Energy Storage and Conversion

https://ojs.acad-pub.com/index.php/esc

ACADEMIC
ACADEMIC PUBLISHING PTE LTD

2024 VOLUME 2 ISSUE 1
ISSN: 3029-2778 (Online)

1

Editorial Team

Editor-in-Chief

Xiaohu Yang
Xi'an Jiaotong University
China

Associate Editor

Rudolf Holze
Chemnitz University of Technology
Germany

Editorial Board Members

Ayesha Kausar
National Center for Physics
Pakistan

Mariacristina Roscia
University of Bergamo
Italy

Narottam Das
Central Queensland University
Australia

Morteza Zare Oskouei
Sahand University of Technology
Iran

Fateh Mebarek-Oudina
University of 20 Août 1955-Skikda
Algeria

Younes Noorollahi
University of Tehran
Iran

Saeed Zeinali Heris
Xi'an University of Science and Technology
China

Kwun Nam Hui
University of Macau
Macau

Surjit Sahoo
Kansas State University
United States

Jiaao Wang
The University of Texas at Austin
United States

Arun Kumar Yadav
Kumoh National Institute of Technology
Korea

Jai Prakash
National Institute of Technology Hamirpur
India

Yuping Wu
Southeast University
China

Rasoul Sarraf Mamoory
Tarbiat Modares University
Iran

Ahmed Al Salaymeh
The University of Jordan
Jordan

Shazia Hasan
Birla Institute of Technology & Science
United Arab Emirates

Hitesh Panchal
Gujarat Technological University
India

Hu Shi
Xi'an Jiaotong Univerisy
China

Wenxiu Que
Xi'an Jiaotong University
China

Arul Manuel Stephan
CSIR-Central Electrochemical Research Institute
India

Yunxiao Wang
University of Wollongong
Australia

Liang Li
Soochow University
China

Jun Wei Lim
Universiti Teknologi PETRONAS
Malaysia

Kriti Tyagi
CSIR-National Physical Laboratory
India

Hamid Reza Rahbari
DTU Construct
Denmark

Byoung-Suhk Kim
Jeonbuk National University
Korea

Ahmed Kadhim Hussein
University of Babylon
Iraq

Zhiyu Li
Shandong University of Technology
China

Masoud Darvish Ganji
Korea Institute of Ceramic Engineering and Technology
Korea

Dumitru Tsiulyanu
Technical University of Moldova
Moldova

Xiaohong Han
Zhejiang University
China

Wael Al-Kouz
University of North Alabama
USA

Mingzhe Yuan
Guangzhou Institute of Industrial Intelligence
China

Hesham A. Hegazi
German University in Cairo
Egypt

Jing Ding
Nanjing Technology University
China

Aman Bhardwaj
Regional Institute of Education
India

Florina Scarlatache
Technical University Gheorghe Asachi of Iasi
Romania

Ahmed Mezrhab
Université Mohammed Premier
Morocco

Muhammad Shahzad Nazir
Huaiyin Institute of Technology
China

Rahim Zahedi
University of Tehran
Iran

Yong Wang
Shanghai University
China

Volume 2 Issue 1 • 2024

Energy Storage and Conversion

Editor-in-Chief

Prof. Xiaohu Yang

Xi'an Jiaotong University, China

ACADEMIC
ACADEMIC PUBLISHING PTE LTD

2024 | Volume 2 | Issue 1

Energy Storage and Conversion

https://ojs.acad-pub.com/index.php/esc

Contents

Articles

1 **Nonlinear controller for SEPIC with single variable to tune**
Youssef El Haj, Vijay Sood, Ahmed Sheir, Ruth Milman

40 **Estimation of the hourly solar radiation**
Muhammed Fatih Saltuk

Reviews

57 **Review on green resources and AI for biogenic solar power**
Jyoti Bhattacharjee, Subhasis Roy

67 **Battery and/or supercapacitor?—On the merger of two electrochemical storage system families**
Yuping Wu, Rudolf Holze

94 **Towards sustainable solar energy solutions: Harnessing supercapacitors in PV systems**
Kerim Karabacak

Energy Storage and Conversion 2024, 2(1), 426.
https://doi.org/10.59400/esc.v2i1.426

Article

Nonlinear controller for SEPIC with single variable to tune

Youssef El Haj, Vijay Sood*, Ahmed Sheir, Ruth Milman

Department of Electrical and Computer Engineering, Ontario Tech University, Oshawa L1H 7K4, Canada
*** Corresponding author:** Vijay Sood, vijay.sood@ontariotechu.ca

CITATION

El Haj Y, Sood V, Sheir A, Milman R. Nonlinear controller for SEPIC with single variable to tune. Energy Storage and Conversion. 2024; 2(1): 426.
https://doi.org/10.59400/esc.v2i1.426

ARTICLE INFO

Received: 22 December 2023
Accepted: 22 January 2024
Available online: 29 January 2024

COPYRIGHT

Copyright © 2024 by author(s). *Energy Storage and Conversion* is published by Academic Publishing Pte. Ltd. This work is licensed under the Creative Commons Attribution (CC BY) license.
https://creativecommons.org/licenses/by/4.0/

Abstract: This work proposes a systematic approach to designing a novel integral sliding mode controller (ISMC) for a single-ended primary-inductor converter (SEPIC) with only one tunable parameter where the upper and lower bounds are derived. The designed surface results in minimal chattering behaviour at the output voltage as well as at the duty cycle and allows for operating the SEPIC at a fixed switching frequency. The proposed controller can withstand up to a 70% variation in the input voltage and 100% variation on the load side, in addition to superior performance for a cold start. The proposed controller and the corresponding mathematical formulation were simulated in a Simulink environment and experimentally tested via a scaled prototype. The proposed controller performance is also compared to Type II and integral Linear-Quadratic Regulators (LQR).

Keywords: SEPIC; ISMC; systematic design; nonlinear controller

1. Introduction

Different types of controllers are designed to achieve one or more objectives based on the target application [1]. For example, in low-power electronic circuits, controlling the converter's output power is the main design objective. This can be extended to different applications, such as LED drives in lighting applications, where the lights can be dimmed by adjusting the converter's output voltage. A battery charging application is another application where the controller is designed to serve objectives such as output current and voltage control. This is expandable to grid-connected renewable energy sources and motor drive applications as well [1–3].

Within the field of power converters, the performance of the designed controller is evaluated and measured based on four metrics: 1) steady-state gain and regulation; 2) dynamic response to load and input disturbances; 3) compliance to electromagnetic interference (EMI) standards and/or total harmonic distortion (THD) regulations; and 4) contribution to converter protection schemes such as overcurrent protection and inrush current limiting. In addition, many controllers are designed not only to satisfy the converter's input-output regulation and performance metrics but also to improve its performance under intrinsic uncertainties, such as components' parasitic capacitance and inductance variations due to soft/ hard saturations [1,4–6]. Therefore, diverse types of control schemes are implemented to achieve as many design objectives as possible. The simplest approach is direct output current control, where a sense of the output voltage provides the correction signal to the controller, which adjusts the converter's duty cycle to maintain the output voltage at or near its reference setting. Such controllers lack the ability to contribute to the converter's protection scheme in terms of short-circuit protection. Other control schemes, such as peak current control and average current control, indirectly control the converter's output

voltage by regulating the internal states, such as the inductor current. The advantage of such schemes is that they satisfy the majority of the controller design objectives while contributing to other aspects of its performance evaluation, such as fast transients and one-cycle short circuit protection [7].

Furthermore, from a controller's law point of view, they can be classified as either linear or nonlinear controllers. Examples of linear controllers are proportional-integral (PI) controllers, type II-III compensators, LQR controllers, and state feedback controllers [4,8]. On the other hand, hysteresis controllers, adaptive controllers, and sliding mode controllers are examples of nonlinear controllers in power electronics. While linear controllers are designed based on the converter's linearized model, they suffer from the severe disadvantage of being able to maintain their performance within narrow regions around the linearized point. On the contrary, nonlinear controllers offer superior performance in terms of satisfying their design objectives and performance metrics over a wider range of load disturbances, input disturbances, parameter uncertainties, and noise [9–14].

Among nonlinear controllers, the sliding mode controller (SMC) has the most attention in both discrete and continuous forms [15]. SMC has a variable structure in its dynamics, ensures disturbance and uncertainty rejection, and performs robust tracking tasks. For instance, in the study of Hamed et al. [15], a modified SMC is designed for a buck converter, and its performance is compared against different types of linear and nonlinear controllers. The study shows that the proposed modified SMC has superior characteristics and fast dynamics. Nonetheless, it is reported that the proposed modified SMC was not able to overcome the chattering phenomenon associated with SMC controllers in general. It also only includes the study of a well-behaved buck converter without explaining how such a controller can be extended to converters with right half-plane zeros or higher-order converters such as SEPIC converters.

An improved SMC for output voltage control in a boost converter is developed in the study of Chincholkar et al. [16]. The proposed controller is applied to a boost converter and compared against PI controllers. Although the research incorporates an integral term, which is a function of the normalized output voltage error, no details were provided on how to solve the chattering issue in the converter's output control signal (duty cycle) or on how to extend this controller to higher-order converters [10,17].

Another approach is introduced in the study of González et al. [18] to overcome the chattering in SMC. In the work, a PI controller is used to form an outer control loop to form a double control loop with the SMC in discontinuous conduction mode (DCM) buck-boost converter. This technique was able to improve the converter's dynamic and steady-state performance. However, it is based on a hysteresis-based SMC, which requires an adaptive feed-forward controller to reduce switching frequency variation. Such frequency restriction is instrumental in reducing EMI noise and input filter design complexity.

A solution to the chattering phenomenon in SMC in power electronics is introduced in the study of Pamdey et al. [19], Ghosh et al. [20], and Das et al. [21]. An integral SMC is developed, which solves the chattering issue in the control signal. This is done by incorporating an integral term to average the output control signal, which

eliminates the chattering and confines the switching frequency to a single frequency. However, the introduced work only covers the design procedure of second-order converters such as buck and boost converters. It also does not cover the converter tuning process that balances the reduction of the chattering of the control signal with the desired dynamic performance.

Furthermore, optimization techniques and artificial intelligence-based SMC design are also introduced [3,12–14,22–25]. It is undeniably beneficial to integrate such techniques with advanced nonlinear controllers such as SMC. It restricts the extension of such algorithms to lower-power and high-density high-power applications where more powerful digital controllers are not available due to size or cost constraints.

In this work, an integral-based SMC is proposed with a systematic approach to design a nonlinear SMC that has not been presented earlier and outlined for high-order converters such as a SEPIC. The main advantage of the proposed controller is that it needs a single value to be tuned over a defined interval with calculated upper and lower bounds. Further, the proposed sliding surface is simple with respect to other proposed sliding surfaces mentioned in the literature. It should be highlighted that the proposed SMC did not compromise the robustness and stability of the system because it was derived based on the dynamics of the converter, where the role of the surface elements was explained and justified. The nonlinearity aspect of the derived SMC rejects varying input voltage disturbances over a wide range. The proposed work is first theoretically proven and then validated by simulation and experimental work. To establish a benchmark with a linear controller, traditional Type-II as well as integral LQR compensators are designed, simulated, and compared with the proposed controller. Furthermore, to complete the comparison analysis between the linear controller and the proposed ISMC, the Type-II compensator will be compared experimentally to the proposed controller. The comparison includes three test categories: cold start, input voltage variation, and load disturbance tests.

The rest of the paper is organized as follows: Section 2 discusses the SEPIC and sliding mode controllers. Section 3 provides the detailed design and modeling of the SEPIC converter. Section 4 deals with the linear and nonlinear controller overview and design for the SEPIC converter. Section 5 provides a derivation of the proposed controller and a step-by-step design guide. Section 6 gives the stability analysis of the proposed controller using the Lyapunov methodology. Section 7 provides the simulation and experimental results of three types of compensators: the Type II compensator, the integral LQR, and the proposed controller. Finally, Section 8 gives concluding remarks on the work presented.

2. SEPIC and sliding mode

The single-ended primary inductor converter (SEPIC) is a fourth-order DC-DC converter. Its large-signal model is highly nonlinear and demonstrates bi-linearity with respect to the control input. Linearized controllers are only valid in a small neighborhood around the equilibrium point, resulting in systems that are vulnerable to instability when faced with any disturbance away from the linearized region. To tackle this issue, a nonlinear controller that provides stable performance over the entire

nonlinear model becomes essential, especially in applications where cost, stability, and performance are critical criteria to maintain, such as integrating renewable energy into the grid and electric vehicles.

Among the nonlinear controller alternatives, the sliding mode controller has an edge with respect to others such as backstepping and feedback linearization. This is because sliding mode control has a variable structure controller that ensures disturbance and uncertainty rejection while performing robust tracking of the desired trajectory. Since DC-DC converters are based on switching mechanisms where the structure varies momentarily based on the switching cycle, a sliding mode controller appropriately complements the application's behaviour.

Different designs for sliding mode control of the SEPIC converter have been addressed in the literature. The work presented in the study of Gireesh et al. [26] uses a pulse width modulated (PWM)-based integral sliding mode control (ISMC) strategy for controlling the output voltage of a SEPIC converter. The work designed an ISMC to regulate the output voltage. The input voltage was varied from 3 to 7 V, while the output was kept at 5 V. The load variation itself was not tested. The output plot had a minor steady-state tracking error. The sliding surface was designed as an error function using the input current, output voltage, and the integral of both voltage and current errors. That sliding surface requires a definition of a reference current for the input inductor. The system is driven based on a PWM signal that is generated based on the equivalent control principle with no switching signal in the control law. On the contrary, the study of Salazar-Duque et al. [27] simplified the sliding surface to be a function of the inductor's current. The reference currents were assigned as the steady-state values of the currents. The controller was tested in two cases. In case I, the input voltage was 24 V, while the reference was changing from 8 to 30 V. In case II, the input voltage was 19 V, and the reference was varied again from 8 to 30 V. The control law was dependent on switching signals with no indication of how it was performed (hysteresis or PWM approach). The system was not tested for variation in the input voltage during the operation or for load variation.

As discussed above, SEPIC converters have the inherent tendency to experience chaotic behaviour as shown in the study of Kavitha et al. [28]. To overcome the instability of the system, an SMC controller was proposed that used a sliding surface composed of the inductor current signal subtracted from a reference value. The desired duty cycle was generated using a hysteresis controller. The system did not investigate the impact of varying either the input, the voltage, or the load on the output behaviour.

Given the fact that robustness is one of the most vital criteria to evaluate the performance of a converter, the researchers in the field proposed another design to ensure a robust response of the SEPIC converter, as demonstrated in the studies of Ablay et al. [29], Li et al. [30], Komurcigil et al. [31], and Jaafar et al. [32]. In the study of Ablay et al. [29], the paper proposed an integral sliding mode controller (ISMC) by defining a surface composed of the negative of the input inductor current and the integral of the error of the output voltage. The surface is simple and proves its ability to track the reference value. The input voltage was 15 V, while the reference voltage varied from 8–25 V. The work proposed a laboratory setup for the controller made of analog components. The control signal was switched using an on/off-based (hysteresis) technique depending on the sign of the sliding surface, which results in a

variable-frequency pulse width modulation (PWM) signal. The system was not tested against variations in either the input voltage or the load impedance. Furthermore, this work used only a simulation study, and experimental results were not presented. Also, the work did not justify how the surface was constructed or the role of the surface elements in system performance and stability. Additionally, from a mathematical perspective, the utilization of the negative current will oppose the surface trajectory, which will result in accumulating more error in the integral function, which may eventually result in slow responses. Alternatively, the system may result in an undesired transient oscillation to make the system reach faster to the desired equilibrium points, given that the scaling factors of the error functions are pre-selected and strong enough to ride the system towards the desired trajectories. From the Lyapunov stability perspective, this type of surface does not ensure negative definite functions under the analysis of a typical Lyapunov candidate function for an SMC; hence, the stability should be studied further.

A universal design has been illustrated in the study of Li et al. [30], where the work proposed a double integral sliding mode controller (DISMC) to control a SEPIC converter. The proposed design was implemented on FPGA and DSP boards operating at 500 kHz and 20 kHz, respectively. The sliding surface was composed of errors in the input inductor current, errors in the output voltage, single and double integrals of the current, and voltage error summation. The controller was operated using a PWM technique. The algorithm was tested by reducing the load from 40 to 20 ohms.

Designing a robust system with a simple design structure is highly recommended. To adhere to this requirement, a simple sliding surface composed of the error in the input inductor current was proposed in the study of Komurcugil et al. [31]. The reference current was generated by a PI controller, which takes its input by measuring the output voltage. The control signal was generated using a hysteresis controller. The controller was tested against input variations where the input was varied from 30–60 V while the output was maintained at a fixed level of 48 V. The load was varied from 50–100 ohms and vice versa. The effect of combining the two variations (load and input voltage) was not shown.

To define the structure of the sliding surface, the study of Jaafar et al. [32] proved the instability of sliding surfaces composed only of any combination of output error voltage, including the error itself, its integral, and its derivative. The work proved the requirement of including at least the error in the input inductor current in addition to the previously defined surfaces. The control signal was derived based on the equivalent control that is free from the switching function. Nevertheless, neither a variation in the input voltage nor in the load was discussed.

Based on the addressed literature, there is a gap in investigating the impact of integrating fast dynamic and variable power resources where the input voltage declines, such as a supercapacitor, as an input to the SEPIC converter. Designing a stable SEPIC converter in buck and boost operation that can withstand major input voltage variation as well as output load variation will allow a resilient and wider range of integration of hybrid energy sources in different fields, such as microgrid-connected fields and electric vehicles.

The prime challenge in this work is to integrate input power sources that drop significantly (primarily to mimic supercapacitor behaviour) with the SEPIC converter

because a typical linear controller fails to achieve the desired response and may impact system stability. Furthermore, the design of a SEPIC controller is a challenging task from both linear and nonlinear controller perspectives. This is because linear controllers for SEPIC converters result in a system with low bandwidth, while the nonlinear controller design method has not been addressed in the literature in a systematic way, unlike linear controllers. In fact, the controllers discussed in the literature suffered from different disadvantages and limitations, as discussed earlier in this chapter. Further details explaining what makes designing a SEPIC controller a challenging task will be covered in the next section.

3. Design and modeling of SEPIC converter

3.1. Mathematical modeling of SEPIC converter

In the DC/DC converter family, the standard SEPIC converter (**Figure 1**) can both buck and boost the DC input voltage. The basic topology of a SEPIC converter is composed of two inductors, two capacitors, a switch, and a diode. SEPIC is classified as a fourth-order converter based on the number of energy storage devices.

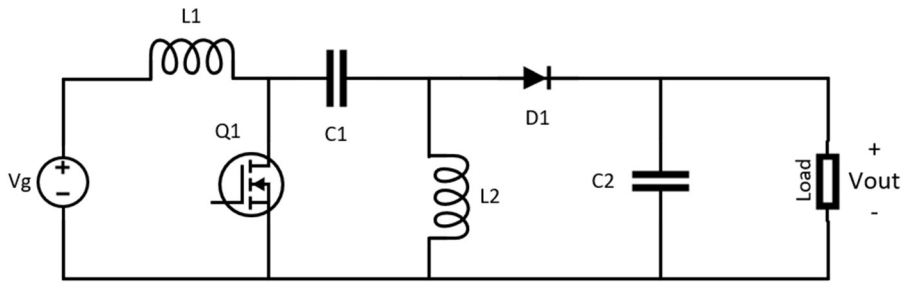

Figure 1. Standard SEPIC circuit.

By controlling the duty cycle (D) of the switch, the SEPIC converter will exhibit a switching mechanism that will result in stepping up or down the input voltage. The input-output relationship with respect to the duty cycle D is given in Equation (1):

$$\frac{v_{out}}{v_g} = \frac{D}{1-D} \tag{1}$$

where D is the duty cycle of the switch.

Specifically, the output of the SEPIC as a function of the duty cycle is summarized as follows:

$$\text{If } D = \begin{cases} < 0.5 & v_{out} < v_{in} \rightarrow \text{Buck mode} \\ = 0.5 & \text{then } v_{out} = v_{in} \\ > 0.5 & v_{out} > v_{in} \rightarrow \text{Boost mode} \end{cases} \tag{2}$$

Deriving the averaged state-space model of the DC-DC power converter is done in two steps. The first step in deriving the averaged model of the SEPIC is to address the converter dynamics while the switch is in the "on" and the "off" states. In the second step, the two sets of differential equations corresponding to the on and off states are averaged over one switching cycle.

Thus, when the switch is in the on position, the SEPIC converter is given in **Figure 2**.

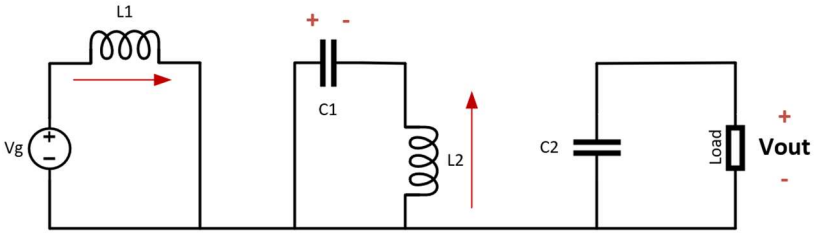

Figure 2. SEPIC converter when the switch is on.

The system's differential equations are defined as:

$$\begin{aligned} \boldsymbol{v_{L1}} &= \boldsymbol{L_1}\frac{\boldsymbol{di_{L1}}}{\boldsymbol{dt}} = \boldsymbol{v_g(t)} - \boldsymbol{r_{L1}i_{L1}} \\ \boldsymbol{v_{L2}} &= \boldsymbol{L_2}\frac{\boldsymbol{di_{L2}}}{\boldsymbol{dt}} = \boldsymbol{v_{c1}(t)} - \boldsymbol{r_{L2}i_{L2}} \\ \boldsymbol{i_{C1}} &= \boldsymbol{C_1}\frac{\boldsymbol{dv_{C1}}}{\boldsymbol{dt}} = -\boldsymbol{i_{L2}(t)} \\ i_{C2} &= C_2\frac{dv_{C2}}{dt} = -\frac{v_{c2}(t)}{R} \end{aligned} \tag{3}$$

When the switch is turned off, the converter model is shown in **Figure 3**.

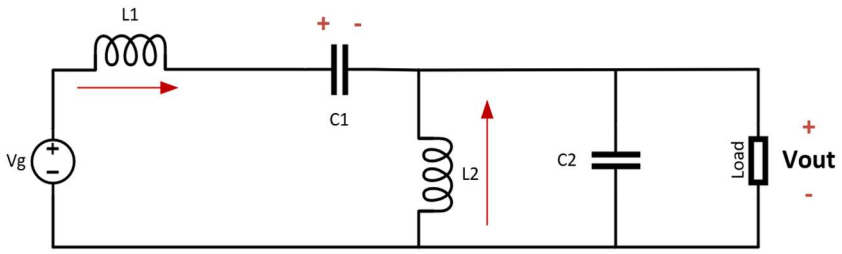

Figure 3. SEPIC converter when the switch is off.

Analyzing the system, the following differential equations are derived:

$$\begin{aligned} \boldsymbol{v_{L1}} &= \boldsymbol{L_1}\frac{\boldsymbol{di_{L1}}}{\boldsymbol{dt}} = \boldsymbol{v_g(t)} - \boldsymbol{v_{C1}(t)} - \boldsymbol{v_{C2}(t)} - \boldsymbol{r_{L1}i_{L1}} \\ \boldsymbol{v_{L2}} &= \boldsymbol{L_2}\frac{\boldsymbol{di_{L2}}}{\boldsymbol{dt}} = -\boldsymbol{v_{c2}(t)} - \boldsymbol{r_{L2}i_{L2}} \\ \boldsymbol{i_{C1}} &= \boldsymbol{C_1}\frac{\boldsymbol{dv_1}}{\boldsymbol{dt}} = \boldsymbol{i_{L1}(t)} \\ i_{C2} &= C_2\frac{dv_2}{dt} = i_{L1}(t) + i_{L2}(t) - \frac{v_{c2}(t)}{R} \end{aligned} \tag{4}$$

Using Equations (3) and (4) in state space representation, the averaged model of the SEPIC converter can be derived using the relationship defined in Equation (5):

$$\begin{aligned} \boldsymbol{A_{avg}} &= \boldsymbol{A_1 u(t)} + \boldsymbol{A_2}\big(\boldsymbol{1} - \boldsymbol{u(t)}\big), \\ B_{avg} &= B_1 u(t) + B_2\big(1 - u(t)\big), \end{aligned} \tag{5}$$

where $u(t)$ is the system input, A_1 and B_1 are the system input matrices respectively when the switch is on and A_2 and B_2 are the system and the input matrices respectively when the switch is off.

The average state-space representation for the SEPIC converter is obtained and expressed in Equation (6):

$$\begin{bmatrix} \dot{x_1} \\ \dot{x_2} \\ \dot{x_3} \\ \dot{x_4} \end{bmatrix} = \begin{bmatrix} -\frac{r_{L1}}{L_1} & 0 & -\frac{1-u}{L_1} & -\frac{1-u}{L_1} \\ 0 & -\frac{r_{L2}}{L_2} & \frac{u}{L_2} & -\frac{1-u}{L_2} \\ \frac{1-u}{C_1} & -\frac{u}{C_1} & 0 & 0 \\ \frac{1-u}{C_2} & \frac{1-u}{C_2} & 0 & -\frac{1}{RC_2} \end{bmatrix} \begin{bmatrix} x_1 \\ x_2 \\ x_3 \\ x_4 \end{bmatrix} + \begin{bmatrix} \frac{V_g}{L_1} \\ 0 \\ 0 \\ 0 \end{bmatrix}, \tag{6}$$

where $x_1 = i_{L1}$, $x_2 = i_{L2}$, $x_3 = v_{C1}$, $x_4 = v_{C2}$, and v_g =input voltage.

As demonstrated in Equation (6), this model addresses the equivalent series resistance (ESR) of the inductors while the capacitors' ESR has been suppressed because the inductor ESR is dominant with respect to capacitor parasitic.

From a linear controller perspective, the SEPIC model in Equation (6) is still in bilinear form and cannot be used to design a linear controller. Therefore, this form must be linearized, where the linearized model will define a relationship between the system controller input and the state variables. Hence, by perturbing the state variables, considering small signal approximations, and then linearizing the derived terms, the small signal model in state-space representation is obtained as below.

$$\boldsymbol{A} = \begin{bmatrix} \boldsymbol{0} & \boldsymbol{0} & -\frac{\boldsymbol{1-D_u}}{\boldsymbol{L_1}} & -\frac{\boldsymbol{1-D_u}}{\boldsymbol{L_1}} \\ \boldsymbol{0} & \boldsymbol{0} & \frac{\boldsymbol{Du}}{\boldsymbol{L_2}} & -\frac{\boldsymbol{1-D_u}}{\boldsymbol{L_2}} \\ \frac{\boldsymbol{1-D_u}}{\boldsymbol{C_1}} & -\frac{\boldsymbol{D_u}}{\boldsymbol{C_1}} & \boldsymbol{0} & \boldsymbol{0} \\ \frac{\boldsymbol{1-D_u}}{\boldsymbol{C_2}} & \frac{\boldsymbol{1-D_u}}{\boldsymbol{C_2}} & \boldsymbol{0} & -\frac{\boldsymbol{1}}{\boldsymbol{RC_2}} \end{bmatrix},$$

$$\boldsymbol{B} = \begin{bmatrix} \frac{\boldsymbol{v_{1_{ss}} + v_{2_{ss}}}}{\boldsymbol{L_1}} \\ \frac{\boldsymbol{v_{1_{ss}} + v_{2_{ss}}}}{\boldsymbol{L_2}} \\ \frac{\boldsymbol{-i_{1_{ss}} - i_{2_{ss}}}}{\boldsymbol{C_1}} \\ \frac{\boldsymbol{-i_{1_{ss}} - i_{2_{ss}}}}{\boldsymbol{C_2}} \end{bmatrix}, \boldsymbol{C} = [\boldsymbol{0\ 0\ 0\ 1}], \boldsymbol{D} = \boldsymbol{0}, \boldsymbol{x} = \begin{bmatrix} \boldsymbol{x_1} \\ \boldsymbol{x_2} \\ \boldsymbol{x_3} \\ \boldsymbol{x_4} \end{bmatrix} \tag{7}$$

where: $i_{1_{ss}} = \frac{D_u^2}{(1-D_u)^2}\frac{v_g}{R}$, $i_{2_{ss}} = \frac{D_u}{1-D_u}\frac{v_g}{R}$, $v_{1_{ss}} = v_g$ and $v_{2_{ss}} = \frac{D_u}{1-D_u}v_g$.

The derived linear state-space model is effective in designing linear controllers that require knowledge of each state dynamic, such as state feedback and its optimized version, LQR. Other standard linear controllers (such as PID family and lead/lag compensators) require only a transfer function that describes a relationship between the control variable and the output voltage if the goal is to regulate the output voltage. In the literature, extensive work has been done to define this transfer function in the study of Basso [33], and this model is given in Equation (8).

Within the scope of this work, the discussed three models of SEPIC converter will be used to design the proposed ISMC, integral LQR, and Type-II compensator, while the system response will be simulated on the switched bilinear model using

MATLAB/Simulink package. Furthermore, the designed controllers will be verified with experimental benchwork using a SEPIC converter.

$$\frac{\boldsymbol{v_{out}}}{\boldsymbol{u}}(\boldsymbol{s}) = \boldsymbol{K_d}\frac{(-\boldsymbol{A_1 s}+\boldsymbol{1})(\boldsymbol{A_2 s^2}-\boldsymbol{A_3 s}+\boldsymbol{1})}{(\boldsymbol{A_4 s^2}+\boldsymbol{A_5 s}+\boldsymbol{1})(\boldsymbol{A_6 s^2}+\boldsymbol{A_7 s}+\boldsymbol{1})} \tag{8}$$

where: $K_d = \frac{1}{(D')^2}$ and $D' = 1 - D$, and D is the duty cycle. $A_1 = \left(\frac{L_1}{R}\right)\left(\left(\frac{D}{D'}\right)^2\right)$, $A_2 = L_2\frac{C_1}{D}$, $A_3 = \left(C_1 R\frac{L_1+L_2}{L_1}\right)\left(\left(\frac{D'}{D}\right)^2\right)$, $A_4 = \frac{1}{w_{o1}^2}$, $A_5 = \frac{1}{w_{o1}Q_1}$, $A_6 = \frac{1}{w_{o2}^2}$, $A_7 = \frac{1}{w_{o2}Q_2}$, $w_{o1} = \frac{1}{\sqrt{\left(\left(L_1\left(\left(C_2\frac{D^2}{D'^2}\right)+(C_1)\right)\right)+(L_2(C_1+C_2))\right)}}$, $Q_1 = \frac{R}{w_{o1}\left(\left(L_1\left(\frac{D^2}{D'^2}\right)\right)+L_2\right)}$, $w_{o2} = \sqrt{\left(\left(\frac{D'^2}{L_1L_2C_1C_2}\right)\left(\left(L_1\left(C_2\left(\left(\frac{D}{D'}\right)^2\right)+C_1\right)\right)+(L_2(C_1+C_2))\right)\right)}$, $Q_2 = \frac{R}{w_{o2}(L_1+L_2)\left(\frac{C_1}{C_2}\right)\left(\frac{w_{o1}}{w_{o2}}\right)^2}$.

3.2. Design of SEPIC converter

In this work, the foundation of the analysis is based on a proper design for a SEPIC converter. Typically, the circuit parameters of the SEPIC converter play a key role in the controller's bandwidth as well as its robustness. This is evident through analyzing the Bode plot of G_{vd} transfer function (i.e., the output voltage to duty cycle transfer function). Typical bode plots of G_{vd} show that SEPIC has double resonance peaks due to the existence of three right half-plane zeros. Additionally, the second resonance is much higher than the first, which impacts the system bandwidth at closed loop. Therefore, it is essential to ensure that the SEPIC is well designed to eliminate the case where the designed compensator cannot offer much due to a poorly designed plant. In this work, the SEPIC converter has been designed using industrial best practices and systematic methodology. The SEPIC converter has been designed following the AN-1484 and TPS-61175 design guides from Texas Instruments (TI). The final design of the converter was tuned to accommodate and withstand the severe tests, as will be explained in later sections. The final design of the designed SEPIC converter is shown in **Table 1**.

Table 1. Designed SEPIC circuit parameters.

Inductor L1, L2	Capacitor C1	Capacitor C2	Load	Input voltage	Output voltage/power	Switching frequency
0.25 mH	2.78 uF	23.15 uF	46.08 Ω	24 V	48 V/50 W	50 kHz

4. Linear and nonlinear controller overview and design for SEPIC converter

4.1. Linear controller

Linear compensators in power converters are designed based on negative feedback systems. The definition of a negative feedback system dictates that the

relationship between the output and the input must be maintained despite the change in the amplitude as well as the rate of change in the control variable, even in the presence of perturbations in the system. Negative feedback is achieved by introducing a new block to the system that takes the error between the output and the set point as its input. This block is referred to as a compensator (other references refer to it as a controller) because it compensates for system imperfections by tailoring the response of the system [9]. Linear compensators can be presented in different structures, such as PID, lead/lag compensators, state feedback, Type-I, -II, -III compensators, etc. In this work, a Type-II compensator and an integral LQR controller were studied. Type-II compensator is standard in the power converter field, and it forms the benchmark for comparative analysis, while an integral LQR controller forms the optimized version of the linear controllers. In the next subsections, Type-II compensators will be discussed. After that, the following subsections will address the integral LQR system.

Type-II compensator:

The Type-II compensator transfer function is comprised of two poles and one zero. It is designed by placing one pole at the origin while the remaining zero-pole pair is placed at a desired/designed location. The placement of the zero-pole pair creates a region of zero gain slope and a corresponding boost in the phase, as shown in **Figure 4**.

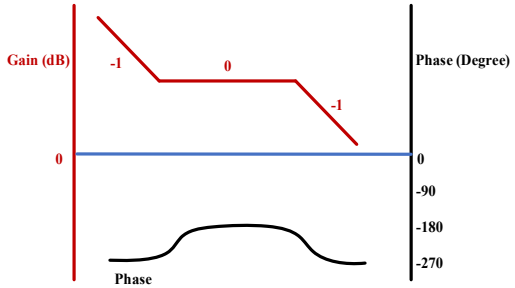

Figure 4. Plot of Type-II transfer function.

This compensator boosts the phase shift from −270° towards −180° during the zero-slope region. Hence, it is evident from **Figure 4** that the maximum boost in the phase is 90 degrees, while the region of this boost is dependent on the zero-slope region. That is, the location of the zero-pole dictates the region where the phase boost will occur. Typically, a Type-II compensator is designed where the loop gain cross-over frequency is occurring at the center of the zero-slope region. Hence, the Type-II compensator is given as shown in Equation (9):

$$\boldsymbol{G_c(s) = \frac{K_c}{s}\frac{(1+\frac{s}{w_z})}{(1+\frac{s}{w_p})}} \tag{9}$$

where K_c is a DC gain. It should be noted that the zero should be placed before the poles (i.e., $w_z < w_p$) which implies that the zero is earlier than the pole, hence it satisfies the boost in the phase requirements.

In the literature, there are different approaches to designing Type-*i* compensators (where *i* = I, II, or III). In this work, *K*-factor method will be used as it is a popular approach in the industry as well as it is a systematic procedure. As per the analysis of

the *K*-factor method, the Type-II compensator is the most suitable compensator for the designed SEPIC model in this work.

As per K-factor method, the first step is to select the desired system cross over frequency (w_c) where the transfer function defined in Equation (8) is used to fulfill this task. In the industry, the desired bandwidth is selected to be one-tenth the switching frequency ($\frac{1}{10} f_{sw}$) as per best practices. However, in the existence of RHPZ, this criterion is not a trivial goal to achieve. Equivalently, as per best practices, once the previous criterion is not achieved, the bandwidth is limited to one-tenth of the lowest RHPZ frequencies, such that the design will offer enough margin to suppress the effect of the RHPZ in a closed loop. By investigating the system frequency response as shown in **Figure 5**, the desired system cross-over frequency is located at 445.15 Hz.

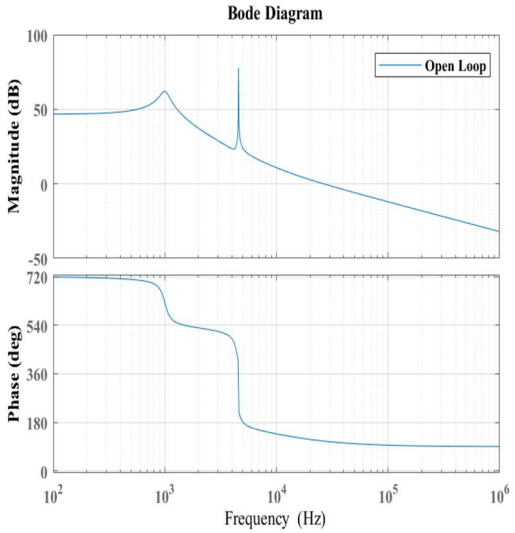

Figure 5. Frequency response of open loop SEPIC converter.

By considering the desired phase margin to be 60°, the required boost in the phase becomes 21°. Therefore, referencing **Table 2**, the needed compensator to use is a Type-II compensator.

Table 2. Compensator type selection guide.

$\boldsymbol{\varphi_{boost} = \text{Phase Margin}_{\text{desired}} - \varphi_{sys} - 90^{\circ}}$	
Required $\boldsymbol{\varphi_{boost}}$	**Compensator type**
Zero degree (**0°**)	Type-I
Less than **90°** (Required $\boldsymbol{\varphi_{boost} < 90°}$)	Type-II
Greater than **90°** (Required $\boldsymbol{\varphi_{boost} \geq 90°}$)	Type-III

After deciding the compensator type, the next step is to start designing the controller parameters. Recalling that Type-II compensator is given by:

$$G_c(s) = \frac{K_c}{s} \frac{(1 + \frac{s}{w_z})}{(1 + \frac{s}{w_p})} \tag{10}$$

The first step will be to calculate w_z and w_p where they are given as:

$$\begin{aligned} \boldsymbol{w_z} &= \frac{\boldsymbol{w_c}}{\mathbf{K}} \\ w_p &= \mathrm{K}.w_c \end{aligned} \tag{11}$$

and K is defined for Type-II compensator to be:

$$K = \tan\left(\frac{\varphi_{boost}}{2} + 45°\right) \tag{12}$$

While determining the type of the compensator the required phase boost is 21°. Hence, the K-factor term will be given as 0.6857. Consequently, the compensator zeros and poles are given as:

$$\begin{aligned} \boldsymbol{w_z} &= \mathbf{4.0789 \times 10^3}\ \mathrm{Hz} \\ w_p &= 1.9179 \times 10^3\ \mathrm{Hz} \end{aligned} \tag{13}$$

Consequently, Type-II compensator for the SEPIC converter demonstrated in **Table 1** is derived to be:

$$G(s)_{comp} = \frac{5997\mathrm{s} + 7.823 \times 10^6}{4079s^2 + 7.823 \times 10^6 s} \tag{14}$$

The open loop, loop gain, and the closed loop Bode plots are shown in **Figure 6**.

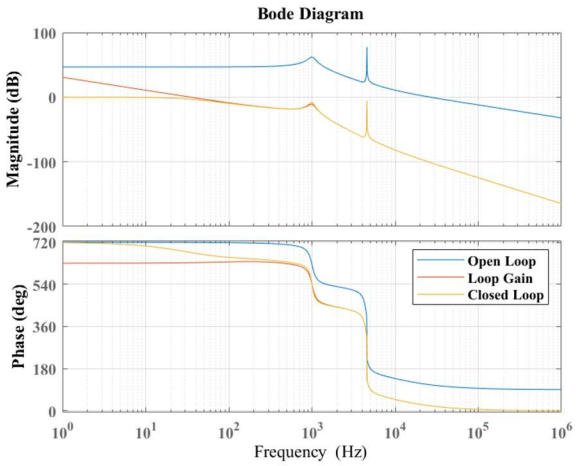

Figure 6. Bode plots of open loop, loop gain, and closed loop.

Integral LQR controller:

Linear quadrature regulator (LQR) is an optimal linear controller that is based on a structural approach to calculate and define the state feedback gains of the system controller. Optimal controllers generally and LQR controllers specifically are based on minimizing a performance index (typically referred to as a cost function) such as the integral of square error denoted by, as given in Equation (15):

$$J = \int_0^\infty (x^T Q x + u^T R u)\mathrm{d}\tau \tag{15}$$

where: x is the state variable vector, u is the control input vector, and Q is a positive semi-definite or definite Hermitian matrix. Q is $n \times n$, where n is number of states, R is a positive definite Hermitian matrix, and R is $r \times r$ where r is the number of inputs.

The performance index proposed in Equation (15) is minimized by solving the Riccati equation as defined in Equation (16):

$$\boldsymbol{A^T P + PA - PBR^{-1}B^T P + Q = 0} \tag{16}$$

where: A is the system matrix, B is the input matrix, Q and R as defined in Equation (15), and P is a positive definite matrix of size $(n \times n)$.

As it can be observed from the Riccati equation, solving the system will result in matrix P since the other variables are either known or assumed without loss of generality. Satisfying the Riccati equation will minimize the cost function, and for the regulator controller case it can be proven that the state feedback gain will be given as:

$$\boldsymbol{K_{gain} = R^{-1}B^{T}P} \tag{17}$$

where: K_{gain} is the state feedback vector.

In some designs, especially in high-order systems, the state feedback controller is not sufficient to perform the tracking task, and it is not capable of rejecting external disturbances, overcoming model uncertainties, or maintaining zero steady-state error. Introducing an integrator usually overcomes these challenges. The integral LQR controller is based on introducing an additional pole at the origin in addition to solving the optimal performance equation. By introducing an integrator to the system, the plant block diagram is depicted in **Figure 7**.

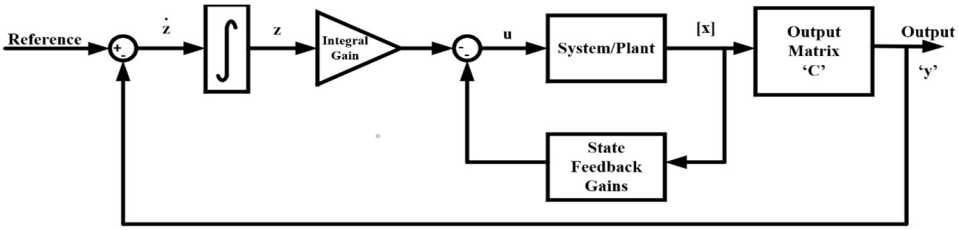

Figure 7. Block diagram of plant with integral LQR.

From **Figure 7**, the new system model with the inclusion of integral action can be described in matrix form to be:

$$\begin{bmatrix} \dot{\boldsymbol{x}} \\ \dot{\boldsymbol{z}} \end{bmatrix} = \begin{bmatrix} \boldsymbol{A} & \boldsymbol{0} \\ -\boldsymbol{C} & \boldsymbol{0} \end{bmatrix} \begin{bmatrix} \boldsymbol{x} \\ \boldsymbol{z} \end{bmatrix} + \begin{bmatrix} \boldsymbol{B} \\ -\boldsymbol{D} \end{bmatrix} \boldsymbol{u} + \begin{bmatrix} \boldsymbol{0} \\ \boldsymbol{1} \end{bmatrix} \boldsymbol{Ref}$$
$$\boldsymbol{y} = [\boldsymbol{C}\ \boldsymbol{0}] \begin{bmatrix} \boldsymbol{x} \\ \boldsymbol{z} \end{bmatrix} + \boldsymbol{Du} \tag{18}$$

Therefore, the model in augmented notion can be described to be:

$$\boldsymbol{\dot{X}_A = A_A X_A + B_A u + FRef}$$
$$\boldsymbol{y = C_A X_A + D_A u}$$

where: $A_A = \begin{bmatrix} A & 0 \\ -C & 0 \end{bmatrix}, B_A = \begin{bmatrix} B \\ -D \end{bmatrix}, C_A = [C\ 0], D_A = D, X_A = \begin{bmatrix} x \\ z \end{bmatrix}$, and $u = -K_A X_A$, where $K_A = [K\ K_i]$.

The following step in designing the integral LQR controller is to define Q and R matrices given in Equation (15), where the Q matrix is required to be positive semi-definite and its dimension is same as (A_A).

Considering the dimension of the SEPIC model, the Q matrix is (5×5) a diagonal matrix, where the *i*-th diagonal element will represent the importance (weight) of the corresponding state variable with respect to the controller objective. In this work, a single input-single output (SISO) structure is adopted to control the SEPIC. As a result, the *R*-matrix will be single value (1×1). The weight of the *R*-element will be the highest because it must be fast to accommodate the switching of the PWM signal generator, provide an acceptable transient response, and provide comparable performance with respect to nonlinear techniques. The elements of the Q

and R matrices are tuned to achieve the desired performance.

The next step is to derive and solve the Riccati equation of the integral LQR. In this work, the optimization is done using the MATLAB toolbox to tune the Q and R matrices and obtain the desired response, while the cost and the state feedback gains are optimized using the MATLAB toolbox tools. The integral LQR controller was designed and tuned for the designed SEPIC converter, as shown in **Table 1**. Using MATLAB simulation to solve the optimization problem, the designed controller gains are listed in **Table 3**.

Table 3. Summary for the designed gains for Integral LQR controller.

Gain 1—K_1	Gain 2—K_2	Gain 3—K_3	Gain 4—K_4	Gain 5—K_5
0.00659	0.00375	−1.60361	0.000385	−3.87298

4.2. Review of sliding mode controller, equivalent control law derivation, and modulation techniques

A sliding mode controller (SMC) is a variable-structure controller. The SMC provides robust tracking for a desired trajectory by defining a sub-manifold that includes the desired trajectory. This manifold is defined as a sliding surface. The construction of the sliding surface is not unique; however, any sliding surface must satisfy the following conditions:

1) The derivative of the sliding surface must include the control input explicitly.
2) As the surface is approaching a zero state, the tracking of the desired trajectory must be achieved.

Typically, the sliding surface can be constructed using a linear combination of the state error functions, linear/nonlinear combinations of the state variable, and an integral or derivative of the aforementioned combinations.

Before deriving the control law for the proposed SMC, a brief explanation of the sliding surface dynamics is provided.

Consider the nonlinear n-th-order system:

$$x^n = f(X,t) + b(X,t).u(X,t) + d(t),$$

where:

- $f(X,t)$ is the nonlinear system model (it may not be exactly known) which must be bounded from above by a known continuous function of the state variable (X) and time (t),
- $b(X,t)$ is the control gain which must also be bounded by a constant function of state variable (X) and time (t),
- $u(X,t)$ is the control input, and
- $d(t)$, is unknown and must be bounded from above by a known continuous function of the state variable (X) and time (t).

It can be shown that the SMC successfully tackles the highly nonlinear and bilinear system, which makes it a perfect candidate for power converters.

If the sliding surface is constructed to include the desired trajectory, then solving the control problem will require two actions:

1) Reaching the sliding surface from any point in the space (regardless of the initial conditions), and

2) Staying on the surface at the desired state.

The first action, reaching the sliding surface, can be achieved by satisfying the sliding condition which is defined to be:

$$\frac{1}{2}\frac{d}{dt}\mathbb{S}^2 \leq -\eta|\mathbb{S}| \tag{19}$$

where $\mathbb{S}$ is sliding surface and η is a positive constant.

If the sliding condition in Equation (19) is satisfied, this will imply that the squared distance towards the surface will keep decreasing, which will force the trajectories to converge towards the sliding surface regardless of the presence of disturbances and the imprecisions in the modeled dynamics. Further, the sliding condition ensures that the sliding surface will be reached, regardless of the initial condition, in a finite time given by:

$$time_{reach\ surface} \leq \frac{\mathbb{S}(t=0)}{\eta}. \tag{20}$$

Furthermore, satisfying the sliding conditions will make the time-varying surface an invariant set. In other words, the surface as $\mathbb{S}^2$ must be maintained as a Lyapunov function with respect to the defined control law.

The second required action to define proper constraints to derive the control law is to ensure that the system will stay on the sliding surface after reaching it. In other words, if the control law is derived such that the sliding surface that is defined for the system's dynamical equations leads to a zero value, then this implies that the desired states reside on the surface; hence, the first derivative must be zero. **Figure 8** illustrates this aspect of the sliding mode controller.

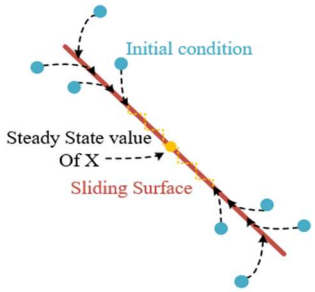

Figure 8. Illustrative trajectory on a sliding surface.

Equivalent control law derivation:

To derive the control law of the SMC, the first step requires constructing the sliding surface based on the earlier discussion. The second step is to define the control law to be:

$$u = u_{eq} + u_n \tag{21}$$

where u_{eq} is the equivalent control vector, while u_n is the switching control term.

The equivalent control term (u_{eq}) is a continuous term, and it is derived based on the system dynamics that will ensure the rate of change in the sliding surface is zero. Typically, the equivalent control term is derived as follows:

1) Find the derivative of the constructed sliding surface,
2) Equate the obtained derivate to zero, and
3) Solve for the control term.

On the other hand, the second term is the switching control term (u_n) which is discontinuous; it accounts for the uncertainties and the system disturbances. Typically, the switching control is given by:

$$u_n = -K_{slide} sgn(\mathbb{S}),$$

where K_{slide} is a positive constant, $\mathbb{S}$ is the sliding surface and sgn is the sign function which is described as:

$$sgn(s) = \begin{cases} 1 \text{ if } \mathbb{S} > 0 \\ -1 \text{ if } \mathbb{S} < 0 \end{cases}$$

The role of $\mathbb{S}$ is to provide enough correction to compensate for any uncertainty or disturbance, while the sign function will ensure the trajectory to the correct direction.

The overall control term (including the equivalent and the switching) can be summarized in the next steps:

1) Find the derivative of the sliding surface ($\dot{\mathbb{S}}$).
2) Equate the ($\dot{\mathbb{S}}$) surface with the switching control term:

$$\dot{\mathbb{S}} = -K_{slide} sgn(\mathbb{S}).$$

3) Solve for the control input term u.

The major advantage of this approach is that it ensures the inclusion of the input vector over the switching control term; hence, the controller will be able to perform a better task in the tracking requirements.

Modulation techniques of the SMC:

In the literature, the SMC is implemented by using either of the following approaches:

- Hysteresis modulation (HM) controller,
- PWM-based on equivalent control law.

a. The hysteresis modulation (HM) controller:

This technique of implementing the SMC is based on the instantaneous sign of the sliding surface, which is defined with respect to the trajectory. Unlike the control law discussed in Equation (21), the HM Controller's control law is simpler and is defined as:

$$\boldsymbol{u = \frac{1}{2}\left(1 - sgn(\mathbb{S})\right) = \begin{cases} u^+ \ \mathbb{S} < 0 \\ u^- \ \mathbb{S} > 0 \end{cases}} \quad (22)$$

Intuitively, the system follows the Filipov structure, where the control signal is composed of two components; each component will guide the system in a region based on the sign of the region with respect to the sliding surface given that the sliding is defined to be zero ($\mathbb{S} = 0$), as illustrated in **Figure 9**.

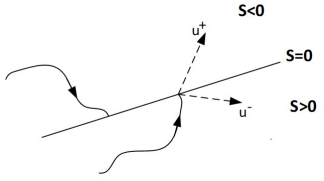

Figure 9. Control law structure using hysteresis controller.

In power converters, the control signal can be either 1 or 0 to drive the semiconductor switch. Therefore, the HM controller will be given as:

$$\boldsymbol{u = \frac{1}{2}\left(1 - sgn(\mathbb{S})\right) = \begin{cases} 1 & \mathbb{S} < 0 \\ 0 & \mathbb{S} > 0 \end{cases}} \quad (23)$$

To satisfy the relationship in Equation (23), the reachability condition for the sliding condition must be met. Hence, by defining a proper Lyapunov candidate function such as ($V = \frac{1}{2}\mathbb{S}^2$), the stability can be proven by having ($\dot{V} = \mathbb{S}\dot{\mathbb{S}} < 0$) which matches with the reachability condition. Consequently, reachability and stability are totally dependent on the sliding surface to satisfy the Lyapunov theorem.

Adopting the HM controller to generate the control signal for SMC suffers from several drawbacks. Firstly, the structure requires infinite switching frequency because it reacts based on the instantaneous sign of the sliding surface. Introducing such a high frequency will introduce high noise in the circuit. Further, the practical implementation of such high-frequency switching is a challenge, and having a sluggish switching behaviour will result in poor performance. On the other hand, if the system requires an input or output filter, then the overall design will be oversized and complicated to satisfy the frequency range of operation. One of the techniques to limit the infinite frequency requirement is to make the switching with respect to a small threshold instead of zero. In other words, the HM controller will be defined as:

$$\boldsymbol{u = \frac{1}{2}\left(1 - sgn(\mathbb{S})\right) = \begin{cases} 1 & \mathbb{S} < \epsilon \\ 0 & \mathbb{S} > -\epsilon \end{cases}} \quad (23)$$

It is highlighted that the introduction of the delay limits the frequency; however, the frequency is still a variable. Furthermore, the value of ϵ is determined by tuning.

b. PWM-based on equivalent control law:

Unlike the HM controller, the PWM-based controller operates at a fixed frequency. Hence, it overcomes all the aforementioned cons. On the other hand, an additional yet simple circuit will be needed to generate the PWM signal. Typically, the PWM signal is generated by comparing a fixed-frequency sawtooth or triangular signal with a reference value. In a power converter, the entered reference signal is the duty cycle of the switch. The comparator will operate the switch by on/off pulses at a fixed frequency.

In SMC implementation, the duty cycle is obtained from the equivalent control law that was illustrated earlier. Typically, the rate of change on the sliding surface is equal to zero. Then, by the definition of the sliding surface, the equation can be solved for a closed form of the control law. In other words:

$$\dot{\mathbb{S}} = 0 \rightarrow \text{solve } f \text{or } u$$

The equivalent control law, as discussed earlier, is continuous and smooth, and it represents the duty cycle of the converter. In other words, the equivalent control signal has low-frequency components and is chatter-free. Therefore, it is a proper representation of the duty cycle of the power converter.

By comparing the generated equivalent control signal to a sawtooth or a triangular signal, the PWM signal is generated to drive the semiconductor switch. One of the disadvantages of this type of technique is that it is weak in its ability to reject disturbances and account for uncertainty. This is because the high-frequency components (switching signals) are not included in the control law. Generally, adding the switching may lead to high chattering in the generated control law and will make the task of generating proper PWM at a fixed frequency imprecise. Nevertheless,

constructing a proper sliding surface based on understanding the model dynamics employs the switching signal, such as the sign function, effectively where the chattering is minimal, and the system is robust with high capability to reject disturbances, uncertainties, and unmodeled dynamics.

5. Derivation of the proposed controller and step-by-step design guide

In this work, a novel approach is proposed to generate the control signal using PWM techniques. The procedure starts by constructing a stable and simple sliding surface. Then the equivalent control law is derived and scaled; a method to define a valid value for the associated gain is introduced. The next step is to add the switching control signal with a proper scaling coefficient. The gain values (for the equivalent and switching controller) are selected to ensure that the chattering is minimal in the converter output as well as in the generated duty cycle; moreover, the gain values are selected to ensure the converter is highly robust against unmodeled dynamics, system uncertainties, and external disturbances.

Typically, the SMC with an equivalent controller approach suppresses the switching element (high frequency) at the cost of system robustness, as discussed earlier. To overcome this scenario and to include the switching element, both the equivalent controller and the switching control signal will be scaled with a proper gain. In the last stage, the total control signal as defined in Equation (21) is used as the input to the PWM generator block. The generated pulses out of the PWM block will be at a fixed frequency, and they will drive the switch in the converter.

Derivation of the sliding surface

Several researchers have discussed SMC for the SEPIC converter and the construction of appropriate sliding surfaces, such as in the studies of Aroudi et al. [6] and Deisch et al. [7]. Depending on the system requirements, combinations of the state variables can be used to construct the surface. In most of the applications described in the literature, the control target is to achieve a robust output voltage tracking task. Hence, it would be expected that the sliding surface will be written as a scaled error function of the output voltage, an integral of the output voltage error signal, or a linear or nonlinear combination of the error signal and its integral. However, this approach is effective for Ćuk converters but not for SEPIC converters. Although both Ćuk and SEPIC are fourth-order converters, they have fundamentally different structures. The studies of Zhang et al. [14] and Hamed et al. [15] have shown that the stability of a sliding surface can be achieved by the earlier discussed approach; in fact, they proved the instability of the surface if it was constructed only by any combination form of output voltage, whether error signal, integral form, or even derivative form. This cited research has shown that to have a stable surface, the surface must include at least one inductor current in the sliding manifold. Nevertheless, there was no concrete justification for the reason behind the inclusion of a state variable such as an inductor current to stabilize the surface.

The answer behind the stabilization of the sliding surface upon the inclusion of the inductor currents relies on investigating the small signal approximation in the

transfer function form. By analyzing the transfer function of the system, where the input is the duty cycle and the output is the inductor current, it is evident that the system is a minimum phase with poles in the left-hand plane (stable system). On the other hand, once the transfer function of SEPIC is constructed between the duty cycle and the output voltage, the resulting system has a non-minimum phase. For this reason, the sliding surface must be constructed to control the output voltage indirectly by introducing the inductor current into the surface. For instance, for the designed converter in this work, the zeros of the SEPIC transfer function from the duty cycle to the input inductor current are given as $-2444 \pm 30{,}817j$ and -1883 which confirms that the system is in the minimum phase due to the zero placement in the left-hand plane region.

As a result, let the sliding surface to be:

$$\mathbb{S} = \boldsymbol{i_{L1}} + \boldsymbol{\lambda} \int (\boldsymbol{v_{C2}} - \boldsymbol{v_{ref}}) \mathbf{d}\boldsymbol{\tau} \tag{25}$$

where λ is a positive constant that is designed as follows:

(1) First, the equivalent control law is derived as discussed in previous sections:

- Find the derivative of the constructed sliding surface and equate the obtained derivate with zero:

$$\frac{\mathbf{d}\boldsymbol{s}}{\mathbf{d}\boldsymbol{t}} = \dot{\mathbb{S}} = \frac{\boldsymbol{d}}{\mathbf{d}\boldsymbol{t}}\left(\boldsymbol{i_{L1}} + \boldsymbol{\lambda} \int (\boldsymbol{v_{C2}} - \boldsymbol{v_{ref}}) \mathbf{d}\boldsymbol{\tau}\right) = \mathbf{0}$$

$$\dot{\mathbb{S}} = \dot{\boldsymbol{\imath}}_{\boldsymbol{L1}} + \boldsymbol{\lambda}(\boldsymbol{v_{C2}} - \boldsymbol{v_{ref}}) = \mathbf{0} \tag{26}$$

$$\dot{\mathbb{S}} = -\frac{\boldsymbol{r_{L1}}}{\boldsymbol{L_1}} \boldsymbol{i_{L1}} + \frac{\boldsymbol{u}-\mathbf{1}}{\boldsymbol{L_1}} \boldsymbol{v_{C1}} + \frac{\boldsymbol{u}-\mathbf{1}}{\boldsymbol{L_1}} \boldsymbol{v_{C2}} + \frac{\boldsymbol{v_g}}{\boldsymbol{L_1}} + \boldsymbol{\lambda}\left(\boldsymbol{v_{C2}} - \boldsymbol{v_{ref}}\right) = \mathbf{0}$$

- Solve for the control term:

$$\boldsymbol{u_{eq}} = \frac{\left[\boldsymbol{r_{L1}} \boldsymbol{i_{L1}} + \boldsymbol{v_{C1}} + \boldsymbol{v_{C2}} - \boldsymbol{v_g} - \boldsymbol{\lambda} \boldsymbol{L_1}\left(\boldsymbol{v_{C2}} - \boldsymbol{v_{ref}}\right)\right]}{\boldsymbol{v_{C1}} + \boldsymbol{v_{C2}}} \tag{27}$$

(2) Since the control signal is needed to operate the switch in the SEPIC, u_{eq} is bounded by the limits of the PWM signals that turn on/off the semiconductor switch. In other words, u_{eq} is bounded between 0 and 1; that is:

$$0 < u_{eq} < 1$$

By applying the lower and upper bounds of u_{eq} (i.e., the zero and one respectively), the corresponding domain of λ can be defined. For simplicity, the ideal model will be described here, where the parasitic value is suppressed.

Consider the lower bound: ($u_{eq} > 0$)

$$\frac{\left[\boldsymbol{v_{C1}} + \boldsymbol{v_{C2}} - \boldsymbol{v_g} - \boldsymbol{\lambda} \boldsymbol{L_1}\left(\boldsymbol{v_{C2}} - \boldsymbol{v_{ref}}\right)\right]}{\boldsymbol{v_{C1}} + \boldsymbol{v_{C2}}} > \mathbf{0} \tag{28}$$

Then, the inequality can be described as:

$$\left[\boldsymbol{v_{C1}} + \boldsymbol{v_{C2}} - \boldsymbol{v_g} - \boldsymbol{\lambda} \boldsymbol{L_1}\left(\boldsymbol{v_{C2}} - \boldsymbol{v_{ref}}\right)\right] > \mathbf{0} \tag{29}$$

By solving for $\boldsymbol{\lambda}$, the following inequality is obtained:

$$\boldsymbol{\lambda} < \frac{\mathbf{1}}{\boldsymbol{L_1}}\left(\frac{\boldsymbol{v_g} - \boldsymbol{v_{C1}} - \boldsymbol{v_{C2}}}{\boldsymbol{v_{ref}} - \boldsymbol{v_{C2}}}\right) \tag{30}$$

The next step, is to consider the upper bound: ($u_{eq} < 1$)

$$\frac{\left[\boldsymbol{v_{C1}} + \boldsymbol{v_{C2}} - \boldsymbol{v_g} - \boldsymbol{\lambda}.\boldsymbol{L_1}\left(\boldsymbol{v_{C2}} - \boldsymbol{v_{ref}}\right)\right]}{\boldsymbol{v_{C1}} + \boldsymbol{v_{C2}}} < \mathbf{1} \tag{31}$$

The inequality, can be simplified to be:

$$\boldsymbol{\lambda < \frac{1}{L_1}\left(\frac{v_g}{v_{ref} - v_{C2}}\right)} \tag{32}$$

When comparing the two results from the inequalities in Equations (30) and (32), the result of the inequality in Equation (32) will be used, as this constraint also satisfies the inequality in Equation (30). The maximum value of λ is described by inequality Equation (32) and will be achieved once $v_{C2} = 0$. It should be noted that the SEPIC is operated in continuous conduction mode (CCM) with a positive input voltage; thus v_{C2} is positive.

Next, λ must be selected to satisfy the bounds:

$$\boldsymbol{0 < \lambda < \frac{1}{L_1}\left(\frac{v_g}{v_{ref}}\right)} \tag{33}$$

By defining and deriving all the parameters on the sliding surface, the next task will be to derive the sliding mode controller law. This is achieved by following the steps in the aforementioned sections; the sliding mode controller is derived as follows:

(1) Find the derivative of the sliding surface ($\dot{\mathbb{S}}$):

$$\boldsymbol{\frac{ds}{dt} = \dot{\mathbb{S}} = \frac{d}{dt}\left(i_{L1} + \lambda \int (v_{C2} - v_{ref})d\tau\right)}$$

$$\boldsymbol{\dot{\mathbb{S}} = \dot{\imath_{L1}} + \lambda(v_{C2} - v_{ref})} \tag{34}$$

$$\boldsymbol{\dot{\mathbb{S}} = -\frac{r_{L1}}{L_1} i_{L1} + \frac{u-1}{L_1} v_{C1} + \frac{u-1}{L_1} v_{C2} + \frac{v_g}{L_1} + \lambda\left(v_{C2} - v_{ref}\right)}$$

(2) Equate the ($\dot{\mathbb{S}}$) with the switching control term:

$$\boldsymbol{\dot{\mathbb{S}} = -K_{slide} sgn(\mathbb{S})}$$

$$\boldsymbol{-\frac{r_{L1}}{L_1} i_{L1} + \frac{u-1}{L_1} v_{C1} + \frac{u-1}{L_1} v_{C2} + \frac{v_g}{L_1} + \lambda\left(v_{C2} - v_{ref}\right) = -K_{slide} sgn(\mathbb{S}),} \tag{35}$$

where K_{slide} is positive constant, and s is the sliding surface.

(3) Solve for the control input term u:

$$\boldsymbol{u = \frac{\left[r_{L1} i_{L1} + v_{C1} + v_{C2} - v_g - \lambda L_1\left(v_{C2} - v_{ref}\right) - K_{slide} L_1 sgn(\mathbb{S})\right]}{v_{C1} + v_{C2}}} \tag{36}$$

where:

- λ is selected to satisfy the inequality given in Equation (33),
- $\mathbb{S}$ is the sliding surface defined in Equation (25), and
- K_{slide} is a positive constant.

The last step is to tune λ and K_{slide} to provide the desired responses in terms of zero steady state error, disturbance rejection and uncertainty compensation, and to ensure the least chattering in the output as well as in the duty cycle.

6. Stability analysis of the proposed controller

The stability analysis of the system is evaluated by studying the Lyapunov candidate function:

$$\boldsymbol{V = \frac{1}{2}\mathbb{S}^2} \tag{37}$$

where V is the Lyapunov function and $\mathbb{S}$ is the sliding surface. The selected Lyapunov function is positive definite.

By taking the derivative of the Lyapunov function:

$$\dot{\boldsymbol{V}} = \mathbb{S}\dot{\mathbb{S}} \tag{38}$$

In a similar proof to the stability of the Lyapunov function, the system stability is proved if the Lyapunov function is positive definite and its derivative is negative definite. Substituting the expressions of the derivative of the sliding surface, we can get:

$$\dot{\boldsymbol{V}} = (\mathbb{S}).\left(-\frac{\boldsymbol{r_{L1}}}{\boldsymbol{L_1}}\boldsymbol{i_{L1}} + \frac{\boldsymbol{u-1}}{\boldsymbol{L_1}}\boldsymbol{v_{C1}} + \frac{\boldsymbol{u-1}}{\boldsymbol{L_1}}\boldsymbol{v_{C2}} + \frac{\boldsymbol{v_g}}{\boldsymbol{L_1}} + \boldsymbol{\lambda}\left(\boldsymbol{v_{C2}} - \boldsymbol{v_{ref}}\right)\right) \tag{39}$$

The controller derived in Equation (36) will be substituted into the expression in Equation (39). The final expression is given as:

$$\dot{\boldsymbol{V}} = (\mathbb{S})\left(-\frac{\boldsymbol{K_{slide}}}{\boldsymbol{L_1}}\boldsymbol{sgn}(\mathbb{S})\right) = -\frac{\boldsymbol{K_{slide}}}{\boldsymbol{L_1}}|\mathbb{S}| \tag{40}$$

The result in Equation (40) states that the derivative of the Lyapunov function ($\dot{V}$) is negative definite which proves that the system is globally asymptotically stable.

This result can be visualized by recalling the reachability condition:

$$\frac{1}{2}\frac{d}{dt}\mathbb{S}^2 \leq -\eta|\mathbb{S}|$$

The expression can be simplified to be:

$$\mathbb{S}\dot{\mathbb{S}} \leq -\eta|\mathbb{S}|$$

By carrying the same previous steps of substituting the derived control law in $\dot{\mathbb{S}}$, we get the following result:

$$-\frac{K}{L_1}|\mathbb{S}| \leq -\eta|\mathbb{S}|$$

Thus, by proper assignment of η, the reachability to the sliding surface is ensured and the convergence rate will be given as:

$$time_{\text{reach surface}} \leq \frac{\mathbb{S}(t=0)}{\eta}$$

Hence, by proving that the rate of change in the surface is negative definite, then the system is globally asymptotically stable.

7. Results

7.1. Simulation results: Type II compensator, integral LQR, proposed controller

Simulating the designed controller and assessing its dynamic behaviour is an essential step before experimentally implementing and testing the developed controller. A MATLAB/Simulink simulation was conducted with the switched nonlinear model rather than an averaged model as an essential first step to validate a model that is as close as possible to a practical scenario. The simulation results were generated for the SEPIC converter using the parameters given in **Table 1**. The comparative evaluation and the analysis cover the three discussed controllers: (a) Type-II compensator, (b) integral LQR, and (c) the proposed ISMC. For all three controllers, the following three test conditions were applied: Cold start-from-rest test, input voltage disturbance test, and load disturbance test.

Converter start-from-rest test:

This test investigates the output voltage of the converter when all the initial conditions are at rest (assumed to be zero). The test results for the three compensators are shown in **Figure 10(a–c)** for the output voltage of the SEPIC converter and **Figure 11(a–c)** for the converter duty cycle, respectively.

a) The Type-II compensator controller resulted in an overdamped response and achieved the tracking task with zero steady-state error with a settling time of 40 ms, as shown in **Figure 10(a)**. **Figure 11(a)** shows the corresponding generated duty cycle by the compensator, and it is evident that it does not have a high ripple. This result is critical to validating the design and moving it from a simulation environment to an experimental model.

b) The integral LQR compensator resulted in a response where the output voltage reached the steady state in a settling time of 10 ms. **Figure 10(b)** shows that the designed compensator resulted in making the system reach the steady state with an overdamped response and perform the tracking task with zero steady-state error. **Figure 11(b)** shows the corresponding generated duty cycle by the compensator where it has a low ripple, and this result is critical in validating the designed controller.

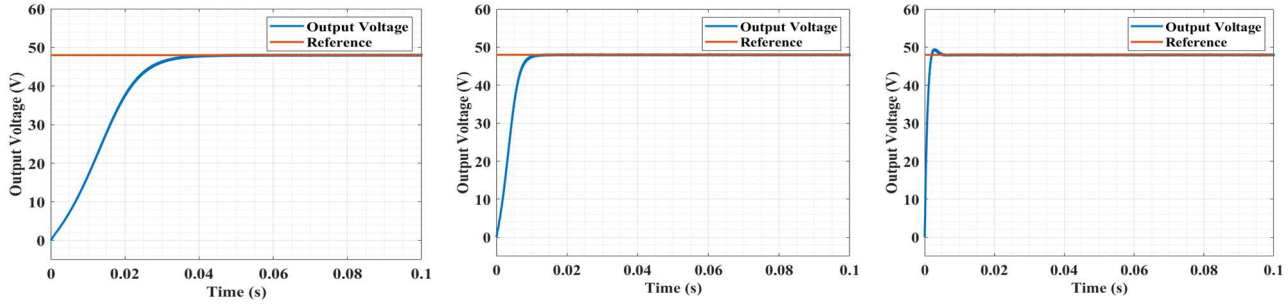

Figure 10. Converter's output voltage at cold start test **(a)** Type-II; **(b)** integral LQR; **(c)** proposed ISMC.

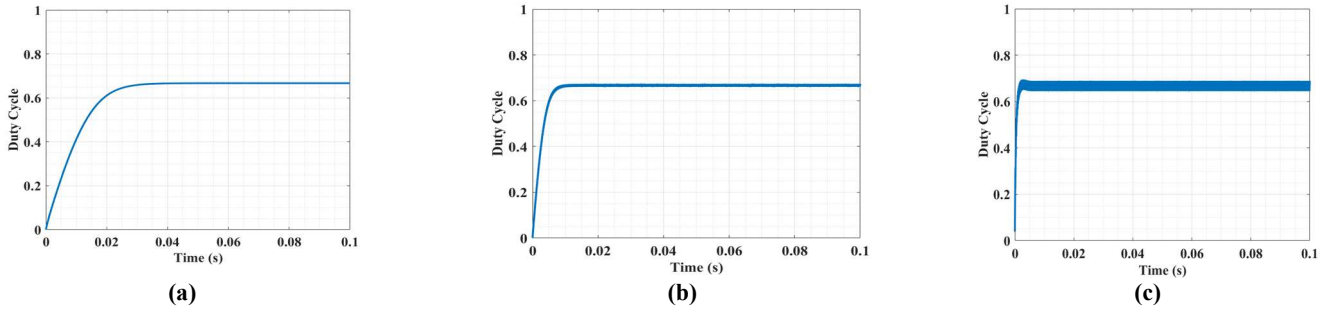

Figure 11. Converter's duty cycle at cold start test **(a)** Type-II; **(b)** integral LQR; **(c)** proposed ISMC.

c) The results of the proposed ISMC controller under the cold start test are depicted in **Figures 10(c)** and **11(c)**. The results show that the converter output voltage reaches the desired output level in 5 ms, and the transient shows a minor overshoot that peaked at 49.6 V (3.3% overshoot). Moreover, the converter using the proposed controller can perform the tracking task with zero steady-state error in the output voltage. Additionally, **Figure 10(c)** shows that after reaching the steady state, the converter output voltage is stable with minimum chattering.

These results are achieved because of the advantages of the proposed ISMC sliding surface, which is based on using the input current (inductor current) and the integral of the output voltage error. The proper design of the surface ensures the system will reach the sliding surface and continue to stay on it. By residing within the sliding surface and sliding on it, the desired point will always be reached. This process ensures smooth transients and reduced chatter in the converter's duty cycle D at steady state, as shown in **Figure 11(c)**. This is typically relevant in applications where the converter is expected to periodically start and stop. It is noted that the dynamics of the duty cycle reflect the output voltage. As shown in **Figure 11(c)**, the duty cycle reaches a steady state in 5 ms with low chattering. This behaviour is identical to that of the output voltage. In fact, verifying the behaviour of the duty cycle in a DC-DC power converter simulation is essential to proving that the converter and its controller have been well designed and that the output voltage behaviour is adhering to the dictated behaviour of the duty cycle. The aforementioned discussion illustrates the advantages of the proposed controller, as the obtained system response does not need to use soft starting techniques/circuits since the response is faster than the other designed controllers.

In summary, this section highlights the first test, where the converter was tested using the three examined controllers under the cold start condition. The study established the Type-II compensator as a benchmark for the analysis and comparison against the integral LQR and the proposed ISMC controllers. The main challenge in this test is starting from zero initial conditions, i.e., charging the storage elements of the SEPIC converter is part of the dynamics when starting from zero. **Table 4** summarizes the results of the simulated cold start test using the three controllers.

Table 4. Comparison of simulation results for the cold test.

Cold start test			
	Type-II	**Integral LQR**	**Proposed ISMC**
Response	Overdamped	Overdamped	Close to critically damped
Settling time	50 ms	10 ms	5 ms

The summarized results state that the Type-II compensator has an overdamped response, and it took 50 ms to reach the steady state. The integral LQR controller had a similar result where the response was overdamped and required only 10 ms to reach steady-state. On the other hand, the proposed controller was much faster, with only a minor overshoot in the output voltage response, and required only 5 ms to reach the steady state. This is 2 times faster than the integral LQR and 10 times faster than the Type-II compensator. During the test, the overshoot reached 49.6 V (3.3% overshoot), given that the input reference is a step function. This overshoot is small, and if the system requires the response to be without an overshoot, then the reference can be adjusted to be a ramped input until the reference reaches the desired level. It should be noted that a ramping reference is a common practice in power electronics to avoid inrush currents in the system. Moreover, the proposed ISMC controller can be tuned easily by re-adjusting the λ value. Hence, if the goal is to achieve a cold start using a step function input without an overshoot, then the designer can reduce the used λ value accordingly until the desired response is achieved.

The depicted results of the cold start test in previous sections showed that the output voltage from the proposed controller has a low ripple like the linear controllers' case. Sliding mode controllers usually suffer from chattering in the output response if a "sign" function is used as part of the controller. This result demonstrates that the design procedure is based on the relationship between the converter states on the newly constructed surface. Furthermore, the scaling gain constant, λ, has been bounded, to ensure system stability with low chattering behaviour. Another point to highlight is the choice of operating the system on a fixed frequency. This reduces the chattering as the converter internally sees an equivalent DC value for the duty cycle D; this makes the converter operate in PWM mode, which effectively results in a low ripple system if the converter components are well-sized.

Input voltage disturbance test:

In this test, the three compensators using the SEPIC converter are evaluated against an input voltage disturbance. Each compensator performance is evaluated in two stages: in the first stage, the converter is subjected to a single disturbance; and in the second stage, the converter is subjected to multiple input voltage disturbances by stepping it down from 24 V to 12 V and then to 6 V. This type of disturbance in the input voltage is considered severe and may be considered out of range for some applications; however, it is of importance in applications where a wide range of input voltages are expected (e.g., different batteries, universal AC input, or use of ultracapacitors). It is noted that the load is kept constant at its nominal value during this test.

a) For the Type-II compensator, after reaching the steady-state condition, the input voltage is stepped down from 24 V to 12 V at 0.1 s, as shown in **Figures 12(a)** and **13(a)**. In this test, the compensator was able to recover from the disturbance in 25 ms. As shown in the figure, the response suffers from a deep undershoot that dropped to 6.8 V. Furthermore, during the recovery process, the response was oscillatory. By varying the input voltage by 50%, the obtained results are not as desired in the power electronics field, as the response is slow, has a large undershoot, and exhibits a large oscillatory response. In the second stage, the converter is subjected to the same previous disturbance at 0.1 s, then another disturbance is introduced at 0.2 s, where the input voltage is reduced from 12 V to 6 V. As shown in **Figures 14(a)** and **15(a)**, the output voltage in the second disturbance has dropped from 48 V to 11.5 V, and it recovered from the disturbance in 15 ms. As depicted in **Figures 12(a)**–**Figure 15(a)**, the response suffers from a deep undershoot, a sluggish response, and oscillations in the recovery process. During this test, the duty cycle is shown in **Figure 16(a)**. The result shows that the corresponding duty cycle has a low ripple, and it is implementable in the experimental setup. Furthermore, the duty cycle corresponds to the output voltage behaviour, where the compensator takes time to adjust the duty cycle; hence, the sluggish response is justified.

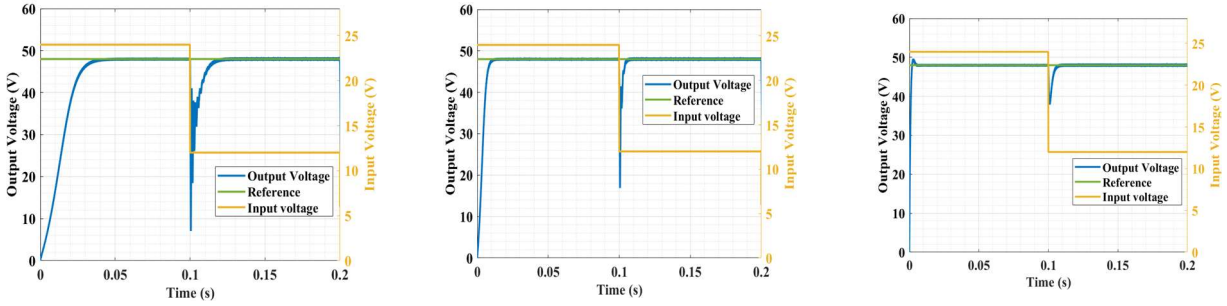

(a) **(b)** **(c)**

Figure 12. Step change in the input voltage from 24 V to 12 V at t = 0.1 s and the corresponding output voltages. **(a)** Type-II compensator; **(b)** integral LQR; **(c)** proposed ISMC.

b) For the integral LQR controller, after reaching the steady-state condition, the input voltage is stepped down from 24 V to 12 V at 0.1 s, as shown in **Figures 12(b)** and **13(b)**. In this test, the compensator was able to recover from the disturbance in 5 ms. As shown in **Figures 14(b)** and **15(b)**, the response had an undershoot with oscillations that dropped as low as 17 V. By comparing the results, it is concluded that the integral LQR controller resulted in a faster response and better undershoot peak; however, the system is still exhibiting an oscillatory behaviour in withstanding the 50% variation in input voltage disturbance. As stated earlier, the disturbance in input voltage will be validated through two cascaded disturbances/ stages. The first-stage results have been depicted in **Figure 12(b)**. In the second stage, first the converter is tested as in case one, then another disturbance is introduced at 0.2 s, where the input voltage is reduced again from 12 V to 6 V. As shown in **Figure 14(b)**, at the first disturbance, the output voltage dropped to 17 V and then recovered from the disturbance in an oscillatory response in 5 ms. The output voltage in the second disturbance dropped from 48 V to 22.5 V, then it showed another overshoot that reached 51.8 V before starting the recovery process. The system, after the second disturbance, reached a steady state again in 7 ms. As depicted in **Figures 12(b)**–**Figure 15(b)**, the response suffers from undershoot, overshoot, and oscillations during the recovery process. During this test, the duty cycle was recorded in **Figure 16(b)**. The result shows that the corresponding duty cycle has a low ripple, and it is implementable experimentally.

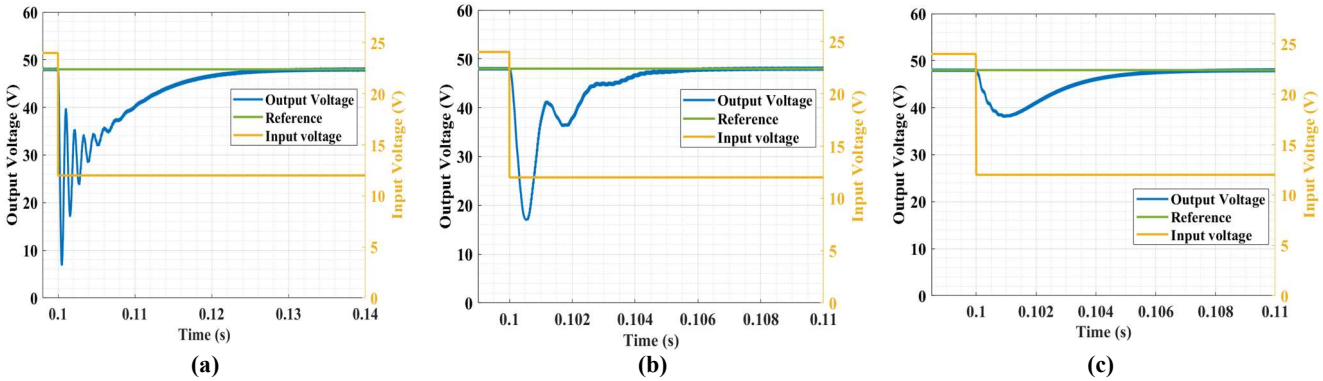

(a) **(b)** **(c)**

Figure 13. Zoomed portion during the step change in the input voltage from 24 V to 12 V at t = 0.1 s. **(a)** Type-II compensator; **(b)** integral LQR; **(c)** proposed ISMC.

c) Like Type-II and the integral LQR controller, the proposed ISMC is subjected to multiple input voltage disturbances in the same manner. The test is conducted after waiting for the system to reach the steady-state condition; then, the input voltage is stepped down from 24 V to 12 V at 0.1 s, as shown in **Figure 12(c)**. The zoomed portion of the response is shown in **Figure 13(c)**. The proposed ISMC provides a smooth, damped transient without oscillation in 6 ms, while the maximum undershoot peak reaches 38.5 V. By observing the ripple on the output voltage, the ripple increased by 0.2% after disturbing the input voltage by 50% from its initial value. In **Figures 14(c)** and **15(c)**, at $t = 0.2$ s, the input voltage is once again stepped down from 12 V to 6 V. During this disturbance, the voltage dropped to 36 V, and the controller required 13 ms to reach stability. The proposed ISMC does not result in any oscillations in the output voltage, as is evident in **Figures 14(c)** and **15(c)**. Similar observations can be made by examining the duty cycle (control input) shown in **Figure 16(c)**. This proves the validity and robustness of the proposed ISMC performance, despite the severity of the applied disturbance.

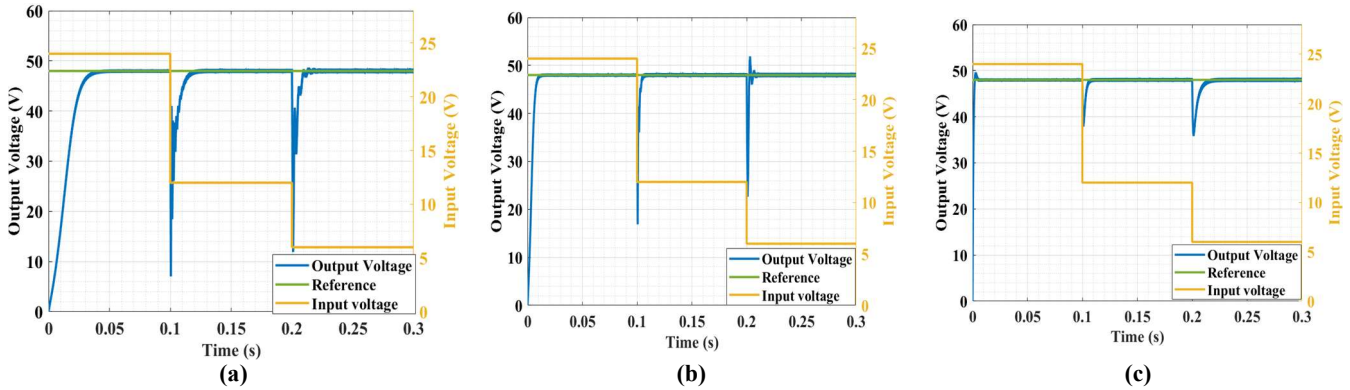

Figure 14. Second step change in the input voltage from 12 V to 6 V at $t = 0.2$s, and the corresponding output voltages. **(a)** Type-II compensator; **(b)** integral LQR; **(c)** proposed ISMC.

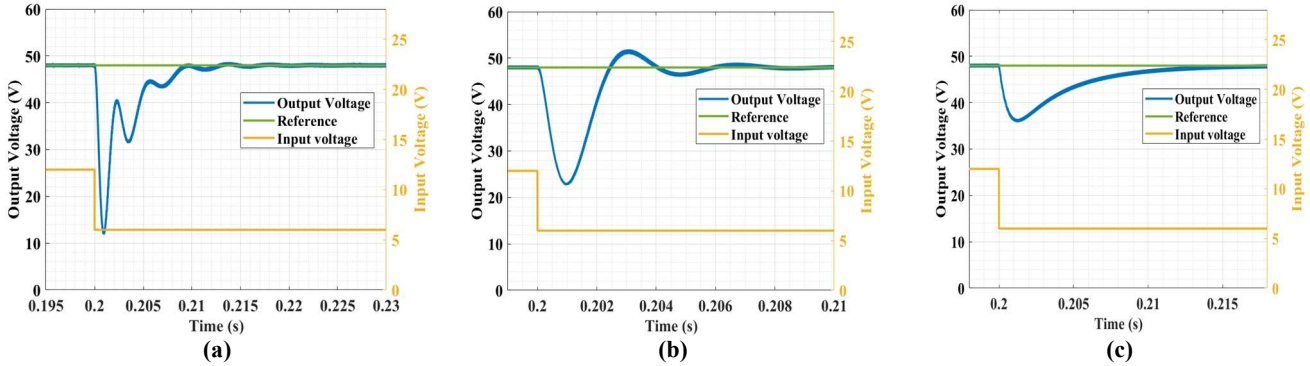

Figure 15. Zoomed portion of output voltage during the second disturbance at 0.2 s where input voltage changes from 12 V to 6 V. **(a)** Type-II compensator; **(b)** integral LQR; **(c)** proposed ISMC.

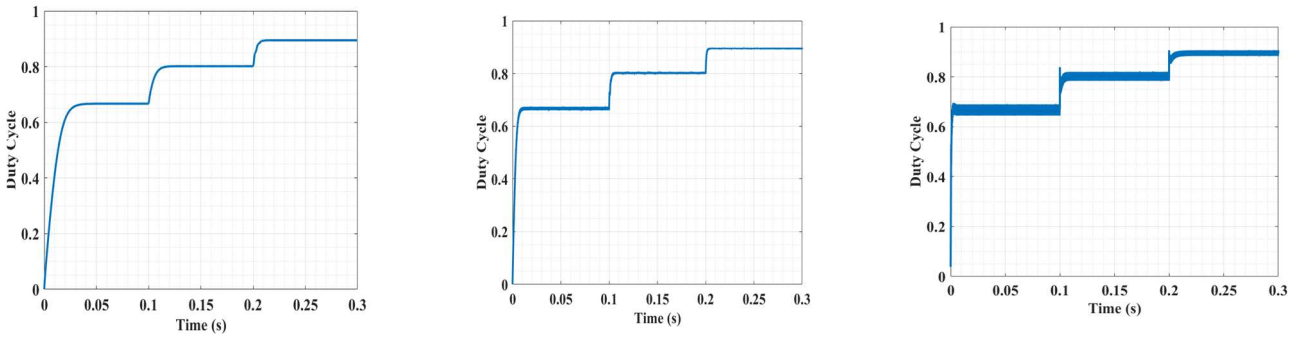

Figure 16. Controller duty cycles '*D*' throughout the different input voltage disturbances. **(a)** Type-II compensator; **(b)** integral LQR; **(c)** proposed ISMC.

In summary, this section covers the second test case, where the system was subjected to cascading severe disturbances in the input voltage. Studying the summary of results, as shown in **Table 5**, highlights the advantages of the proposed ISMC with respect to the other linear controllers. The results depicted in previous sections show that all the controllers can reject a disturbance in the input voltage up to 75% from the nominal state, which is 24 V. Although the proposed ISMC controller in this test is comparable to the Type-II compensator and relatively slower than the integral LQR controller, the ISMC controller offers other features that make it better than the discussed controllers. For instance, the output voltage dropped only to 36 V from 48 V due to the disturbance, while the voltage dropped to 22.5 V and 11.5 V in the case of the integral LQR and Type-II compensator, respectively. On a percentage basis, the 75% input voltage disturbance resulted in a deviation of 25%, 53%, and 76% for the ISMC, integral LQR, and Type-II compensators, respectively. This shows the significant advantage of the proposed ISMC.

Another point to highlight for the proposed ISMC is that the output voltage returns to the steady state after the disturbance in an oscillation-free response, unlike the case of the other linear compensators. This point is crucial in applications where fluctuations on the voltage rail can impact other sub-systems in the entire system. For instance, if the converter output is an input stage to another converter (such as motor inverters), then fluctuations in the first stage DC-DC converter output rail may disturb the second stage. Nevertheless, the proposed ISMC controller offers a smooth response for such cases where the input voltage may be disturbed by 75%. Furthermore, for this disturbance, the ripple in the output voltage does not have a noticeable increase after the disturbance is applied. This is categorized as a prime success in the design where the chattering is minimal, although the input disturbance is as high as 75%.

Table 5. Comparison of simulation results for input voltage disturbance.

Input voltage disturbance test			
	Type-II	**Integral LQR**	**Proposed ISMC**
Percentage change in input voltage	75%	75%	75%
Peak drop in output voltage	11.5 V	22.5 V	36.0 V

Table 5. (*Continued*).

Input voltage disturbance test			
	Type-II	**Integral LQR**	**Proposed ISMC**
Oscillations in response	Yes-severe	Yes-moderate	No
Settling time	15 ms	7 ms	13 ms

Load disturbance test:

The goal of this test is to investigate the converter response following a load disturbance. In this test, the converter will be subjected to 100% load variation to assess the controller's response under extreme conditions. The test demonstrates a severe condition as the load is varied by 100%, which results in doubling the delivered load current. During this test, the input voltage is kept constant at 24 V. After that, the load was varied by 100%, and the load resistance was dropped from 46 **Ω** to 23 **Ω**. This resulted in the delivered current increasing from 1.04 A to 2.08 A.

a) Using a type II compensator, the test resulted in oscillatory behaviour in the output voltage. The response shows an overshoot peaking at 52.5 V, followed by an undershoot peaking at 41 V. The transient in this test took 3.5 ms to settle and reach steady-state. Like the previous tests, the oscillatory behaviour is high and not desired in the response. **Figure 17(a)** shows the output voltage response under this load disturbance, and **Figure 18(a)** shows a zoomed capture of this response.

b) Simulating an integral LQR controller resulted in the results that are shown in **Figure 17(b)**. Analysing the depicted results shows that the test resulted in oscillatory behaviour in the output voltage. The response shows an overshoot that is contained within the 2% settling time criteria, followed by an undershoot that peaked at 41 V. The transient in this test took 2.5 ms to reach steady-state. Like the previous tests, the oscillatory behaviour is high, and it is not desired in the response. **Figure 18(b)** shows a zoomed capture of this response.

c) The proposed ISMC controller was tested for this case. The output voltage response under this test is shown in **Figure 17(c)**. Studying the results in **Figure 17(c)** concludes that the proposed controller can reject extreme variation in the load as a disturbance. The response has no oscillation, despite the significant change in the load. The designed controller was able to reject the disturbance in 6 ms, and the peak during the transient process reached 36 V. Furthermore, the compensator was able to reject the disturbance without compromising the output voltage ripple, unlike the case with linear compensators. The smooth response and low ripple system are desired features in the power converter field that the proposed ISMC can offer, unlike the discussed linear compensators. **Figure 18(c)** shows a zoomed capture of this response.

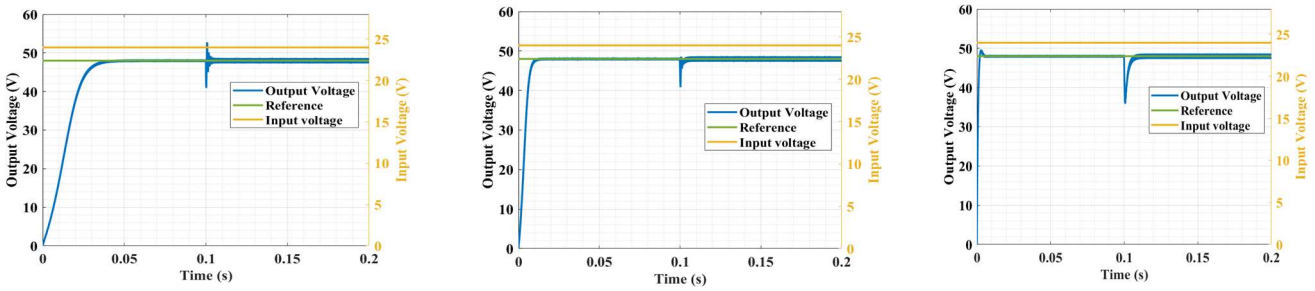

Figure 17. Output voltage at case 4: **(a)** Type-II; **(b)** integral LQR; **(c)** proposed ISMC.

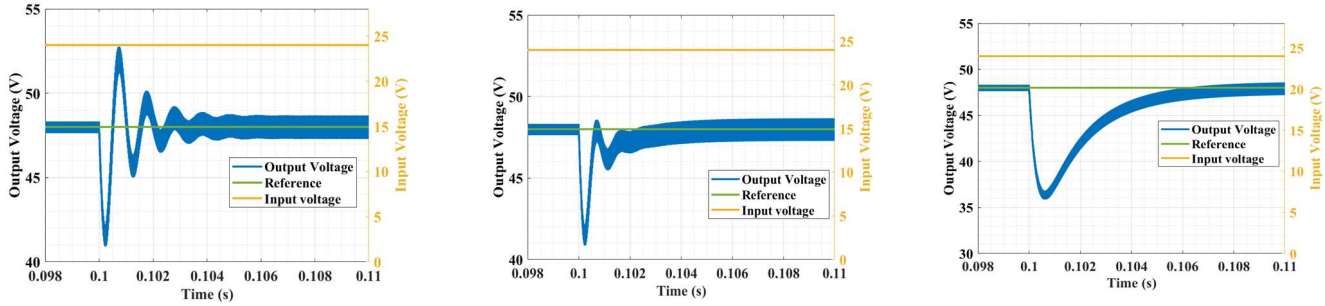

Figure 18. Zoomed portion of the output voltage at case 4: **(a)** Type-II; **(b)** integral LQR; **(c)** proposed ISMC.

In summary, this sub-section shows the results of testing the system against load disturbances. This is to investigate how well the compensator can operate under severe conditions. The following analysis focuses on the fourth stage. A summary of the results is highlighted in **Table 6**. Analyzing the obtained results as per **Table 6** concludes that in terms of the undershoot, once the load is changed from 46 to 23 **Ω**, both linear controllers are comparable, as the voltage dropped to 41 V while using the proposed ISMC, the voltage dropped to 36 V. From the settling time perspective, the linear controllers required 3.5 ms and 2.5 ms for Type-II and integral LQR controllers, respectively. The proposed ISMC required around 6 ms to recover from the transient. The key point and the advantage that the controller is bringing to the discussion is its ability to reject the disturbance in a response that is oscillation-free. Type-II and integral LQR controllers were able to reject the disturbance faster than the proposed ISMC; however, both linear controllers suffered from oscillations during the recovery process, and this would make the response unacceptable in the power electronics field. This is because having an oscillation may impact the performance of other stages and may drive the system out of stability if the other stages are not designed to tolerate such oscillations in the response. It should be noted that the output voltage did not suffer from high chattering using the ISMC. This is evident from analysing the ripple of the output voltage, where the maximum ripple did not exceed 2 V under 100% load variation. As discussed, this outstanding outcome is a result of the proper design of the sliding surface, proper selection of $\boldsymbol{\lambda}$ term, and selecting the system to operate on a PWM fixed frequency.

Table 6. Comparison of simulation results for load disturbance-derated system.

Load disturbance test 46–23 Ω			
	Type-II	**Integral LQR**	**Proposed ISMC**
Load variation	100%	100%	100%
Peak drop in output voltage	41 V	41 V	36 V
Oscillations in response	Yes-severe	Yes-moderate	No
Settling time	3.5 ms	2.5 ms	6 ms

7.2. Experimental results: Derated system: Type-II and proposed Controllers

In this section, the experimental work on the designed converter was conducted at derated power of 24 W, where the load was changed to 24 Ohm. The experimental work used the components summarized in **Table 7**. Following the simulation testing plan, the experimental work will be conducted under the same tests and conditions. In other words, this section will investigate the designed Type-II compensator as well as the proposed ISMC experimentally. Within all the next tests, Type-II compensator is $G_{comp} = \frac{5392.20s+6857734.57}{3337.37s^2+6857734.57s}$, while for the proposed controller, the Lambda (λ) is set at 400.

Case 1: Cold start test:

In this case, the converter using the controller of interest is tested experimentally where it starts from rest and all the initial conditions are zero.

Table 7. Component list to conduct the experimental work.

Components	**Part number**
SEPIC converter	As developed in **Table 1**
Main power supply	ITECH—IT6006C-500-40
Auxiliary power supply	KORAD KA6003P
Oscilloscope	ROHDE & SCHWARZ RTB2004
Differential probe	CAL Test—CT3683
Voltage probe	ROHDE & SCHWARZ RT-ZP10
Microcontroller	Texas Instruments LAUNCHXL-F28069M

The test outcomes are summarized in the following points:

a) For the Type-II compensator, the output voltage response is shown in **Figure 19**. The figure shows the output voltage, and the horizontal and vertical divisions are 5 V and 20 ms, respectively. Analyzing the results in **Figure 19** highlights the following facts: The output voltage response is overdamped, and no oscillations are observed during the transitions. Having an overdamped response is a highly desirable feature in a power converter; nevertheless, the response took 70.7 ms to reach the steady state. Furthermore, the steady-state value of the output voltage is 23.3 V, which corresponds to a 2.91% steady-state error.

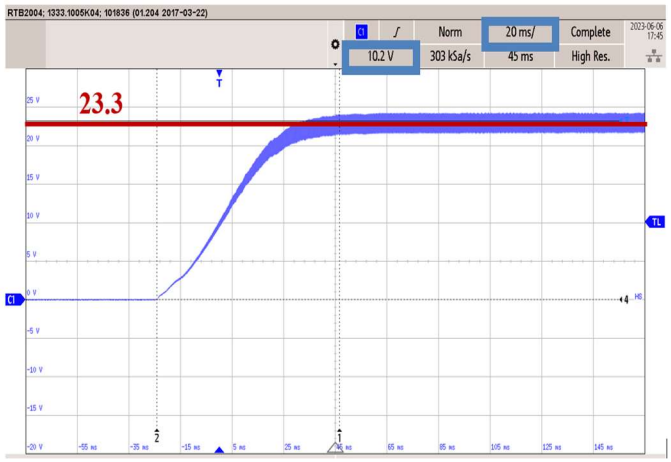

Figure 19. Voltage response for the de-rated power scenario using Type-II compensator-experimental result.

The required time to reach steady-state with respect to switching frequency is relatively extremely high and not desirable although the response is overdamped.

b) For the proposed ISMC, the output voltage response is shown in **Figure 20**. The figure shows the output voltage, and the horizontal and vertical divisions are 10 V and 2 ms, respectively. Studying the results in **Figure 20** shows the output voltage response has an overshoot that reaches 29 V with a settling time of 5 ms, with no other oscillations observed during the transitions. The response is very close to an overdamped response, which is desirable in a power converter, as well as being much faster than Type-II compensators. The steady-state voltage is at 25 V, which translates to 4.17% steady-state error, which is less than 5% acceptance criterion.

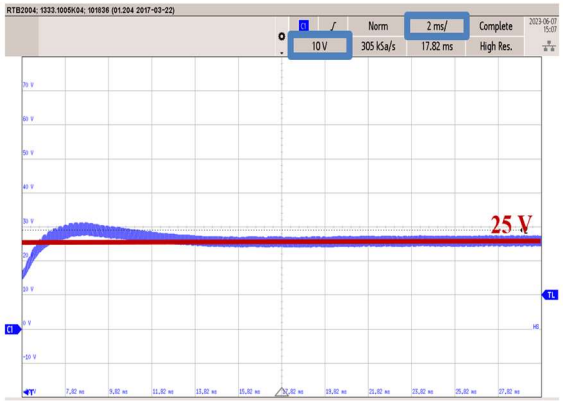

Figure 20. Voltage response for the de-rated power scenario using proposed ISMC-experimental result.

In summary, the cold start is implemented by turning on the system from rest and then waiting for the system to reach steady state. The main challenge in this test is starting from zero initial conditions (i.e., charging the storage elements of the SEPIC converter is becoming part of the picture where their status is starting from zero). **Table 8** summarizes the results of the experimental cold start test using the Type-II compensator vs. the proposed ISMC controller.

Table 8. Comparison of experimental results for cold test- derated system.

Cold start test		
	Type-II	**Proposed ISMC**
Response	Overdamped	Underdamped-close to critical damped
Settling time	70.7 ms	5 ms

The summarized results state that the linear compensator, Type-II compensator, has an overdamped response, and it took 70.7 ms to reach the steady state. On the other hand, the proposed controller was much faster, although there was a minor overshoot in the output voltage response. Specifically, the proposed ISMC controller required 5 ms to reach steady and this is approximately 14 times faster than the classical linear controller. During the test, the overshoot has reached 29 V, given that the reference is the step function. Ideally, an overshoot may not be a desirable feature in the power converters; however, in power electronics field, the reference is provided typically in a ramp function format to eliminate such overshoots that appear if the reference is a step function. Moreover, the proposed ISMC controller can be tuned easily by readjusting the λ value. Hence, if the goal is to achieve a cold start using the step function without an overshoot, then the designer can reduce the used λ value accordingly until the desired response is achieved.

Studying the depicted results of the cold start test results in observing that the output voltage from the proposed controller has a low ripple, around 2 V (pp), which is like the linear case. Sliding mode controllers usually suffer from a chattering in the output response if a sign function is used as part of the controller. This result emphasises the contribution of this work, as the design procedure is based on understanding and analyzing the relationship between the converter states on the novel constructed surface. Furthermore, the scaling constant, λ term, has been bound in this work to ensure system stability with lower chattering behaviour. Another point to highlight, is the selection of operating the system on a fixed frequency has a contribution to reducing the chattering as the converter internally is seeing an equivalent DC value of the duty cycle; this makes the converter operate in PWM mode, which effectively and inherently results in a low ripple system if the converter components are well sized and selected.

Case 2: Input voltage disturbance test:

After reaching steady-state, the input voltage is step changed from 12 V to 5 V (i.e., 58.3% disturbance). The results of this test are presented next:

a) Using the Type-II compensator, the output voltage response (**Figure 21**) shows the output voltage (in blue) as well as the input voltage (in magenta). The input voltage is stepped down to 5 V because, as confirmed by the simulation environment, 5 V is the lowest input that the compensator can tolerate to output 24 V while the power is at 24 W. Investigating the depicted results shown in **Figure 21** shows that the output voltage exhibited very minor oscillations during the transient process. Further, the output voltage dropped from 24 V to 8 V, where the settling time is around 25 ms. It should be noted that there was a minor tracking error before and after the test. Before applying the voltage disturbance, the output voltage at steady-state was 23.3 V (2.91% error), while after the test,

the steady-state value became 24.8 V (3.33%).

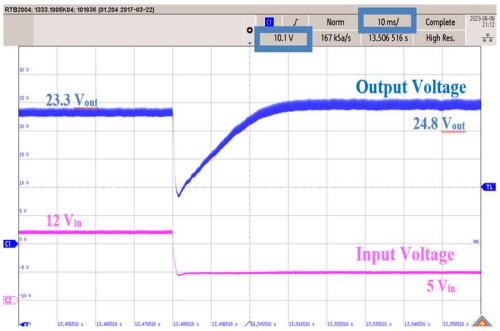

Figure 21. Voltage response for the de-rated power scenario using Type-II compensator-experimental result for input voltage disturbance.

b) Using the proposed ISMC, the input voltage is stepped down from 12 V to 3.5 V, which is equivalent to a 70.8% disturbance from the nominal input voltage. The corresponding results of this test in terms of output voltage response are shown in **Figure 22**. The figure shows the output voltage as well as the input voltage in blue and magenta traces, respectively. The vertical divisions for both measurements are in 10 V, while for the time scale, the divisions are in 5 ms. In this test, the input voltage was reduced to 3.5 V. The input voltage has been stepped down to 3.5 V because this is the lowest input that the compensator can tolerate to output 24 V at a 24 W load size. Therefore, stepping down the input voltage to 3.5 V is the maximum extreme condition that the system can be subjected to and tested against. Investigating the depicted results shown in **Figure 22** shows that the output voltage does not exhibit any oscillations during the transient process. Also, at the time of the disturbance, where the input voltage changed to 3.5 V, the output voltage dropped to 10 V, and it took 8 ms to recover from this disturbance. The obtained output voltage profile is highly favorable in the field of power electronics as the waveforms do not have any oscillations, yet it is fast enough compared to linear compensators. In terms of steady-state error, the output voltage after the disturbance was 24.4 V, which is equivalent to 1.67%.

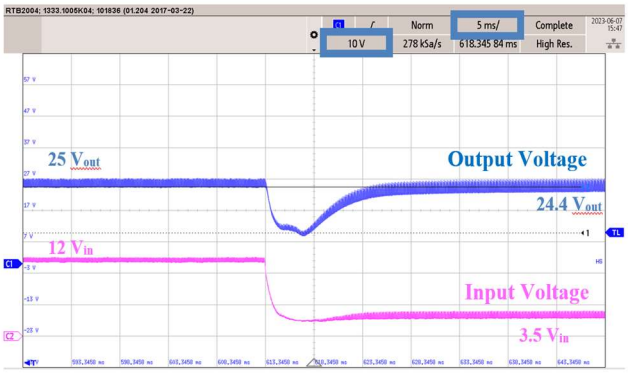

Figure 22. Voltage response for the de-rated power scenario using proposed ISMC-experimental result for input voltage disturbance.

In a nutshell, the system was tested against a severe change in the input voltage in the form of a step disturbance. Studying the summary of the results as shown in

Table 9 highlights the added advantages of the proposed ISMC. Although both controllers were capable of rejecting the introduced step input voltage disturbance, the proposed ISMC figures exceed the performance of the benchmark design Type-II compensator. Experimentally, the proposed ISMC can reject a disturbance up to 70.8% of the nominal input voltage, unlike the linear controller, which can handle up to 58.3% of the of the disturbance. Moreover, the ISMC controller was capable of handling the disturbance better than the linear compensator; this is evident in the output voltage, as the voltage dropped to 10 V in the ISMC case while the output voltage dropped to 8 V in the Type-II compensator case. The time that it took the controller to overcome the disturbance is another factor in comparing the designs. The results in **Table 9** show that the proposed controller is capable of rejecting a 70.8% disturbance in input voltage in 8 ms, which is around 3 times faster than a Type-II compensator. It should be emphasised on the fact that the output voltage in the case of the ISMC controller returns to the steady state after the disturbance introduction in a smooth oscillation-free response, unlike the case of the linear compensator. This point is crucial in applications where fluctuations on the voltage rail can impact the other sub-systems of the entire system. For instance, if the output of the converter is an input stage to other converters, such as motor inverters, then fluctuations on the converter output rail may disturb the second stage, and other considerations should be investigated. Nevertheless, the proposed ISMC controller offers a fast and smooth response in such cases where the input voltage is disturbed. Furthermore, for a disturbance of 70.8% in the input voltage, the ripple has increased to be around 3.75 V from 2 V, which is classified as prime success in the design where the chattering is minimal, although the disturbance was about 70.8% from the nominal case.

Table 9. Comparison of simulation results for input voltage disturbance- derated system.

Input voltage disturbance test		
	Type-II compensator	**Proposed ISMC**
Lowest input voltage	5 V	3.5 V
Max percentage of change	58.30%	70.8%
Peak undershoot in output voltage	8 V	10 V
Oscillations in response	Yes-minor	No
Settling time	25 ms	8 ms

Case 3: Load disturbance test:

In this case, the system is investigated to reject 100% load disturbance. The test procedure will be started by running the converter at a cold start until the output voltage reaches the desired level of 24 V. After that, the load will be changed by 100%, i.e., the impedance will be changed to 12 Ω. Next, the load will be returned to its nominal condition, where the load will be changed from 12 Ω to 24 Ω. The results of the described test are presented next:

a) The zoomed portion of the output voltage response using Type-II is shown in **Figure 23(a,b)**. In both zoomed portions, the figures show the output voltage, while the vertical and horizontal divisions are 14.68 V and 5 ms for the first and

14 V and 10 ms for the second. In the first disturbance scenario, where the load is changed from 24 Ω to 12 Ω, the output voltage displayed oscillations that started with an undershoot that peaked at 17.4 V. The process of recovery from the first disturbance took 20 ms. At the second disturbance, a similar response was obtained, where the response suffered from oscillations that peaked at 30 V. The system took 20 ms to reject the disturbance and return to steady-state. Another observation to note is the level of steady-state voltage before and after the disturbance. Before the first disturbance, the output voltage was 23.3 V, then dropped to 22.7 V after the disturbance; furthermore, it should be noted that after the first disturbance, the ripple increased, which is an expected outcome due to the extreme loading condition. After the second disturbance, where the load changed from 12 Ω to 24 Ω, the output voltage steady-state value changed from 22.7 V to 23.6 V.

b) The proposed ISMC controller resulted in the responses depicted in **Figure 24(a,b)** (zoomed portion). In both zoomed portions, the figures show the output voltage, while the vertical divisions are 10 V. The horizontal divisions are 10 ms and 2 ms for the first and second scenarios, respectively. Studying these responses results in the next observation. In the first disturbance scenario, where the load is changed from 24 Ω to 12 Ω, the output voltage did not have any oscillations in the transients. The response has an undershoot that peaked at 19.6 V, then it reached the steady-state again in a smooth response. The process of recovery from this disturbance took 2 ms. At the second disturbance, a similar response was obtained, where the output voltage had a smooth recovery during the transients. Specifically, the transients started with an overshoot that peaked at 33.6 V, then the output voltage recovered in a smooth response. In this case, the system took 3 ms to reject the disturbance and return to steady-state level. Studying the results shows that the ripple increased after the first disturbance, and this is expected due to the significant loading condition, like in the case of the linear compensator. Another point that should be noted is that after the disturbance, the output voltage at steady-state was 24.7 V, which confirms the design was successful.

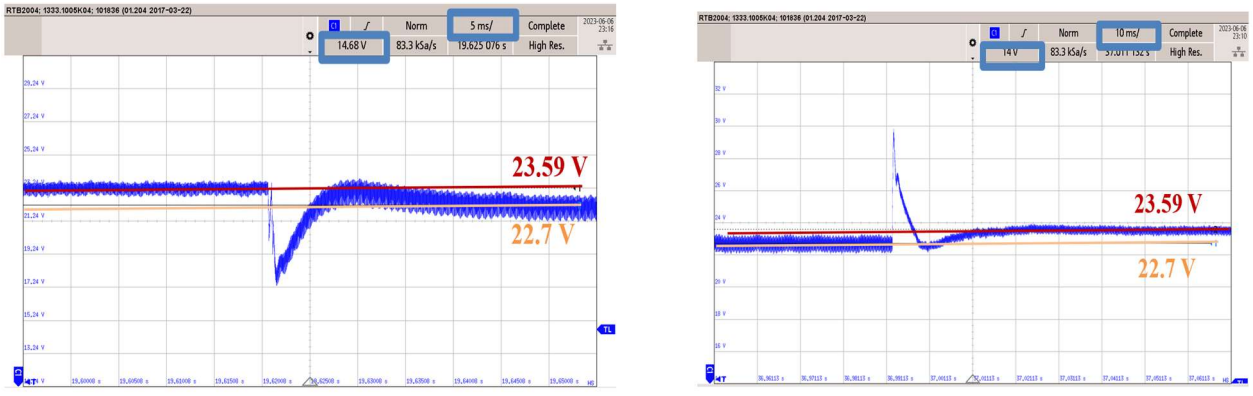

(a) **(b)**

Figure 23. Zoomed portion at voltage response for the de-rated power scenario using Type-II compensator-experimental result for load disturbance from **(a)** 24 Ω to 12 Ω; **(b)** 12 Ω to 24 Ω.

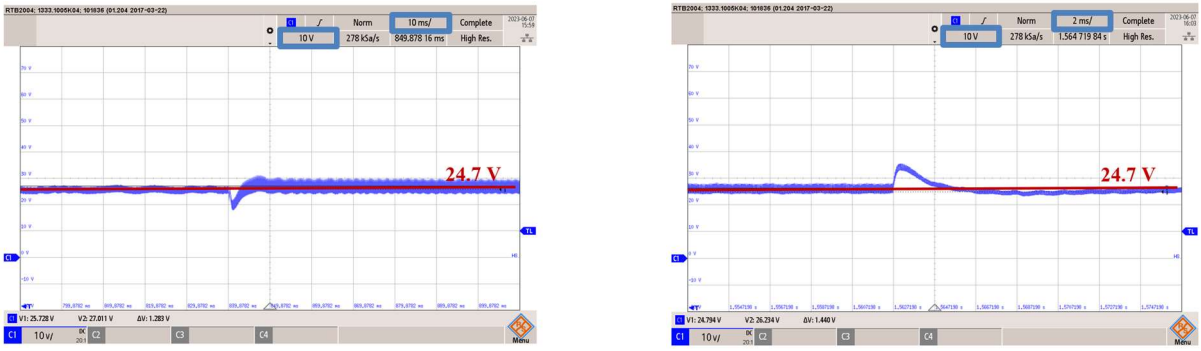

(a) **(b)**

Figure 24. Zoomed portion at voltage response for the de-rated power scenario using proposed ISMC-experimental result for load disturbance from **(a)** 24 Ω to 12 Ω; **(b)** 12 Ω to 24 Ω.

In short, the system was tested against 100% load variation where this test aimed to investigate how well the compensator is capable of operating under severe conditions. A summary of the presented results in the previous subsections under this test case is highlighted in **Table 10**. Analyzing the obtained results as per **Table 10**, it can be concluded that in terms of the undershoot, once the load is changed from 24 to 12 Ω, both controllers are comparable, with a slight advantage to the linear compensator as peak response. Similarly, once the load is changed again from 12 to 24 Ω, both controllers result in an overshoot with a minor advantage towards the linear compensator in terms of the maximum peak value. However, in terms of how smooth the response is, the proposed ISMC is taking the lead. As shown in the previous subsections, the proposed ISMC response does not have any oscillation, whether the load is changed from 24 to 12 Ω or vice versa. On the contrary, the linear compensator response showed an undershoot followed by an overshoot for the 24–12 Ω case and showed an overshoot cascading with an undershoot for the scenario of 12–24 Ω. Having a system with no oscillation sin the recovery process is a highly desirable feature in the power electronics field. This is because having an oscillation may impact the performance of other stages and may drive the system out of stability if the other stages are not designed to tolerate such oscillations in the response. From a settling time perspective, the proposed ISMC controller demonstrates a superior result experimentally. The proposed ISMC controller was capable of rejecting load disturbances 7–10 times faster than the Type-II compensator without having any oscillations in the response. From a power converter perspective, this result brings significant advantages to the field because the response is smooth without compromising the recovery time.

It should be noted that the output voltage in this test for both scenarios did not suffer from high chattering. This is evident through dissecting the ripple of the output voltage, where the maximum ripple did not exceed 5 V under 100% load variation while the ripple is maintained around 2 V whenever the load is back to 24 Ω. This is an outstanding result due to the proper construction of the sliding surface, the proper selection of λ term, and the selection of the system to be operating on a PWM fixed frequency structure.

Table 10. Comparison of simulation results for load disturbance- derated system.

Load disturbance test 24–12 Ω		
	Type-II compensator	**Proposed ISMC**
Load variation	100%	100%
Peak undershoot in output voltage	17.4 V	19.6 V
Oscillations in response	Yes-minor	No
Settling time	20 ms	2 ms
Load disturbance test 12–24 Ω		
	Type-II Compensator	**Proposed ISMC**
Load variation	100%	100%
Peak overshoot in output voltage	30 V	33.6 V
Oscillations in response	Yes-minor	No
Settling time	20 ms	3 ms

8. Conclusion

This work proposes a systematic approach to designing an integral sliding mode controller for a SEPIC converter. Furthermore, the work summarized the design guide for a Type-II compensator as well as an integral LQR where these controllers were compared to the proposed controller. The designed controllers were simulated in a Simulink environment using a switched converter model and then validated through a scaled experimental setup. The hardware results confirm the simulation results, and they show the benefits that can be achieved by designing and implementing the ISMC for SEPIC converter. As highlighted in the literature, one of the prime limitations of using the sliding mode controller in industry is the lack of a standardized approach to design the controller, and this issue was addressed in this work.

Author contributions: Conceptualization, YEH, VS and RM; methodology, YEH, VS; software, YEH; validation, YEH, VS and AS; formal analysis, YEH and VS; investigation, YEH and VS; resources, VS; data curation, YEH and VS; writing—original draft preparation, YEH, VS and AS; writing—review and editing, VS; visualization, YEH, VS and AS; supervision, VS and RM; project administration, VS; funding acquisition, VS. All authors have read and agreed to the published version of the manuscript.

Conflict of interest: The authors declare no conflict of interest.

References

1. Kapat S, Krein PT. A Tutorial and Review Discussion of Modulation, Control and Tuning of High-Performance DC-DC Converters Based on Small-Signal and Large-Signal Approaches. IEEE Open Journal of Power Electronics. 2020, 1: 339-371. doi: 10.1109/ojpel.2020.3018311
2. Ullah Q, Busarello TDC, Brandao DI, et al. Design and Performance Evaluation of SMC-Based DC–DC Converters for Microgrid Applications. Energies. 2023, 16(10): 4212. doi: 10.3390/en16104212
3. Nicola M, Nicola CI, Selișteanu D. Improvement of the Control of a Grid Connected Photovoltaic System Based on Synergetic and Sliding Mode Controllers Using a Reinforcement Learning Deep Deterministic Policy Gradient Agent. Energies. 2022, 15(7): 2392. doi: 10.3390/en15072392

4. Erickson RW, Maksimović D. Fundamentals of Power Electronics. Springer US; 2001. doi: 10.1007/b100747
5. Mohan N. Advanced Electric Drives: Analysis, Control and Modeling Using Simulink by Ned Mohan. Mnpere; 1707.
6. Aroudi AE, Mandal K, Al-Numay MS, et al. Piecewise Quadratic Slope Compensation Technique for DC-DC Switching Converters. IEEE Transactions on Circuits and Systems I: Regular Papers. 2020, 67(12): 5574-5585. doi: 10.1109/tcsi.2020.2993793
7. Deisch C. Simple switching control method changes power converter into a current source. In: Proceedings of the 1978 IEEE Power Electronics Specialists Conference; 13-15 June 1978; Syracuse, NY, USA. pp. 300-306. doi: 10.1109/pesc.1978.7072368
8. Liu YF, Meyer E, Xiaodong Liu. Recent Developments in Digital Control Strategies for DC/DC Switching Power Converters. IEEE Transactions on Power Electronics. 2009, 24(11): 2567-2577. doi: 10.1109/tpel.2009.2030809
9. Khalil H. Nonlinear Systems, 3rd ed. Pearson; 2001.
10. Tan SC, Lai YM, Tse CK. General Design Issues of Sliding-Mode Controllers in DC–DC Converters. IEEE Transactions on Industrial Electronics. 2008, 55(3): 1160-1174. doi: 10.1109/tie.2007.909058
11. Wang J, Rong J, Yu L. Dynamic prescribed performance sliding mode control for DC–DC buck converter system with mismatched time-varying disturbances. ISA Transactions. 2022, 129: 546-557. doi: 10.1016/j.isatra.2022.02.019
12. Buckner GD. Intelligent bounds on modeling uncertainty: applications to sliding mode control. IEEE Transactions on Systems, Man and Cybernetics, Part C (Applications and Reviews). 2002, 32(2): 113-124. doi: 10.1109/tsmcc.2002.801350
13. Pandey SK, Veeranna K, Patil SL, et al. Uncertainty Estimator based Sliding Mode Control Schemes for Multimode Noninverting Buck-Boost DC-DC Converter. IFAC-PapersOnLine. 2020, 53(1): 555-560. doi: 10.1016/j.ifacol.2020.06.093
14. Zhang L, Wang Z, Li S, et al. Universal finite-time observer based second-order sliding mode control for DC-DC buck converters with only output voltage measurement. Journal of the Franklin Institute. 2020, 357(16): 11863-11879. doi: 10.1016/j.jfranklin.2019.11.057
15. Hamed SB, Hamed MB, Sbita L. Robust Voltage Control of a Buck DC-DC Converter: A Sliding Mode Approach. Energies. 2022, 15(17): 6128. doi: 10.3390/en15176128
16. Chincholkar SH, Jiang W, Chan CY. A Modified Hysteresis-Modulation-Based Sliding Mode Control for Improved Performance in Hybrid DC–DC Boost Converter. IEEE Transactions on Circuits and Systems II: Express Briefs. 2018, 65(11): 1683-1687. doi: 10.1109/tcsii.2017.2784549
17. Wang Y, Duan G, Yu J, et al. Harmonic Analysis of Sliding-Mode-Controlled Buck Converters Imposed by Unmodeled Dynamics of Hall Sensor. Energies. 2023, 16(17): 6124. doi: 10.3390/en16176124
18. González I, Sánchez-Squella A, Langarica-Cordoba D, et al. A PI + Sliding-Mode Controller Based on the Discontinuous Conduction Mode for a Unidirectional Buck–Boost Converter with Electric Vehicle Applications. Energies. 2021, 14(20): 6785. doi: 10.3390/en14206785
19. Pandey SK, Patil SL, Phadke SB. Regulation of Nonminimum Phase DC–DC Converters Using Integral Sliding Mode Control Combined with a Disturbance Observer. IEEE Transactions on Circuits and Systems II: Express Briefs. 2018, 65(11): 1649-1653. doi: 10.1109/tcsii.2017.2759908
20. Ghosh SK, Roy TK, Pramanik MdAH, et al. Design of Nonlinear Backstepping Double-Integral Sliding Mode Controllers to Stabilize the DC-Bus Voltage for DC–DC Converters Feeding CPLs. Energies. 2021, 14(20): 6753. doi: 10.3390/en14206753
21. Das S, Salim Qureshi M, Swarnkar P. Design of integral sliding mode control for DC-DC converters. Materials Today: Proceedings. 2018, 5(2): 4290-4298. doi: 10.1016/j.matpr.2017.11.694
22. Bensaada M, Boudghene Stambouli A. A practical design sliding mode controller for DC–DC converter based on control parameters optimization using assigned poles associate to genetic algorithm. International Journal of Electrical Power & Energy Systems. 2013, 53: 761-773. doi: 10.1016/j.ijepes.2013.05.043
23. Komurcugil H. Adaptive terminal sliding-mode control strategy for DC–DC buck converters. ISA Transactions. 2012, 51(6): 673-681. doi: 10.1016/j.isatra.2012.07.005
24. Mahdavi J, Nasiri MR, Agah A, et al. Application of Neural Networks and State-Space Averaging to DC/DC PWM Converters in Sliding-Mode Operation. IEEE/ASME Transactions on Mechatronics. 2005, 10(1): 60-67. doi: 10.1109/tmech.2004.842227
25. Sarkar TT, Mahanta C. Estimation Based Sliding Mode Control of DC-DC Boost Converters. IFAC-PapersOnLine. 2022, 55(1): 467-472. doi: 10.1016/j.ifacol.2022.04.077

26. Gireesh G, Seema PN. High frequency SEPIC Converter with PWM Integral Sliding Mode Control. In: Proceedings of the 2015 International Conference on Technological Advancements in Power and Energy (TAP Energy); 24-26 June 2015; Kollam, India. pp. 393-397. doi: 10.1109/tapenergy.2015.7229651
27. Salazar-Duque JE, Ortiz-Rivera EI, Gonzalez-Llorente J. Analysis and non-linear control of SEPIC dc-dc converter in photovoltaic systems. In: Proceedings of the 2015 IEEE Workshop on Power Electronics and Power Quality Applications (PEPQA); 2-4 June 2015; Bogota, Colombia. pp. 1-6. doi: 10.1109/pepqa.2015.7168243
28. Kavitha A, Indira G, Uma G. Analysis and Control of Chaos in SEPIC DC-DC Converter Using Sliding Mode Control. In: Proceedings of the 2008 IEEE Industry Applications Society Annual Meeting; 5-9 October 2008; Edmonton, AB, Canada. pp. 1-6. doi: 10.1109/08ias.2008.289
29. Ablay G. Robust tracking controller for SEPIC drivers. Electronics Letters. 2016, 52(24): 2007-2009. doi: 10.1049/el.2016.3427
30. Li N, Lin-Shi X, Lefranc P, et al. Universal DC-DC converter using SEPIC. In: Proceedings of the 2011 14th European Conference on Power Electronics and Applications; 30 August 2011–1 September 2011; Birmingham, UK. pp. 1-10.
31. Komurcugil H, Biricik S, Guler N. Indirect Sliding Mode Control for DC–DC SEPIC Converters. IEEE Transactions on Industrial Informatics. 2020, 16(6): 4099-4108. doi: 10.1109/tii.2019.2960067
32. Jaafar A, Godoy E, Lefranc P, et al. Nonlinear sliding mode observer and control of high order DC-DC converters. In: Proceedings of the IECON 2010 - 36th Annual Conference on IEEE Industrial Electronics Society; 7-10 November 2010; AZ, USA. pp. 180-186. doi: 10.1109/iecon.2010.5675208
33. Basso CP. Designing Control Loops for Linear and Switching Power Supplies: A Tutorial Guide. Artech House; 2012.

Energy Storage and Conversion 2024, 2(1), 214.
https://doi.org/10.59400/esc.v2i1.214

Article

Estimation of the hourly solar radiation

Muhammed Fatih Saltuk

Development and Investment Bank of Türkiye, 34764 Istanbul, Turkey; fatih.saltuk@kalkinma.com.tr

CITATION

Saltuk MF. Estimation of the hourly solar radiation. Energy Storage and Conversion. 2024; 2(1): 214. https://doi.org/10.59400/esc.v2i1.214

ARTICLE INFO

Received: 7 November 2023
Accepted: 8 January 2024
Available online: 15 January 2024

COPYRIGHT

Copyright © 2024 by author(s). *Energy Storage and Conversion* is published by Academic Publishing Pte. Ltd. This work is licensed under the Creative Commons Attribution (CC BY) license. https://creativecommons.org/licenses/by/4.0/

Abstract: Hybrid facility investments from renewable energy sources have increased in recent years. In general, solar power is the secondary energy source in hybrid systems. The reason why solar energy is most commonly used in hybrid power systems is that it is cheaper than other types of renewable energy. Solar-Hydroelectric (SHE) is one of the foremost compatible hybrid energy pairs, as solar and hydroelectric power generation profiles complement one another. Hybrid systems consisting of solar and hydropower have complementary characteristics due to the shared use of infrastructure systems and different periodicities in power generation. Energy management is important for SHE-integrated facilities. Since only a limited amount of energy can be injected into the grid from transformer capacities, energy management in hybrid systems is of great importance. To manage energy in hybrid energy systems, the amount of energy that can be produced each hour must be determined. In hybrid energy plants, there is usually already another renewable energy plant in place, and solar energy is added on top and optimized. Since there are no pyrometers in the existing plants, the daily radiation data from the National Aeronautics and Space Administration (NASA) is used, but the daily energy production amount may be insufficient for accurate energy management. To realize this, it's necessary to reveal the energy generation on an hourly basis. During this study, the quantity of radiation on an hourly basis was determined to calculate solar power generation. Empirical and econometric models utilized in radiation amount determination were performed, and the most appropriate method was clarified by comparing them with one another. Hourly-based radiation is achieved with an empirical method by using National Aeronautics and Space Administration (NASA) daily radiation.

Keywords: SHE (Solar-Hydroelectric); energy management; solar radiation

1. Introduction

Energy management and hybrid energy became the most significant issues to ensure the sustainability of energy production. In general, solar energy is the most renewable energy hybrid. Therefore, it's necessary to work out energy generation amounts on an hourly basis and to confirm energy management. Solar energy may be a style of energy that is easily accessible around the globe. Electricity generation from solar energy is within the sort of function of radiation and temperature. Meteorological measurements are made regionally in many parts of the planet. The radiation amount is obtained from satellites. The NASA official website has daily irradiance data for any coordinate on the planet. However, these data must be obtained on an hourly basis for energy management. The quantity of radiation on an hourly basis is obtained by basically two methods. One of them is the empirical method, and the other is the econometric statistical method. During this study, both approaches were run separately and compared with actual data. The literature reviews are given in the following paragraphs. With the widespread use of hybrid energy, energy management is becoming more important. The main reason is that the capacity that can be fed into the

grid does not change, no matter how much the installed power increases. For example, if a wind turbine with an installed capacity of 80 MW, which has the right to inject energy into the grid with an installed capacity of 50 MW, is additionally supported by solar energy with an installed capacity of 100 MW, the amount of energy that the turbine can inject into the grid will not be 180 MW, which is the total installed capacity of the two production facilities, but the amount of electricity injected into the grid will still be 50 MW. Therefore, energy management in hybrid energy systems is critical to the continuity of the system. In hybrid energy, solar energy is mostly used. In hybrid projects using solar energy, the amount of radiation should be determined on an hourly basis to ensure natural and reliable energy management. The amount of radiation is one of the main factors that determines the amount of energy production, as it directly affects the amount of electricity produced by the PV panels. With this study, the solar radiation amounts are accurately and quickly determined every hour and will be used for both efficient power optimization and energy management.

Tırmıkçı used the mathematical models and equations to see the most suitable angle in Sakarya province in her doctoral thesis. During this study, Tırmıkçı revealed a real-time comparison of the two-axis scheme positioned with the sun and therefore the fixed scheme. Tırmıkçı worked on position with the foremost appropriate annual angle [1]. Jacovides et al. stated versatile correlations in determining the hourly solar radiation. During this study, radiation measurements for Cyprus supported the experiment, which was briefly defined empirically by making use of the mathematical models previously stated within the literature studies by other researchers. By calculating the coefficients, hourly radiation is estimated [2]. Iqbal correlated the mean beam with diffuse radiation. Monthly average radiation amounts with the knowledge obtained from the stations for various cities in Canada are calculated [3]. Alsafadi and Başaran Filik used a design algorithm like a machine learning mechanism for hourly solar radiation. Estimated the quantity of radiation on an hourly basis by applying machine learning (ML-machine learning) to empirical models for Eskişehir [4]. Serttaş proposed a brand-new pattern scan-based approach to radiation forecasting [5]. Maleki et al. estimated the global solar radiation on disposed sides. Empirical radiation simulation developed especially within the last ten years for a neighborhood [6]. Chandel and Aggarwal have worked on a one-hour energy model that will provide reliable and accurate finishes up within the western Himalayas. This study has been cited as a reference in many other articles [7].

Khatib and Elmenreich proposed a new approach for obtaining hourly solar radiation. In this study, an artificial neural network is used to generalize daily solar radiation [8]. Berrizbeitia et al. stated an experimental simulation for determining solar radiation. During this study, a review and experimental analysis emphasized that daily radiation amounts are often easily obtained from NASA sources, but it had been emphasized that a model should be developed for the hourly radiation amount obtained on an hourly basis, and empirical coefficients for 19 different regions were tested [9]. Gueymard stated a new estimation approach for solar radiation. During this study, the number of radiations was measured on a monthly and average hourly basis using two new models in line with the information provided by an outsized nation-state and lots of information stations. The empirical coefficients proposed during this study were also utilized in studies conducted by other researchers [10]. Al-Rawahi et al. suggested

a new estimation method for Oman. During this study, the amount of radiation is calculated on an hourly basis from the available daily radiation amounts for Oman [11]. Ishola et al. developed a territorial correction factor for the estimation of hourly-based solar irradiance. A comparison was made specific to the estimation model that determined ten regions for radiation amount and also the coefficients determining the regional radiation [12]. Hussein estimated hourly global radiation in Egypt employing a mathematical model. A mathematical model prediction calculates the amount of radiation for Egypt on an hourly basis using meteorological data [13]. Within the studies examined, general and conceptual models were formed by fitting and measurements made in numerous parts of the world and at different times into mathematical models [1–13]. Among these models, mathematical models and experimental coefficients, which are briefly called empirical, were employed within the studies created by Maleki et al. [6], Chandel and Aggarwal [7], Gueymard [10]. In addition to empirical coefficients and prediction models, statistical models are also used when determining the quantity of radiation. When using statistical models, forward-looking estimations are made by using mostly actual data. In regions where data is going to be obtained on an hourly basis, high correlation results are often obtained due to statistical methods. Huang et al. forecasted solar radiation by continuously employing some auto-regressive and space (CARDS) models. During this study, the authors emphasized that the amount of radiation is seriously tormented by weather changes like cloudiness. In this case, the only approaches today are statistics. It's stated that some methods exist in computing networks, and random variables are called stochastically. Within the study, a self-connected (AR-autoregressive) model is used together with a dynamic system model. As a result of the study, it was stated that the proposed system confirmed and improved the predictions by around 30% [14]. Mbaye et al. estimated the solar availability of the Dakar site by using the ARMA model. A self-correlated dynamic average (ARMA-autoregressive moving average) model was used for short-term radiation estimation. Data and validations were obtained from a station located in Dakar. The data represent the period the period between October 2016 and September 2017 and are presented on an hourly basis. As a result of the study, it was emphasized that the ARMA method is reliable [15]. Adejumo and Suleiman estimated solar irradiance by using the ARMA-GARCH approach. A combined self-correlated dynamic mean model (ARMA) and a generalized self-correlated and variable conditions model (GARCH-generalized autoregressive conditional heteroscedasticity) were employed during this study. For the southern element of Nigeria, an estimate was made for the amount of radiation [16]. Ghofrani and Alolayan used statistics for renewable energy forecasting. They stated statistics and connections that will be used for renewable energy and gave information about their general framework [17]. Hassan et al. estimated the daily-based solar radiation of the United Arab Emirates (Al-Ain) by using an econometric statistics model. During this study, statistic connection models (ARIMA) radiation amount estimates, including autoregressive integrated moving averages, were used. 10 years of knowledge were taken (1995–2004), and a two-year estimation (2005–2007) was made within the sunshine of these data. Correlation studies were also performed for the results obtained, and thus the results were compared [18]. Prajapati and Sahay worked on a survey paper on the solar irradiance forecasting method. They used

different and reliable statistical methods for the estimation of radiation amounts, and the results were explained [19]. Huang et al. used the ARMA model for estimating the solar energy capability. Short-time radiation estimation was made using the MATLAB program and the ARMA statistical model [20].

Ferrari et al. used a statistical model approach for radiation prediction. The climatic data obtained for the town of Milan estimated the amount of radiation within the framework of the numerous statistical models and compared them with each other [21]. Marchesoni-Acland et al. analyzed the performance of the ARMA models. During this study, the quantity of short-term radiation employing a self-repetitive algorithm using satellite data was estimated [22]. Colak et al. carried out ARMA and ARIMA models for determining global solar radiation. The statistical model was constructed comparisons of the ARMA and ARIMA models were made to this model, and radiation amount estimation was made with the best results [23]. Diagne et al. reviewed a global solar radiation prediction model. During this study, they stated that solar energy contains a fluctuating production trend because the amount of radiation changes very rapidly over time, and thus the irradiance amount estimation isn't effective in solar power. Statistical models were used for the quantity of radiation and compared with each other [24]. Alsharif et al. stated that a statistical ARIMA model is utilized for the estimation of solar irradiance. This effort is performed as a case study for Seoul, the Republic of Korea. They used seasonal statistical methods (SARIMA) for the town of Seoul. Connections were established, and comparisons were made employing an information set of roughly 37 years (1981–2017) [25]. Li et al. emphasized that, due to economic and technical restrictions, the daily values of solar radiation were taken into account in most feasibility studies [26]. They improved a graphical solar irridation model by using daily solar irridation values. In this study, they claimed that they got approximately 10% more accuracy than usual methods. Gupta et al. reviewed estimation models of global solar radiation [27]. They emphasized that solar energy is the most important renewable energy for achieving the net zero target by 2050. Hissou et al. examined the machine learning methodology for the prediction of global solar irradiation [28]. They emphasized that the results of the results of this new approach were satiably in accordance with regression models. Guermoui et al. harmonized methodologies like time-varying filters and empirical approach [29]. They stated that the results of this new approach are better than those of classical estimation methods for all studied regions. Fan et al. analyzed empirical and machine learning methodologies for estimating solar irradiation in the various states of China [30]. 12 machine learning models were used in the study. ANFIS, MARS, and XGBoost models were indicated as the most recommended machine learning models. Gürel et al. reviewed various methods for the prediction of solar irradiation [31]. They compared empirical, time-series, artificial intelligence, and hybrid models. They emphasized that each model has advantages and disadvantages in accordance with the targeted zone. They claimed that the hybrid model is a more applicable approach for the prediction of global solar radiation. Yarar et al. emphasized the importance of hourly-based global solar radiation for harmonic analysis of the microgrid connection [32]. Kaysal and Hocaoğlu modelled a new approach using an artificial neural network for the prediction of solar irradiation [33]. They used a two-stage forecasting model and a discrete wavelet transform for their

study. Mukhtar et al. integrated conventional and artificial neural networks for the prediction of hourly-based solar irradiation [34]. They emphasized that, in general, developing countries do not have solar pironometers. So, they claimed that the designated method can be used in developing countries, especially African countries. Geetha et al. offered an artificial neural network model for the prediction of global solar radiation [35]. They claimed that, due to this improved model, designing and evaluating the stage of PV installation can be easier without meteorological data collection. In these studies, researchers claimed that hourly solar irradiance data are important for evaluating power plants that are using photovoltaic tools and equipment. They emphasized that the majority of solar irradiance studies and actual measurements are not obtained by daily values due to economic and technical restrictions, especially in developing countries. In their study, they used the identification, classification, clustering, and regression of climate indicators and meteorological data. They compared estimation models and tried to get the best availability.

In the studies conducted by researchers, it was mentioned that more effective results are obtained by using empirical and hybrid methods. In conducting the study, econometric models and empirical modeling approaches were used. As a result of these studies, it was found that empirical models are more useful. Comparing the studies conducted by the researchers, it is found that similar results were obtained, and it is evaluated that the researchers have developed models that contain complex calculations and relationships. The main objective of this study is to provide data for the algorithm to optimize the installed power and energy management of hybrid power plants. The developed algorithm determines the size of the hybrid structure with renewable energy pairs. This algorithm structure consists of four main sections. In the first section, the project characteristics of the renewable energy to be used in the hybrid structure are determined; in the second part, the project characteristics of solar energy; in the third part, the costs; and in the fourth part, the decision mechanism, including the iterative functions, is included. The study carried out aimed to use solar radiation on an hourly basis, which is intended as a data input for the calculation of the amount of energy to be extracted from the solar energy sector. It is expected that the hourly solar radiation is practical and flexible so that it can be used in the algorithm. To meet the requirements of the algorithm, it was preferred to compare models based only on empirical and econometric approaches rather than the complex and mixed structures developed by other researchers. As a result of the comparison, it was found that it is more appropriate to use empirical models because they have high coefficients and can meet the requirements of the algorithm. It has been found that the amount of solar radiation that provides the data input for the developed algorithm can be improved with hybrid or more advanced models. It is assumed that these integrated, developed structures can be used, but in terms of practicality, the use of empirical models is considered sufficient. The designed algorithm is given in **Figure 1**.

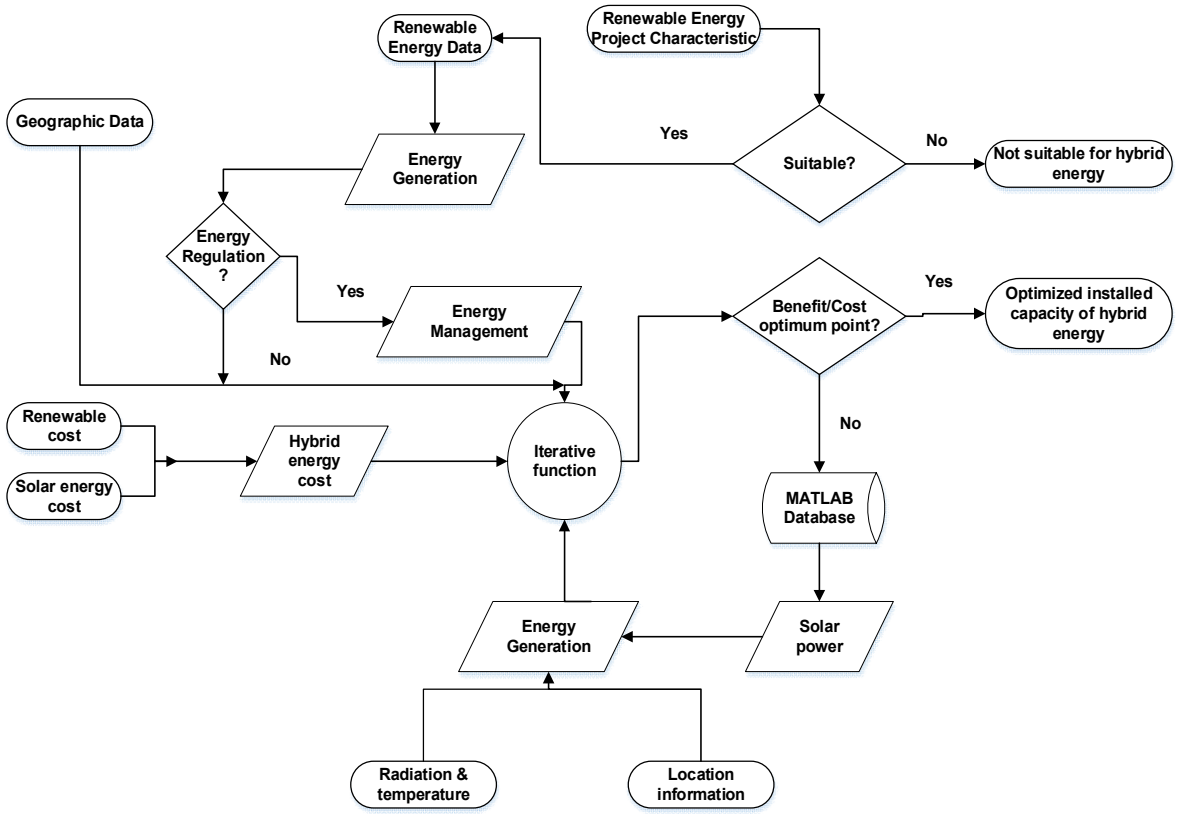

Figure 1. The algorithm of installed capacity for solar energy in integrated hybrid renewable structure.

Thanks to the developed algorithm, the installed capacity of solar energy to be engaged in hybrid energy systems is determined and optimized. The algorithm has a simple but effective decision mechanism and basically works considering the generation profiles and characteristics of the energy management of renewable energy plants in the hybrid structure. In this study, the amount of solar radiation data was estimated to feed into the algorithm and determine the amount of solar energy production. Since energy management is done on an hourly basis, the predictions aim to determine the amount of solar radiation on an hourly basis.

2. Mathematical model

The ratio of the amount of solar energy on an empirical hourly basis to the amount of solar energy daily is calculated by Equation (1) given below.

$$\frac{G_h}{G_d} = \frac{\left(\frac{\pi}{24}\right).(\cos w - \cos w_s)}{\sin w_s - (\frac{2\pi w_s}{360}).(\cos w_s)} \quad (1)$$

In Equation (1), G_h represents the hourly-based solar irradiance (kWh/m^2), G_d represents the daily-based solar irradiance (kWh/m^2), w_s represents the hour angle at sunrise (° degrees). w represents the hour angle (° degrees) which the displacement of the sun concerning a defined zone of the world and can be found by Equation (2) below.

$$w = \left(\frac{360}{24}\right).(AST - 12) \quad (2)$$

The AST (apparent solar time) specified in Equation (2) represents the observed or actual solar time. AST is calculated by Equation (3) given below;

$$AST = LST + EoT + \left(4\frac{\text{minute}}{\text{degree}}\right)[(LSMT - LOD)] \quad (3)$$

LST (local standard time) specified in Equation (3) represents the time of local standard, LOD represents the longitude, $LSMT$ (local standard meridian time) represents the meridian time of local standard, and EoT (equation of time) represents the imbalance of visible and mean solar time. $LSMT$ and EoT are found by Equations (4) and (5) given below.

$$LSMT = 15°.(Zone\ of\ GMT) \quad (4)$$

$$EoT = 9.87.\sin(2B) - 7.53.\cos(B) - 1.5.\sin(B) \quad (5)$$

The *GMT* (Greenwich Mean Time Zone) specified in Equation (4) represents the time intervals arranged according to the city of Greenwich. B is a coefficient and is found as stated in Equation (6) below;

$$B = \frac{360°}{365}.(n - 81) \quad (6)$$

The n specified in Equation (6) represents the number corresponding to the day in the calendar year. For example, while the number of n for January 1 is 1, the number n for February 1 is 32.

w_s specified in Equation (1) is found by Equation (7);

$$w_s = \cos^{-1}(-\tan\emptyset\tan\delta) \quad (7)$$

The w_s specified in Equation (7) represents the sunrise angle. In this equation $\emptyset$ represents the angle of latitude (°C), and δ represents the slope (°C). δ is calculated by Equation (8) given below.

$$\delta = 23.45.\sin\left[\frac{360(284 + n)}{365}\right] \quad (8)$$

The angle δ varies between +23.45°/−23.45°. The following **Figure 2** shows the change in the angle during the year;

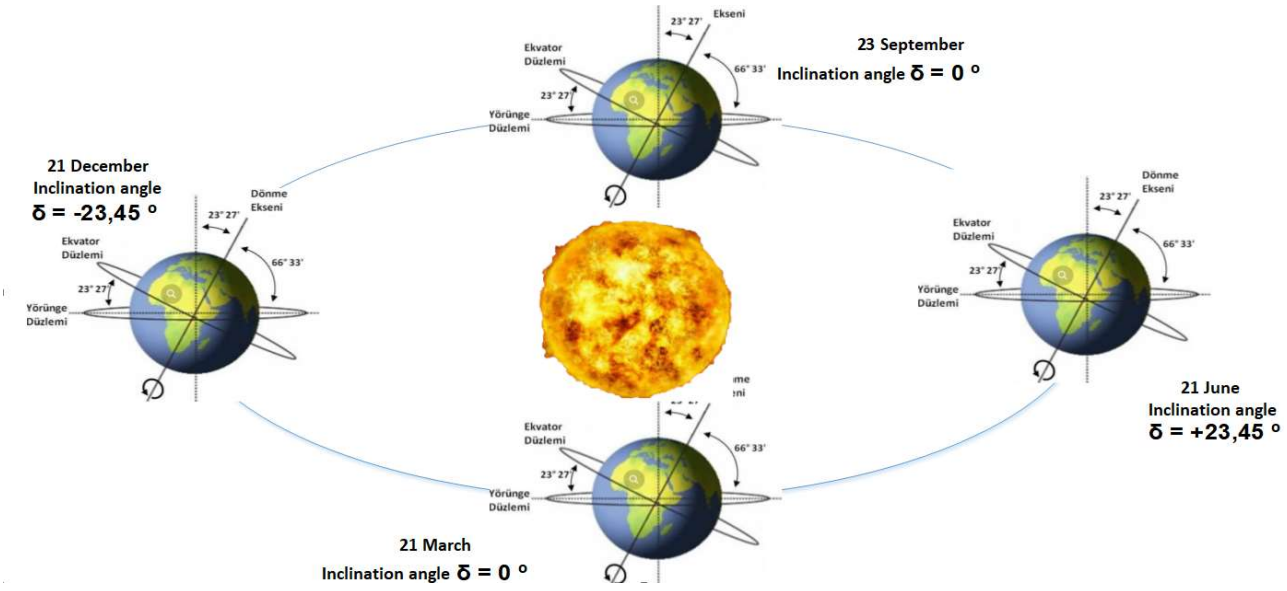

Figure 2. Angle of inclination and change over the year [6].

In the study carried out by Chandel and Aggarwal [7] the relationship between daily and hourly solar radiation is given in Equation (9) below;

$$r_t = \frac{G_h}{G_d} \tag{9}$$

The r_t term specified in Equation (9) represents the conversion rate between hourly and daily solar radiation. The r_t ratio is obtained by Equation (10) given below;

$$r_t = \frac{r_o.\left[1 + q.\left(\frac{a_2}{a_1}\right).k.A(w_s).r_0\right]}{\left[1 + q.\left(\frac{a_2}{a_1}\right).B(w_s)/A(w_s)\right]} \tag{10}$$

The r_o given in Equation (10) represents the ratio of the earth outside hourly based solar irradiance to the daily irradiance. This ratio is calculated by Equation (11) given below. The coefficients, k, $A(w_s)$ and $B(w_s)$ are given in Equations (12)–(14).

$$r_o = (\cos w - \cos w_s)/k.A(w_s) \tag{11}$$

$$k = \frac{24}{\pi} \tag{12}$$

$$A(w_s) = \sin w_s - w_s.cosw_s \tag{13}$$

$$B(w_s) = w_s.(0.5 + \cos^2 w_s) - 0.75\,.\sin 2w_s \tag{14}$$

The coefficients, a_2 and a_1 specified in Equation (10) are empirical coefficients. These coefficients are calculated by Equation (15) below;

$$\begin{aligned} a_1 &= 0.41341.K_t + 0.61197.{K_t}^2 - 0.01886.K_t.S_0 + 0.00759.S_0 \\ a_2 &= \text{Max}(0.054; 0.28116 + 2.2475.K_t - 1.76118.{K_t}^2 - 1.84535\sin h_0 \\ &\quad + 1.6811.\sin^3 h_0 \end{aligned} \tag{15}$$

K_t in Equation (15) represents the measured radiation ratio of earth's face to the calculated irradiance at the highest point of the atmosphere. In this study, ratio is accepted as 0.61 [10].

Given in Equation (10), q is the incidence angle of the beam, h_0 is the sun height of the atmosphere, S_0 is the daytime duration. The corresponding Equations (16)–(18) are given below to calculate the relevant parameters;

$$q = \cos\emptyset.\cos\delta \tag{16}$$

$$\sin h_0 = \frac{q.A(w_s)}{w_s} \tag{17}$$

$$S_0 = k.w_s \tag{18}$$

In addition to empirical methods, the amount of solar radiation can be determined by using econometric statistical methods. If hourly data is available for the studied site, hourly solar radiation data can be obtained, which is likely to occur prospectively. The most commonly used models in the literature and their explanations are given below. Time series lead to statistical data. These models, which are especially used for the sun and wind, produce new predictions in line with the actual data. One of the most used models is the self-connection (AR-autoregressive) model. The AR model is calculated as given in Equation (19);

$$x_t = \sum_{i=1}^{m} \phi_i.x_{t-i} + w_t = \phi_1.x_{t-1} + \phi_2.x_{t-2} + \cdots + \phi_m.x_{t-m} + w_t \tag{19}$$

In Equation (19), x_t represents time series value, w_t represents noise amounts, $\phi = (\phi_1, \phi_2, \ldots, \phi_m)$ vectors of model coefficients, m represents positive integer.

Another model is the moving average (MA-moving average) model. In this model, unlike the AR model, time series are created by using weighted total values in this model. The MA model is calculated as given in Equation (20);

$$x_t = \sum_{j=0}^{n} \theta_j . w_{t-j} = w_t + \theta_1 . x_{t-1} + \theta_2 . x_{t-2} + \cdots + \theta_n . x_{t-n} \quad (20)$$

Equation (20), x_t represents the time series value, w_t represents the noise amounts, $\theta = (\theta_1, \theta_2, \ldots, \theta_n)$ is the vector coefficients of the model, n represents the positive integer. θ_0 is accepted as $\theta_0 = 1$.

Another model is the self-correlated moving average (ARMA) model. This model has emerged by using AR and MA models together. It is calculated by Equation (21) given below.

$$x_t = \sum_{i=1}^{m} \phi_i . x_{t-i} + \sum_{j=0}^{n} \theta_j . w_{t-j} \quad (21)$$

In Equation (21), x_t is time series value, w_t is the amount of noise, $\theta = (\theta_1, \theta_2, \ldots, \theta_n)$ is the vector of moving average model coefficients, $\phi = (\phi_1, \phi_2, \ldots, \phi_m)$ is the vector of self-correlated model coefficients, m and n represent a positive integer. θ_0 is accepted as $\theta_0 = 1$.

Another model is the self-related and external variable moving average (ARMAX). This model has emerged by using AR and MA models together, as well as expanding the overall scope by using variables. It is calculated by Equation (22) given below.

$$x_t = \sum_{i=1}^{m} \phi_i . x_{t-i} + \sum_{j=0}^{n} \theta_j . w_{t-j} + \sum_{k=1}^{p} \lambda_k . e_{t-k} \quad (22)$$

In Equation (22), x_t is time series value, w_t is noise amount, $\theta = (\theta_1, \theta_2, \ldots, \theta_n)$ is the vector of moving average model coefficients, $\phi = (\phi_1, \phi_2, \ldots, \phi_m)$ is the vector of the self-correlated model coefficients, $\lambda = (\lambda_1, \lambda_2, \ldots, \lambda_p)$ is the external variable coefficient, m, n and p represent a positive integer. θ_0 is accepted as $\theta_0 = 1$.

Another model is the self-correlated and integrated moving average (ARIMA) model. This model is achieved by using AR and MA models together, as well as evaluating non-stationary variables. It is calculated by Equation (23) given below.

$$x_t = \sum_{i=1}^{m} \phi_i . S^d . x_{t-i} + \sum_{j=0}^{n} \theta_j . w_{t-j} \quad (23)$$

In Equation (23), x_t is the time series value, w_t is the amount of noise, $\theta = (\theta_1, \theta_2, \ldots, \theta_n)$ is the vectors of moving average model coefficients, $\phi = (\phi_1, \phi_2, \ldots, \phi_m)$ is the vectors of self-correlated model coefficients, m and n represent a positive integer. θ_0 is accepted as $\theta_0 = 1$. The expressions $S = 1 - q - 1$ and $\phi_m(q)$, represent the stationarity and translatability expressions of the AR (m) operator.

3. A case study

The second method employed in obtaining the quantity of radiation is the approach that features econometric and statistical methods. The most widely used econometric models within the literature are autoregressive integrated moving average (ARIMA), autoregressive moving average (ARMA), autoregressive moving average model with exogenous variables (ARMAX), autoregressive (AR), and moving average (MA) models. Additionally, an artificial neural network (ANN) model was used as a synthetic intelligence element. Econometric models were created using the

"R" modeling program and MATLAB. The models used were compared with one another, and therefore the best-suited one was chosen. In the first place, a one-day forecast was made for the AR and MA models, which are econometric models. Econometric models are fed from the data set from a solar energy plant that is found in Denizli province, Acıpayam district of Turkey. A seven-day real data set was used to predict one-day radiation. The MATLAB program is employed for this prediction. The demonstration of the model is given in **Figure 3**.

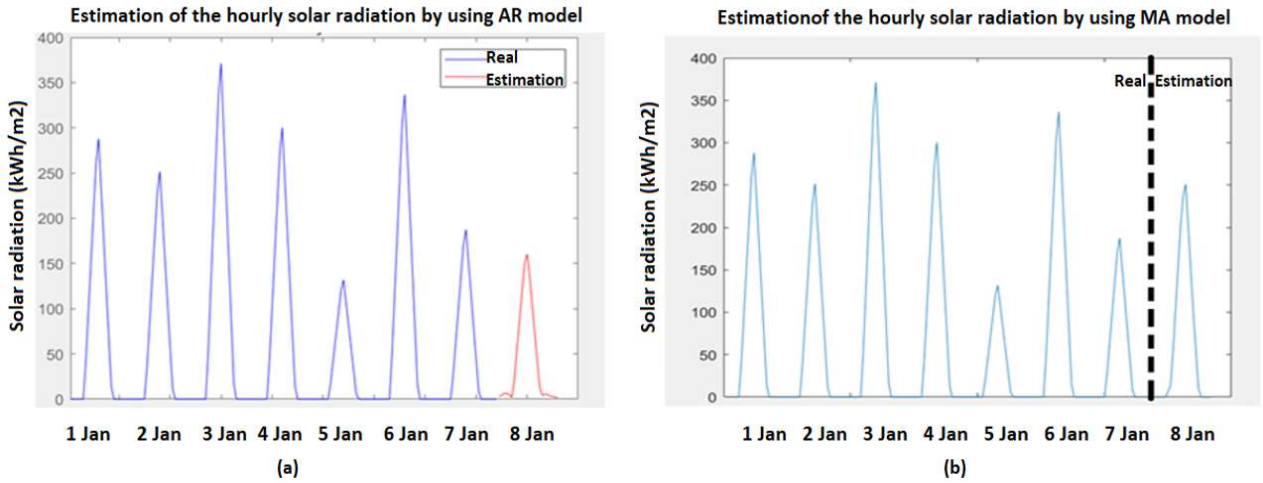

Figure 3. Estimation of the hourly solar radiation by **(a)** AR model; and **(b)** MA model.

The study was distributed with the "R" modeling program for ARIMA and ANN models. Six days of information acquisition are employed for 1 day and 6 days following estimations. The study results and existing condition comparisons are demonstrated within the graphs below. The details of the study are given in **Figures 4** and **5**.

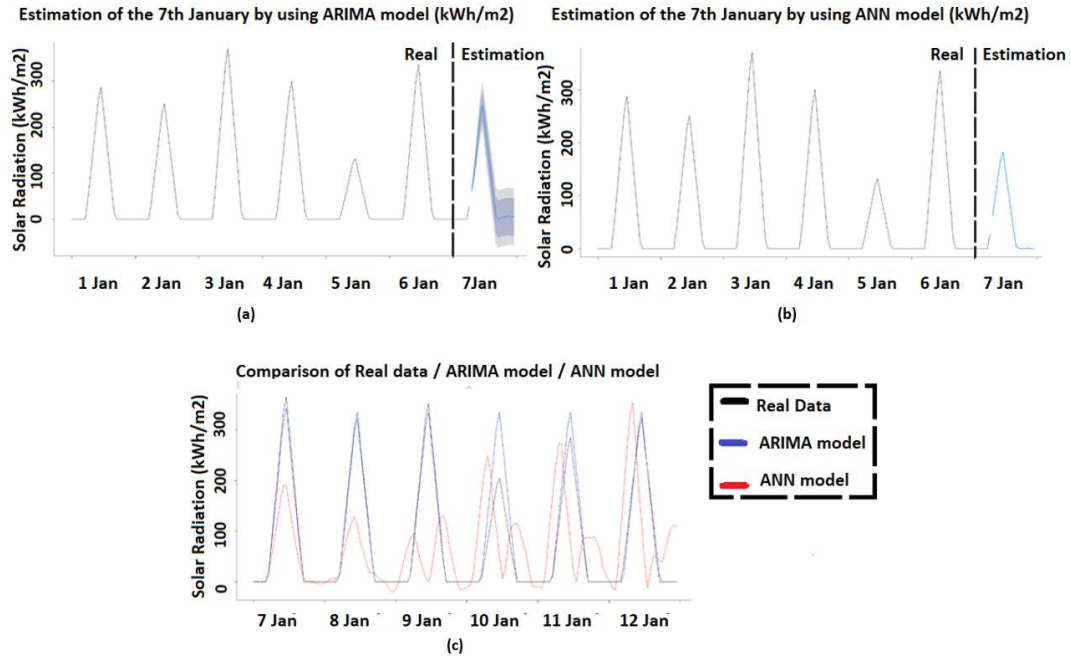

Figure 4. Models comparison **(a)** ARIMA model; **(b)** ANN model; **(c)** ARIMA/ANN models.

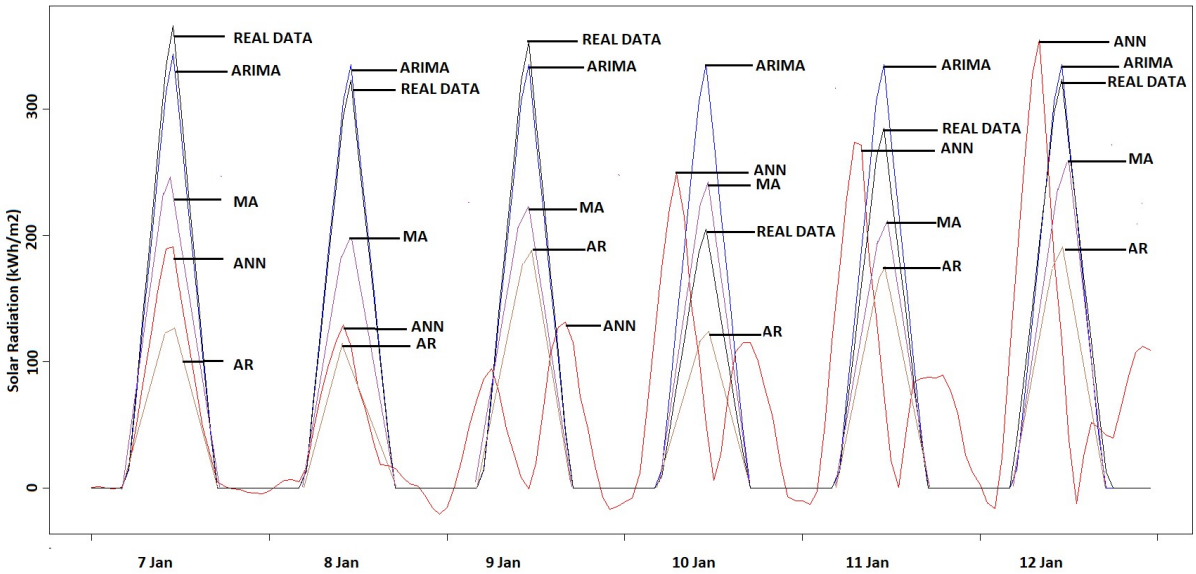

Figure 5. Comparison of the econometric models.

Looking at the comparative figure, it is clear that the econometric models differ from the actual data. Taken on its own, it can be said that the ARIMA model produces results that are relatively similar to the original data. Although the ARIMA model consists of the integration of other AR and MA models, it is a more advanced econometric model. Finally, using the data within the first 2 months of the year—January and February—radiation amount predictions were made for the primary six days of March. The subsequent chart shows the relevant studies and their results. Estimates obtained with AR and MA models produced very different results from the particular data. Within the more advanced ARIMA and ANN models, estimations were made using only a two-day data set. Additionally, "R" modeling, which is an econometric program that has more precise results for these models, was used. First, the ARIMA model was run. The quantity of estimation that offers the foremost optimum solution in step with the determined number of steps has been revealed. The blue drawing within the graph below gives the optimum ARIMA line. Other gray areas reflect the framework of others and sensibility (**Figure 6**).

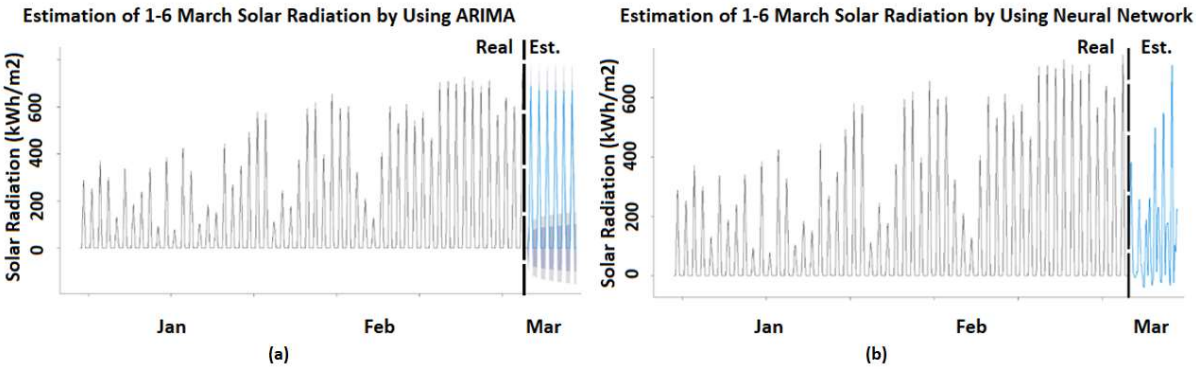

Figure 6. Prediction of the solar radiation of 1–6 March by using **(a)** ARIMA; and **(b)** ANN.

Using econometric models can provide reasonable results if the information is as detailed and long as possible. It's not always easy to achieve these detailed, supported

coordinates in radiation estimations. An empirical model comes into play in these circumstances. The daily radiation amounts are often reached at supported coordinates on the official NASA website. When the empirical model compares with the artificial neural network and ARIMA models,

- It doesn't need one-to-one hourly radiation. It is often obtained on an hourly basis using daily radiation.
- While the amount of radiation at any point in the world is obtained daily from public sources, it's too difficult to access hourly radiation amount data supported by coordinates.
- High correlation with real values.
- Does not need long-term data entry like ARIMA and ANN.
- Obtaining realistic predictions not only in short-term forecasts like ARIMA and ANN but also in long-term forecasts.

Due to its prominent features, it's been decided to use an empirical model for radiation predictions. Based on the results obtained, using the MATLAB GUI program, an interface has been created to display the quantity of radiation within the day, month, year, or any desired period. Changes in the amount of radiation throughout the year and the start and end times are often determined within the interface and may be obtained at desired month, day, and hour intervals.

So, an empirical model is chosen for hourly-based estimation. The radiation amounts of the coordinates of the solar energy plant located in Denizli province, Acıpayam district, which are used for empirical models, were obtained daily from the NASA website [36]. By making use of the equations described within the mathematical model section, hourly radiation amounts were obtained in daily radiation amounts. Additionally, the study was enriched with the MATLAB GUI program. By using the MATLAB GUI, it's possible to draw graphs of the quantity of radiation on an hourly basis at any time during the year. While designing the MATLAB GUI graphic area, radiation amounts were graphed in line with the beginning and end times. The timeline relies on months, days, and hours. Desired graphs are drawn by entering the periods to be seen in these boxes. An 8760-hour-based radiation dataset was created to hide the entire year. The MATLAB GUI chart below shows the 24 h radiation amounts for 31 March, 30 June, 30 September, and 31 December. This demonstration is given in **Figure 7**.

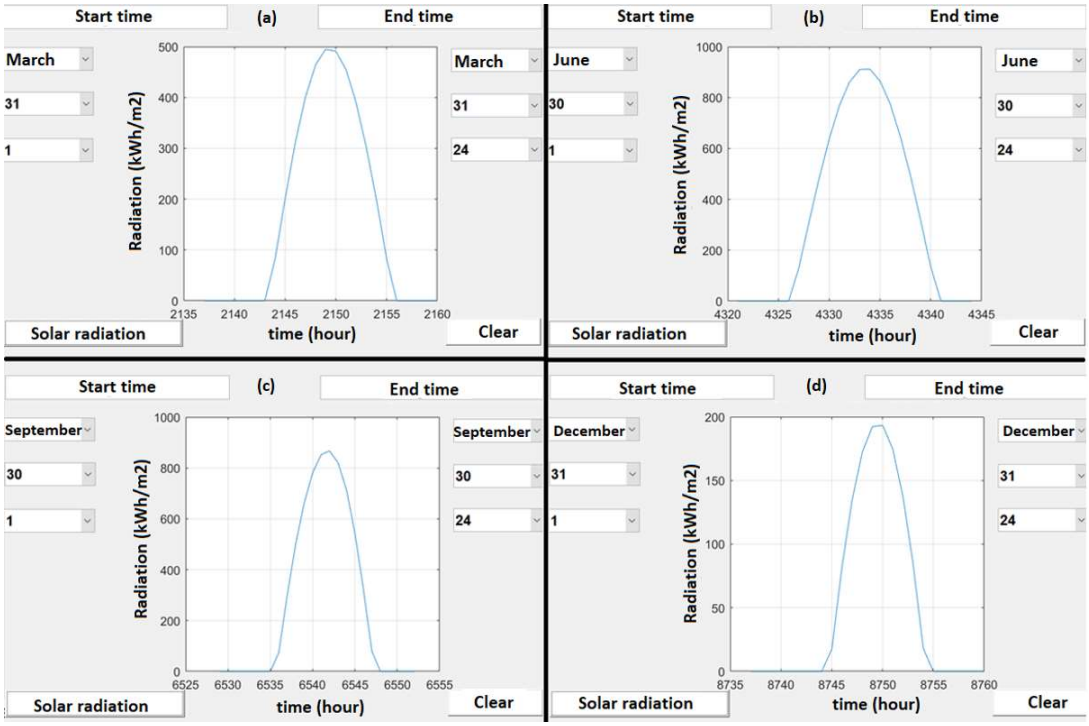

Figure 7. Estimation of the hourly based solar radiation by using the empirical model in MATLAB GUI **(a)** 31 March; **(b)** 30 June; **(c)** 30 September; and **(d)** 31 December.

The daily radiation amounts were taken from the NASA website for the solar energy plant located within the Acıpayam district of Denizli province. This original dataset is given in **Figure 8**.

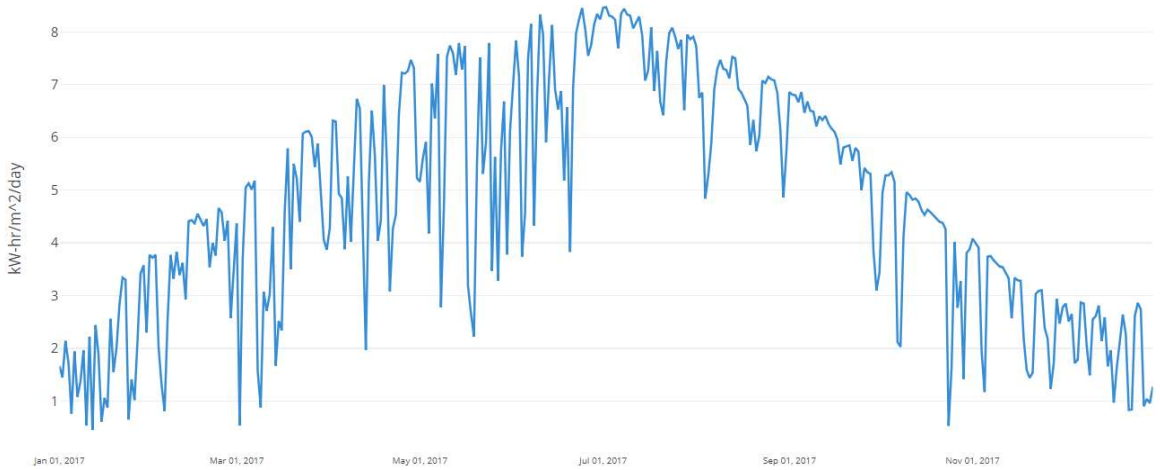

Figure 8. The daily solar radiation obtained from the NASA website (365 days) [26].

The amount of solar energy produced may be calculated by using the panel data. To check the operation of the approach, a dataset of a SPP that is located at a distance of 2 km was taken. Daily NASA data for the identical region were correlated hourly within the light of the original data using the equations above. The parametric statistic obtained as a result of 86% gives a robust concept whose acceptance is usable for solar radiation. The daily NASA data are converted to the hourly irradiance shown in the figure below. The correlation graph of the study is given in **Figure 9**.

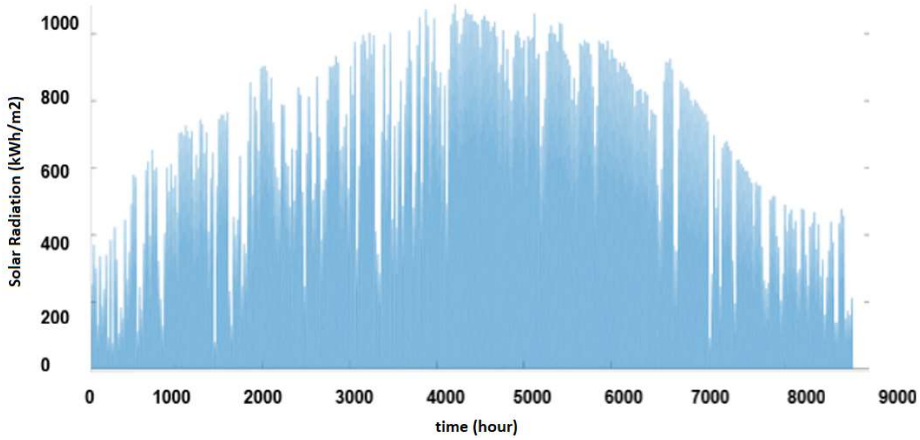

Figure 9. The hourly based solar irradiance obtained from the daily solar irradiance dataset (8760 h = 24 h/day × 365 day).

The energy generation amount was estimated by using the empirically obtained radiation amount and panel/inverter data of a solar energy plant located within the Acıpayam district of Denizli province. The particular production of this existing facility has been compared with the energy generation amounts prepared using the radiation amounts obtained on an hourly basis. *X* variable references the time, *Y* is that the radiation. The coefficient of correlation is obtained as 0.8625. The result is given in **Figure 10.**

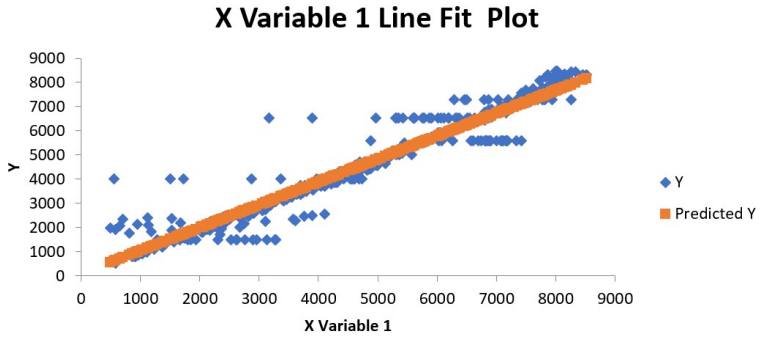

Figure 10. Predicted and real solar radiation correlation plot.

With the assistance of the designed interface, analyses may be made for specified periods, and changes in radiation amounts may be observed. After determining the quantity of radiation, the quantity of energy to be obtained from the sun was determined. After obtaining the amount of radiation, the amount of energy that will be obtained from the sun was calculated following the mathematical model and algorithm explained within the above sections. Before calculating the quantity of radiation, the energy production figures of an SPP facility located in Denizli province/Acpayam district were compared with the energy amount obtained by the proposed method, and the technical specifications of the panels utilized in the prevailing SPP facility were taken as a basis. Within the current SPP facility, Yingli Solar-branded 250-watt polycrystalline PV panels are used. Within the manuals (data sheet) containing the technical specifications of the PV panels, the measurement results under the quality test (STC-standard test condition) and nominal operating cell (NOCT) conditions are included.

The amount of power that can be obtained from PV panels depends on radiation and temperature. The graph below shows the I-V and power curves of the PV panels embedded in MATLAB. Technical specifications also include changes in current and voltage due to a natural process. After entering the NOCT values of the chosen PV panel, the values to be obtained and the voltage were determined by using the hourly data obtained from the meteorology station for Acıpayam district. The quantity of energy that may be obtained from the solar power system was calculated by multiplying the determined current and voltage values with one another. Since a high production forecast of roughly 91% can be obtained in comparison to the particular electricity generation. It's been accepted that the said approach is employed in other regions similarly. Accordingly, the calculation was made by using the tactic described above within the determination of the number of radiations in the related HEPP facility area.

4. Conclusion

The summarized results of this study are given below.

In recent years, worldwide applications and research have been disbursed for SHE plants, which is one of the hybrid renewable energy systems. One of the foremost issues for these integrated facilities is the management of the amount of energy generated from solar and hydroelectricity. To confirm reliable energy management, hourly electricity generation must be obtained. Electricity generation from solar energy may be a function that depends on the quantity of radiation and temperature. To see the amount of solar energy on an hourly basis, the amount of radiation must be determined. While it's easy to access the daily radiation data on a coordinated basis, this data isn't disclosed to the public on an hourly basis.

There are two basic methods employed in the literature to get the quantity of radiation on an hourly basis. One of them is the empirical method, and the other is the econometric method. In this study, the quantity of radiation was determined by using both methods. As a result of the studies, the quantity of radiation on an hourly basis was obtained from the daily radiation data, while more realistic results were obtained with the empirical method. The biggest difference during this comparison is the requirement of longer-term and more detailed data for econometric statistical models to get an affordable result. By using the empirical model, the quantity of radiation on an hourly basis was obtained from the daily radiation. These data are often easily employed in the energy management of renewable hybrid energy systems like solar hydroelectric facilities. The suggested hourly-based global solar radiation, which is obtained by an empirical model, can be used in the developed algorithm of a hybrid renewable energy system. It is a simple and practical way to estimate the amount of solar energy. The existing results are adequate; in addition to this, the study can be improved by using advanced artificial intelligence methods.

Conflict of interest: The author declares no conflict of interest.

References

1. Tırmıkçı CA. Real-time Comparison of a Two-Axis Sun-Tracking Moving Solar System and a Fixed Solar System Positioned at an Optimal Annual Inclination Angle (Turkish) [PhD thesis]. Sakarya Üniversitesi; 2018. pp. 1-110.
2. Jacovides CP, Tymvios FS, Assimakopoulos VD, et al. Comparative study of various correlations in estimating hourly diffuse fraction of global solar radiation. Renewable Energy. 2006, 31(15): 2492-2504. doi: 10.1016/j.renene.2005.11.009
3. Iqbal M. Correlation of average diffuse and beam radiation with hours of bright sunshine. Solar Energy. 1979, 23(2): 169-173. doi: 10.1016/0038-092x(79)90118-x
4. Alsafadi M, Başaran Filik Ü. Hourly global solar radiation estimation based on machine learning methods In Eskisehir. Eskişehir Technical University Journal of Science and Technology A—Applied Sciences and Engineering. 2020, 21(2): 294-313. doi: 10.18038/estubtda.650497
5. Serttaş F. A New Approach to Solar Irradiance Forecasting Based on Pattern Scanning (Turkish) [Master's thesis]. Afyon Kocatepe Üniversitesi; 2015. pp. 1-67.
6. Maleki MS, Hizam H, Gomes C. Estimation of hourly, daily and monthly global solar radiation on inclined surfaces: Models re-visited. Energies. 2017, 10(1): 134. doi: 10.3390/en10010134
7. Chandel SS, Aggarwal RK. Estimation of hourly solar radiation on horizontal and inclined surfaces in western Himalayas. Smart Grid and Renewable Energy. 2011, 2(1): 45-55. doi: 10.4236/sgre.2011.21006
8. Khatib T, Elmenreich W. A model for hourly solar radiation data generation from daily solar radiation data using a generalized regression artificial neural network. International Journal of Photoenergy. 2015, 2015: 1-13. doi: 10.1155/2015/968024
9. Berrizbeitia SE, Jadraque Gago E, Muneer T. Empirical models for the estimation of solar sky-diffuse radiation. A review and experimental analysis. Energies. 2020, 13(3): 701. doi: 10.3390/en13030701
10. Gueymard C. Prediction and performance assessment of mean hourly global radiation. Solar Energy. 2000, 68(3): 285-303. doi: 10.1016/s0038-092x(99)00070-5
11. Al-Rawahi NZ, Zurigat YH, Al-Azri NA. Prediction of hourly solar radiation on horizontal and inclined surfaces for Muscat/Oman. The Journal of Engineering Research [TJER]. 2011, 8(2): 19. doi: 10.24200/tjer.vol8iss2pp19-31
12. Ishola KA, Fealy R, Mills G, et al. Developing regional calibration coefficients for estimation of hourly global solar radiation in Ireland. International Journal of Sustainable Energy. 2018, pp.1-15.
13. Hussein TAT. Estimation of hourly global solar radiation in egypt using mathematical model. International Journal Latest Trends Agriculture Food Science. 2012, 2(2): 74-82.
14. Huang J, Korolkiewicz M, Agrawal M, et al. Forecasting solar radiation on an hourly time scale using a coupled autoregressive and dynamical system (CARDS) model. Solar Energy. 2013, 87: 136-149. doi: 10.1016/j.solener.2012.10.012
15. Mbaye A, Ndiaye ML, Ndione DM, et al. ARMA model for short-term forecasting of solar potential: Application to a horizontal surface of Dakar site. OAJ Materials and Devices. 2019, 4(1). doi: 10.23647/ca.md20191103
16. Adejumo AO, Suleiman EA. Application of ARMA-GARCH models on solar radiation for South Southern Region of Nigeria. Journal of Informatics and Mathematical Science. 2017, 9(2): 405-416.
17. Ghofrani M, Alolayan M. Time series and renewable energy forecasting. Time Series Analysis and Application. 2018, 77-92. doi: 10.5772/intechopen.70845
18. Hejase HAN, Assi AH. Time-series regression model for prediction of mean daily global solar radiation in Al-Ain, UAE. ISRN Renewable Energy. 2012, 2012: 1-11. doi: 10.5402/2012/412471
19. Prajapati SK, Sahay KB. A survey paper on solar irradiance forecasting method. International Journal of Engineering Research & Technology (IJERT). 2016, 5(3): 536-541. doi: 10.17577/ijertv5is030469
20. Huang R, Huang T, Gad R. Solar generation prediction using the ARMA model in a laboratory-level micro-grid. In: Proceedings of the 2012 IEEE Third International Conference on Smart Grid Communications (SmartGridComm); 5-8 November 2012; Tainan, Taiwan. pp. 1-6. doi: 10.1109/SmartGridComm.2012.6486039
21. Ferrari S, Lazzaroni M, Piuri V, et al. Statistical models approach for solar radiation prediction. In: Proceedings of the 2013 IEEE International Instrumentation and Measurement Technology Conference (I2MTC); 6-9 May 2013; Minneapolis, MN, USA. pp. 1-6. doi: 10.1109/I2MTC.2013.6555712

22. Marchesoni-Acland F, Lauret P, Gomez A, et al. Analysis of ARMA solar forecasting models using ground measurements and satellite image. In: Proceedings of the 2019 IEEE 46th Photovoltaic Specialists Conference (PVSC), 16-21 June 2019; Chicago, USA. pp. 1-7. doi: 10.1109/PVSC40753.2019.8980821
23. Colak I, Yesilbudak M, Genc N, et al. Multi-period prediction of solar radiation using ARMA and ARIMA models. In: Proceedings of the 2015 IEEE 14th International Conference on Machine Learning and Applications, 9-11 December 2015, Miami, Florida, USA. pp. 1045-1049. doi: 10.1109/ICMLA.2015.33
24. Diagne M, David M, Lauret P, et al. Review of solar irradiance forecasting methods and a proposition for small-scale insular grids. Renewable and Sustainable Energy Reviews. 2013, 27: 65-76. doi: 10.1016/j.rser.2013.06.042
25. Alsharif M, Younes M, Kim J. Time series ARIMA model for prediction of daily and monthly average global solar radiation: The case study of Seoul, South Korea. Symmetry. 2019, 11(2): 240. doi: 10.3390/sym11020240
26. Li Y, Wang Y, Yao W, et al. Graphical decomposition model to estimate hourly global solar radiation considering weather stochasticity. Energy Conversion and Management. 2023, 286: 116719. doi: 10.1016/j.enconman.2023.116719
27. Gupta S, Singh AK, Mishra S, et al. Estimation of solar radiation with consideration of terrestrial losses at a selected location—A review. Sustainability. 2023, 15(13): 9962. doi: 10.3390/su15139962
28. Hissou H, Benkirane S, Guezzaz A, et al. A novel machine learning approach for solar radiation estimation. Sustainability. 2023, 15(13): 10609. doi: 10.3390/su151310609
29. Guermoui M, Gairaa K, Ferkous K, et al. Potential assessment of the TVF-EMD algorithm in forecasting hourly global solar radiation: Review and case studies. Journal of Cleaner Production. 2023, 385: 135680. doi: 10.1016/j.jclepro.2022.135680
30. Fan J, Wu L, Zhang F, et al. Empirical and machine learning models for predicting daily global solar radiation from sunshine duration: A review and case study in China. Renewable and Sustainable Energy Reviews. 2019, 100: 186-212. doi: 10.1016/j.rser.2018.10.018
31. Gürel AE, Ağbulut Ü, Bakır H, et al. A state of art review on estimation of solar radiation with various models. Heliyon. 2023, 9(2): e13167. doi: 10.1016/j.heliyon.2023.e13167
32. Yarar N, Yagci M, Bahceci S, et al. Artificial neural networks based harmonics estimation for real university microgrids using hourly solar irradiation and temperature data. Energy Nexus. 2023, 9: 100172. doi: 10.1016/j.nexus.2023.100172
33. Kaysal K, Hocaoğlu FO. Modelling of different mother wavelet transforms with artificial neural networks for estimation of solar radiation. Eskişehir Technical University Journal of Science and Technology A—Applied Sciences and Engineering. 2023, 24(2): 141-154. doi: 10.18038/estubtda.1184918
34. Mukhtar M, Oluwasanmi A, Yimen N, et al. Development and comparison of two novel hybrid neural network models for hourly solar radiation prediction. Applied Sciences. 2022, 12(3): 1435. doi: 10.3390/app12031435
35. Geetha A, Santhakumar J, Sundaram KM, et al. Prediction of hourly solar radiation in Tamil Nadu using ANN model with different learning algorithms. Energy Reports. 2022, 8: 664-671. doi: 10.1016/j.egyr.2021.11.190
36. NASA Prediction of Worldwide Energy Resources. The power project. Available online: https://power.larc.nasa.gov/ (accessed on 22 November 2023).

Energy Storage and Conversion 2024, 2(1), 457.
https://doi.org/10.59400/esc.v2i1.457

Review

Review on green resources and AI for biogenic solar power

Jyoti Bhattacharjee, Subhasis Roy*

Department of Chemical Engineering, University of Calcutta, Kolkata 700009, India
*** Corresponding author:** Subhasis Roy, subhasis1093@gmail.com; srchemengg@caluniv.ac.in

CITATION

Bhattacharjee J, Roy S. Review on green resources and AI for biogenic solar power. Energy Storage and Conversion. 2024; 2(1): 457. https://doi.org/10.59400/esc.v2i1.457

ARTICLE INFO

Received: 5 January 2024
Accepted: 16 February 2024
Available online: 25 February 2024

COPYRIGHT

Copyright © 2024 by author(s). *Energy Storage and Conversion* is published by Academic Publishing Pte. Ltd. This work is licensed under the Creative Commons Attribution (CC BY) license. https://creativecommons.org/licenses/by/4.0/

Abstract: The need for clean and renewable energy has grown dramatically over the past few years. As potential candidates for producing green energy in this region, photovoltaic and bio-solar energy technologies have arisen. This review presents a novel approach for designing and developing photovoltaics and bio-solar cells using eco-friendly materials and artificial intelligence (AI) techniques. An intriguing architecture is outlined for a bio-solar cell that fuses photovoltaic electronics with photosynthetic organisms. A recyclable thin-film solar cell serves as the basis of our photovoltaic system. To further maximize the effectiveness of the device, we use AI algorithms. According to statistical calculations, the proposed bio-solar cell can produce a sizable amount of electricity while being ecologically sound. This paper outlines significant advances in developing solar cells and photovoltaics using green nanomaterials and AI, which provide exciting potential for improving energy harvesting capacity. This review also presents an overview of the effects of the potential commercialization of our strategy, its social and environmental benefits, and its pitfalls.

Keywords: bio-solar cell; energy efficiency; green nanomaterials; machine learning; photovoltaics; sustainability

1. Introduction

1.1. History

Humans are becoming more aware of the environmental challenges caused by global warming. This rising awareness is prompting academics to look for new ways to control thermal energy. Recent environmental laws, such as the European Union's objective of reducing greenhouse gas emissions by 40% by 2030 compared to 1990, have posed ambitious challenges to researchers. To achieve this purpose, buildings must regulate their thermal energy efficiently. To put things in perspective, households in the EU created more than 600 million tonnes of CO_2-equivalent greenhouse gases in 2017, more than industry and agriculture combined, which produced roughly 400 million tonnes [1]. Since 1750, the world has seen significant advancements in human civilization, but these have also contributed to the deterioration of the environment and climate. When non-sustainable power sources show signs of rising temperatures and sea levels, more frequent and severe natural disasters, and serious threats to biodiversity, sustainable solar energy and photovoltaics will take over as the primary power producers in the ecosystem. Traditional solar cells are difficult because they rely on scarce and expensive elements like silicon, cadmium, and gallium, which are not ecologically benign [2]. As a result, there is a demand for environmentally friendly and cost-effective alternative materials and procedures.

Research is ongoing in developing solar cells that mimic biological processes, such as photosynthesis. These biologically inspired solar cells may use organic

materials or biomimicry to improve efficiency. This review paper suggests the creation of a novel bio-solar cell and photovoltaics design that harnesses solar energy using natural resources and artificial intelligence. Gerald Pearson, Calvin Fuller, and Daryl Chapin developed the silicon photovoltaic (PV) cell in 1954 at Bell Laboratories in New York. This one was the first solar cell to generate enough electricity from solar radiation to operate typical home appliances [3]. The potential applications of biogenic solar power augmented by AI are as diverse as they are promising. From urban landscapes adorned with solar-integrated buildings that mimic the efficiency of leaves to remote regions powered by self-sustaining biogenic solar grids, the future holds a tapestry of possibilities [4].

Michael Grätzel and Brian O'Regan, scientists, invented the first dye-sensitive solar cell in 1991 (DSSC). These hybrid solar cells use organic and inorganic materials [5]. The efficiency of solar-to-electric conversion using organometallic dyes such as ruthenium and porphyrins has been quite high for developing DSSCs [6]. According to a Scopus database search, 92 papers on AI-enabled design for biogenic solar cells were published in 2021, an increase from 14 in 2010. This suggests that demand for this subject is increasing, and there may be room for more research and development in the coming years. From 2010 to 2023, the cost of solar photovoltaic (PV) technology fell by 15% each year, indicating a learning rate of roughly 20% per doubling of installed capacity. During this time, installed capacity expanded by 25% annually, contributing to cost savings. In parallel, onshore wind capacity increased by 12% annually, doubling a 10% learning rate per capacity. If these rapid advancements continue, solar PV and wind power are projected to become the dominant players in the electrical landscape within the next 1–2 decades [7]. Their lower expenses and rapid expansion greatly outperform other alternatives. Solar energy, like other discoveries, began in niche sectors, providing electricity to applications with few options in space and isolated locations. Since then, cumulative investments and sales, spurred by previous policies, have reduced its cost by nearly three orders of magnitude. The implementation of feed-in tariffs, primarily in Germany, inspired a volume of investment and cost reductions, bringing the technology to mainstream markets following Chinese engagement in supply chains [8].

1.2. Green resources for solar power

From traditional energy sources to the burgeoning era of renewables, this part lays the groundwork for understanding why green resources are an option and a requirement for a robust and sustainable future. Passive use of green resources not only changes the energy landscape but also makes a substantial contribution to environmental conservation. The harmonic integration of green resources with solar power systems has inherent benefits such as reduced carbon emissions, ecological preservation, and climate change mitigation [9]. These materials provide a novel way to supplement solar electricity by turning mechanical vibrations into electrical energy via a passive process. Integration into solar panels allows energy extraction from ambient vibrations, such as wind, footsteps, and other minor movements. This inconspicuous strategy quietly improves the overall efficiency of solar systems [10]. Solar paint uses photovoltaic particles to harness sunlight and turn it into power,

allowing surfaces to be passively transformed into energy-generating assets. This technique, which can be applied as easily as traditional paint, shows the passive integration of renewable energy solutions into our daily lives by transforming buildings into passive contributors to the solar power grids, as stated below [11]:

Microbial fuel cells (MFCs): MFCs are a groundbreaking development in biogenic solar power. Bacteria, byproducts of organic matter decomposition, produce electricity when they metabolize. Utilizing this microbial metabolism introduces a sustainable and passive technique of solar energy conversion.

Bioluminescent algae: bioluminescent algae, which produce natural light, provide a novel application in solar power. Researchers are looking into genetically engineering these organisms to increase their light production, perhaps providing a biogenic source of passive solar energy [12].

Biogenic resources in solar panels: Incorporating biogenic resources into standard solar panels represents a paradigm shift. Coating solar cells with microbial coatings or embedding bioluminescent algae in panels improves their efficiency by passively increasing light absorption.

Biohybrid solar cells: Biohybrid solar cells combine the benefits of biological systems and synthetic materials. Adding microbial fuel cells or bioluminescent algae into these cells creates a new passive way of generating solar power [13]. Despite the promise, challenges such as scalability, long-term viability, and ethical considerations surrounding genetic modification need careful consideration. Addressing these challenges is crucial for successfully implementing biogenic solar power solutions. This review uses IEA data for historical power generation, capital and operational costs, and BNEF data for capacity factors, construction, and lifespans through 2020.

Additionally, IRENA provides data on historical renewable energy capacity from 2019 to 202. Regarding technical developments, their adoption rates are controlled by how long they spread, which is decided by their life cycle turnover. Cars have a half-life of 10 to 15 years; fossil fuel plants last 25 to 40 years; and long-lived infrastructure like nuclear plants and hydro dams lasts 50 to 100 years. These longer lifespans avoid abrupt shifts in technical orientation. The persistence of the development direction, or degree of inertia, shows that forecasts of energy system technology, taking observed diffusion and cost trajectories into account, can be reliable for at least 15–20 years, albeit with a widening margin of error over time. **Figure 1** displays the global distribution of energy output across 11 important technologies. The current energy mix is diversified, but E3ME-FTT forecasts indicate that solar PV will dominate by the middle of the century, even without extra renewables regulations.

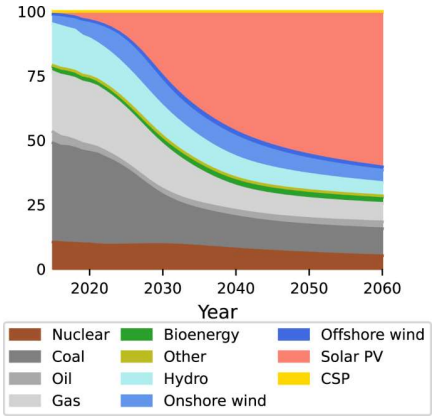

Figure 1. Presentation of worldwide share in electricity generation of various renewable energies, with solar energy responsible for 56% of production [14].

2. Biogenic solar power

The bio-solar cell was composed of a transparent conductive substrate coated with a layer of CNCs. Green chemistry was used to immobilize chlorophyll, a photosensitizer, onto the CNC surface, and CNCs functioned as a scaffold for it. In addition to working as a photosensitizer, chlorophyll was responsible for absorbing light and creating electricity [15].

The systems in most of the literature review showed up to 5.6% power conversion efficiencies, more significant than most published numbers for bio-solar cells. It was found that the organic polymer substrate dissolved fully in the soil in about two months and that the devices had good stability and durability. The biophotovoltaic cell has been evaluated using a variety of techniques, including UV-vis spectroscopy, electrochemical impedance spectroscopy (EIS), scanning electron microscopy (SEM), and current-voltage (I-V) measurements. The electrical efficiency of a regular solar cell was compared to that of a bio-solar cell. According to EIS testing, the biosolar cell has a lower charge transfer resistance than a standard solar cell, indicating greater charge collection efficiency. The biosolar cell performed better based on I-V measurements, as evidenced by increased short-circuit current density and fill factor [16]. AI algorithms can predict the energy yield of photovoltaic materials, and bio-solar cell design parameters are adaptable, as illustrated in **Figure 2(a,b)**. The optimal design had a microbe density of 1×10^9 cells/cm^2 and a 100 nm semiconductor film thickness. The bio-solar cell's open-circuit voltage was 0.4 V, the fill factor (FF) was 0.47, and the short-circuit current density (Jsc) was around 6.5 mA/cm^2.

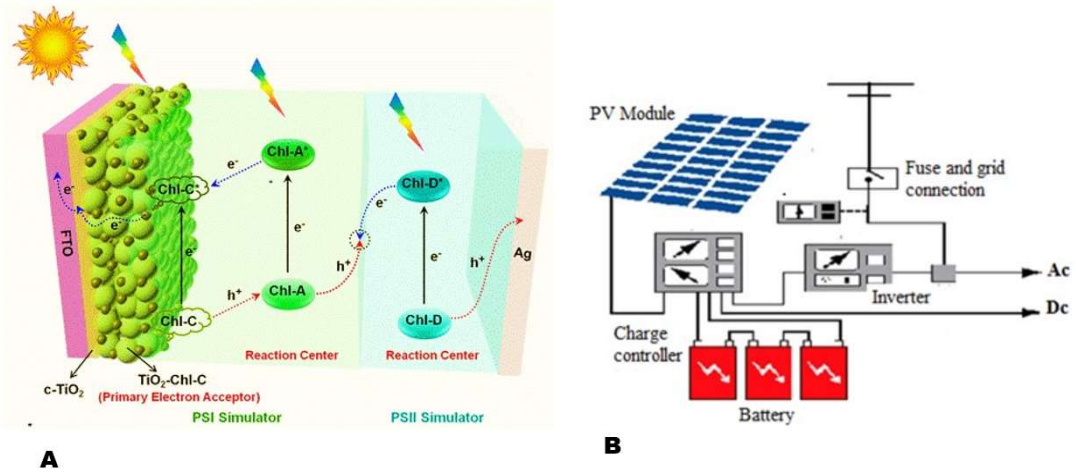

Figure 2. (a) Triple-layer chlorophyll-based bio-solar modules [17]; **(b)** Schematic diagram of BIPV [17].

The fundamental principles involve using biological things like plants, bacteria, and algae to collect and transform sunlight into useful energy passively. Understanding photosynthesis, microbial metabolism, and bioluminescence is essential for creating efficient biogenic solar power systems. Artificial intelligence is emerging as a critical factor in optimizing and managing biogenic solar power systems. This study investigates the mutually beneficial link between living creatures and AI, emphasizing the possibilities for intelligent control, predictive analytics, and adaptive energy management. Machine learning algorithms analyze and anticipate energy production trends, allowing for real-time changes to maximize efficiency. Autonomous systems are designed for maintenance, cleaning, and monitoring, assuring biogenic solar farms' ongoing and optimal operation [18].

Case study

The purpose of this case study is to develop a tool, known as the AIQ-Model, for better communication regarding "energy-producing solar shading" in the context of a specific form of Building Integrated Photovoltaics (BIPV) called BIPV shading devices. The impetus for this tool stems from the observation by several writers of the necessity for a comprehensive communication language or tool for BIPV design. The purpose is to remedy the field's lack of a common methodology. In response to this need, an evaluation technique for architectural integration qualities was created, represented visually by a triangle with corners representing geometry, materiality, and detailing. The goal is to examine how effectively a solar shading system corresponds with the overall architecture of a structure [19]. According to the literature review, the AIQ-Tool was useful during a test focus group, allowing members to share their opinions on architectural integration and sparking good discussions.

Interestingly, while architects were the principal users, discussions were enhanced by the participation of professionals from other disciplines. However, the developers admit the tool's limitations, namely its emphasis on "external integration and aesthetics." They contend that this narrow focus ignores the interdisciplinary components of solar building design, necessitating multifunctional energy planning from multiple perspectives [20].

3. AI improvement

To optimize the performance of photovoltaic components, we used artificial intelligence algorithms to mimic and anticipate their features. We employed a machine learning model to forecast the optimal thickness of the titanium dioxide layer and natural pigment phase, which were important variables influencing device efficiency. The model based on a literature review was built using data on the effectiveness of simulated solar cells at various layer thicknesses, and it predicted the right thickness with great accuracy. We built the photovoltaic gadget after optimizing it with chemical synthesis, inkjet printing, and spin coating methods [21]. The cell was made using previously identified sustainable components, and its efficiency, output voltage, and current capacity were assessed using various electrical and optical characterization techniques. We also tested the cell's resilience and endurance under different climatic conditions. AI algorithms optimize energy storage by forecasting demand patterns, weather conditions, and consumption trends, resulting in more efficient use of stored energy and less waste. Integrating AI into energy systems enables autonomous decision-making using real-time data. This involves automatically altering solar panel orientations, coordinating energy delivery, and responding to demand variations [22]. Zade presented the idea of fuzzy logic for the first time. Applying fuzzy logic fundamentals results in more straightforward progress and precise outcomes. Employing fuzzy logic and ANN techniques simultaneously delivers the ANN's online learning capabilities and the flexibility of fuzzy logic. ANFIS is built on the use of fuzzy logic and ANN simultaneously. Fuzzy inference systems have two primary arrangements: (a) Mamdani and (b) Takagi-Sugen [23]. Optimization algorithms are the foundation of intelligent decision-making in biogenic solar power. This review explains how these algorithms simplify procedures, increase efficiency, and contribute to the overall optimization of solar energy systems.

Optimization algorithms alter solar panel orientations in real time to provide optimal sunshine exposure. This adaptability improves energy absorption and conversion efficiency, particularly in biogenic solar systems, where the presence of living organisms introduces variables. Efficiency in energy storage and distribution is critical in biogenic solar systems. Optimization algorithms control these processes by analyzing demand patterns, weather forecasts, and grid conditions, ensuring biogenic energy is seamlessly integrated into existing infrastructure [24,25]. Machine learning algorithms, spanning from supervised to unsupervised learning, find use in many aspects of biogenic solar power. Supervised learning methods, such as regression and classification, are essential for estimating solar energy output. These algorithms understand patterns and relationships from prior data, allowing them to anticipate energy production accurately based on environmental parameters. Clustering and anomaly detection are unsupervised learning methods that help monitor system health. These algorithms enable proactive maintenance and troubleshooting of biogenic solar systems by detecting abnormalities in their operation [26]. Efficiency in energy storage and distribution is critical in biogenic solar systems. Optimization algorithms control these processes by analyzing demand patterns, weather forecasts, and grid conditions, ensuring biogenic energy is seamlessly integrated into existing infrastructure [27]. The interaction of machine learning, predictive analytics, and

optimization algorithms results in a unified and intelligent framework for biogenic solar power. This literature review aims to provide an overview of solar PV technology, RE hybrids, installation status, configuration trends, policies, and problems. This foundation for future study involves a comprehensive compilation of components that bring the target to reality. **Figure 3a** depicts the increase in photovoltaic power efficiency due to the convergence of solar energy with artificial intelligence. **Figure 3b** shows a year-wise statistical analysis of publications focusing on green methanol, green ammonia, and green hydrogen production from biogenic bacteria.

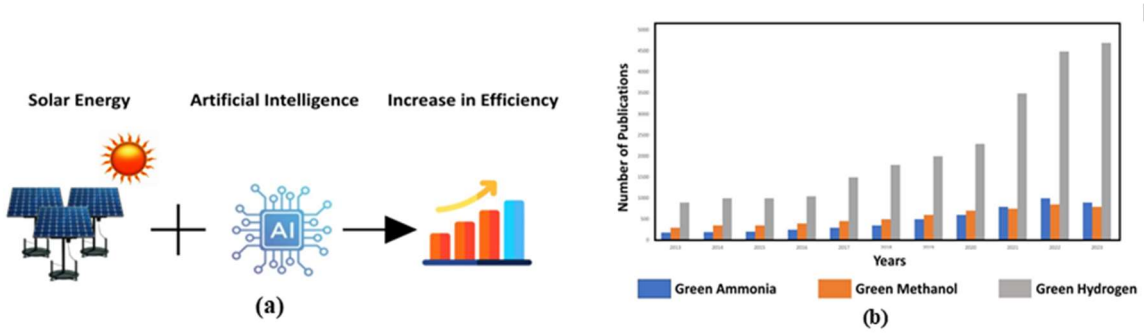

Figure 3. (a) scheme showing the integration of solar energy and AI to increase power generation efficiency; **(b)** statistical presentation of publications based on green methanol, green ammonia, and green hydrogen from biogenic bacteria year-wise.

4. Challenges and future scope

Researchers at Newcastle University have developed environmentally friendly, high-efficiency photovoltaic cells with a power conversion efficiency of 38%. These cells are intended to power Internet of Things (IoT) devices using ambient light. The dye-sensitized cells, which use a copper (II/I) electrolyte, are non-toxic and environmentally friendly, potentially revolutionizing the way IoT devices are powered and encouraging sustainable development in industries such as healthcare and manufacturing. The team also developed an energy management technique using long short-term memory (LSTM) artificial neural networks to forecast deployment conditions and alter IoT sensor computational loads, optimizing energy consumption and minimizing power losses [28–30]. Machine learning algorithms can improve water resource management, increasing the efficiency and sustainability of hydroelectric systems within the larger biogenic solar power framework [31].

As AI and biogenic solar power integration improve, obstacles such as algorithmic complexity, data privacy, and system interoperability must be overcome. This section highlights potential obstacles and suggests solutions to overcome them. The ethical considerations of using artificial intelligence with biological organisms to produce energy are substantial. This chapter investigates concerns about genetic changes, data privacy, and the proper use of AI in the search for renewable energy [32]. Even with current technological advancements, the average cost of solar energy generation is exceptionally high compared to conventional technologies and renewable alternatives. Although there are numerous solutions for storing energy

generated by solar energy or any other energy source, none are considered the best. Many green nanostructures are biodegradable and can deteriorate over time, limiting photovoltaic cell performance and longevity [33]. AI-based designs might potentially be restricted by data availability and quality. Incorrect or inadequate data might result in inaccurate forecasts and inferior layouts. Other governance and land availability challenges must be addressed while constructing on-grid PV. Available groundwater and solar energy access in sensitive watersheds may jeopardize water security through excessive abstraction. Solar power generation is inherently unreliable due to its reliance on weather deviations; to estimate how well solar power generation can generate energy at a specific location at a particular moment, weather predictions must be prepared in advance [34]. One of the limitations of the research is that solar cells have a lower power conversion efficiency (PCE) than conventional PV cells. Since solar energy only lasts for one day, the amount of storage needed for the long term is measured in hours. Since thermal energy storage technology has become an essential part of CSP systems, it has been the focus of this research. The total installation costs for CSP plants with TES are typically greater than those without, but storage makes capacity factors more noticeable. Phase change materials (PCM) are employed as storage media in concentrated solar power plants, along with sensible gas-state, sensible solid-state, sensible liquid-state, and thermochemical materials (CSP) [35].

5. Conclusive remarks

This review presents an innovative strategy for designing and developing bio-solar systems and photovoltaics using natural products and AI algorithms. We combined plants that produced electricity with photovoltaic electronics to create a hybrid bio-solar cell and proposed a thin-film solar cell made of sustainable ingredients as a component of the bio-solar cell, using AI approaches to optimize device performance. The introduction of AI models aided in reducing development time and costs, reducing carbon footprints, and making large-scale production feasible. In light of advancements in human welfare and education, it is anticipated that the proliferation of solar PV systems installed in rural areas will stimulate the economic development of these communities. Even though a PV system's initial cost is now considerable, continued material and energy efficiency advancements could considerably lower it. A complete transition from fossil fuels to sustainable solar energy would necessitate closer collaboration between governmental bodies, non-governmental organizations, the scientific community, and enterprises for the next few decades. The bio-solar cell addressed here is an environmentally friendly substitute for conventional solar cells since it was designed and constructed with green nanotechnology. AI algorithms have been utilized to improve the instrument's performance, resulting in increased productivity and a longer lifespan in the future.

Acknowledgments: The author (SR) would like to acknowledge 'Scheme for Transformational and Advanced Research in Sciences (STARS)' (MoE-STARS/STARS-2/2023-0175) by the Ministry of Education, Government of India for promoting translational India-centric research in sciences implemented and managed by Indian Institute of Science (IISc), Bangalore, for their support.

Conflict of interest: The authors declare no conflict of interest.

References

1. Dubey S, Jadhav NY, Zakirova B. Socio-Economic and Environmental Impacts of Silicon Based Photovoltaic (PV) Technologies. Energy Procedia. 2013, 33: 322-334. doi: 10.1016/j.egypro.2013.05.073
2. Fraas LM. History of Solar Cell Development. In Low-Cost Solar Electric Power. Springer International Publishing; 2013. pp. 1–12.
3. Goetzberger A, Luther J, Willeke G. Solar cells: past, present, future. Solar Energy Materials and Solar Cells. 2002, 74(1-4): 1-11. doi: 10.1016/S0927-0248(02)00042-9
4. Lyu S, Bertrand C, Hamamura T, et al. Molecular engineering of ruthenium-diacetylide organometallic complexes towards efficient green dye for DSSC. Dyes and Pigments. 2018, 158: 326-333. doi: 10.1016/j.dyepig.2018.05.060
5. Bera S, Sengupta D, Roy S, et al. Research into dye-sensitized solar cells: a review highlighting progress in India. Journal of Physics: Energy. 2021, 3(3): 032013. doi: 10.1088/2515-7655/abff6c
6. De A, Bhattacharjee J, Chowdhury SR, et al. A Comprehensive Review on Third-Generation Photovoltaic Technologies. Journal of Chemical Engineering Research Updates. 2023, 10: 1-17. doi: 10.15377/2409-983x.2023.10.1
7. Palacios A, Barreneche C, Navarro ME, et al. Thermal energy storage technologies for concentrated solar power – A review from a materials perspective. Renewable Energy. 2020, 156: 1244-1265. doi: 10.1016/j.renene.2019.10.127
8. Kim SG, Jung JY, Sim M. A Two-Step Approach to Solar Power Generation Prediction Based on Weather Data Using Machine Learning. Sustainability. 2019, 11(5): 1501. doi: 10.3390/su11051501
9. Samuel MS, Ravikumar M, John J. A, et al. A Review on Green Synthesis of Nanoparticles and Their Diverse Biomedical and Environmental Applications. Catalysts. 2022, 12(5): 459. doi: 10.3390/catal12050459
10. Parthiban R, Ponnambalam P. An Enhancement of the Solar Panel Efficiency: A Comprehensive Review. Frontiers in Energy Research. 2022, 10. doi: 10.3389/fenrg.2022.937155
11. Freire-Gormaly M, Bilton AM. Design of photovoltaic powered reverse osmosis desalination systems considering membrane fouling caused by intermittent operation. Renewable Energy. 2019, 135: 108-121. doi: 10.1016/j.renene.2018.11.065
12. Paletta Q, Terrén-Serrano G, Nie Y, et al. Advances in solar forecasting: Computer vision with deep learning. Advances in Applied Energy. 2023, 11: 100150. doi: 10.1016/j.adapen.2023.100150
13. Sharma N, Puri V, Mahajan S, et al. Solar power forecasting beneath diverse weather conditions using GD and LM-artificial neural networks. Scientific Reports. 2023, 13(1). doi: 10.1038/s41598-023-35457-1
14. Nijsse FJMM, Mercure JF, Ameli N, et al. The momentum of the solar energy transition. Nature Communications. 2023, 14(1). doi: 10.1038/s41467-023-41971-7
15. Ye L, Zhang S, Ma W, et al. From Binary to Ternary Solvent: Morphology Fine-tuning of D/A Blends in PDPP3T-based Polymer Solar Cells. Advanced Materials. 2012, 24(47): 6335-6341. doi: 10.1002/adma.201202855
16. Roy S, Botte GG. Perovskite solar cell for photocatalytic water splitting with a TiO2/Co-doped hematite electron transport bilayer. RSC Advances. 2018, 8(10): 5388-5394. doi: 10.1039/c7ra11996h
17. Zhao W, Dall'Agnese C, Duan S, et al. Trilayer Chlorophyll-Based Cascade Biosolar Cells. ACS Energy Letters. 2019, 4(2): 384-389. doi: 10.1021/acsenergylett.8b02279
18. Grott S, Kotobi A, Reb LK, et al. Solvent Tuning of the Active Layer Morphology of Non-Fullerene Based Organic Solar Cells. Solar RRL. 2022, 6(6). doi: 10.1002/solr.202101084
19. Attoye D, Adekunle T, Tabet Aoul K, et al. A Conceptual Framework for a Building Integrated Photovoltaics (BIPV) Educative-Communication Approach. Sustainability. 2018, 10(10): 3781. doi: 10.3390/su10103781
20. Li S, Liu L, Peng C. A Review of Performance-Oriented Architectural Design and Optimization in the Context of Sustainability: Dividends and Challenges. Sustainability. 2020, 12(4): 1427. doi: 10.3390/su12041427
21. Freire-Gormaly M, Bilton AM. Impact of intermittent operation on reverse osmosis membrane fouling for brackish groundwater desalination systems. Journal of Membrane Science. 2019, 583: 220-230. doi: 10.1016/j.memsci.2019.04.010
22. Zhang W, Saliba M, Stranks SD, et al. Enhancement of Perovskite-Based Solar Cells Employing Core–Shell Metal Nanoparticles. Nano Letters. 2013, 13(9): 4505-4510. doi: 10.1021/nl4024287
23. Srivastava SK, Piwek P, Ayakar SR, et al. A Biogenic Photovoltaic Material. Small. 2018, 14(26). doi: 10.1002/smll.201800729

24. Lee J, Choi J, Park W, et al. A Dual-Stage Solar Power Prediction Model That Reflects Uncertainties in Weather Forecasts. Energies. 2023, 16(21): 7321. doi: 10.3390/en16217321
25. Mehdinia A, Mehrabi H. Application of nanomaterials for removal of environmental pollution. In: Thomas S, Grohens Y, Pottathara YB (editors). Industrial Applications of Nanomaterials. Elsevier; 2019. pp. 365-402. doi: 10.1016/b978-0-12-815749-7.00013-x
26. Abdelkareem MA, El Haj Assad M, Sayed ET, et al. Recent progress in the use of renewable energy sources to power water desalination plants. Desalination. 2018, 435: 97-113. doi: 10.1016/j.desal.2017.11.018
27. Bera S, Saha A, Mondal S, et al. Review of defect engineering in perovskites for photovoltaic application. Materials Advances. 2022, 3(13): 5234-5247. doi: 10.1039/d2ma00194b
28. Richards BS, Shen J, Schäfer AI. Water–Energy Nexus Perspectives in the Context of Photovoltaic-Powered Decentralized Water Treatment Systems: A Tanzanian Case Study. Energy Technology. 2017, 5(7): 1112-1123. doi: 10.1002/ente.201600728
29. Ben Ali I, Turki M, Belhadj J, et al. Using quasi-static model for water/power management of a stand-alone wind/photovoltaic/BWRO desalination system without batteries. In: Proceedings of the 2016 7th International Renewable Energy Congress (IREC); 22-24 March 2016; Hammamet, Tunisia. pp. 1-6. doi: 10.1109/irec.2016.7478871
30. Kharraz JA, Richards BS, Schäfer AI. Autonomous Solar-Powered Desalination Systems for Remote Communities. In: Arafat HA (editor). Desalination Sustainability: A Technical, Socio-Economical and Environmental Approach. Elsevier; 2017. pp. 75-125. doi: 10.1016/b978-0-12-809791-5.00003-1
31. Wang D, Zhou G, Li Y, et al. High-Performance Organic Solar Cells from Non-Halogenated Solvents. Advanced Functional Materials. 2021, 32(4). doi: 10.1002/adfm.202107827
32. Richards BS, Capão DPS, Früh WG, et al. Renewable energy powered membrane technology: Impact of solar irradiance fluctuations on performance of a brackish water reverse osmosis system. Separation and Purification Technology. 2015, 156: 379-390. doi: 10.1016/j.seppur.2015.10.025
33. Danladi E, Ichoja A, Onoja ED, et al. Broad-band-enhanced and minimal hysteresis perovskite solar cells with interfacial coating of biogenic plasmonic light trapping silver nanoparticles. Materials Research Innovations. 2023, 27(7): 521-536. doi: 10.1080/14328917.2023.2204585
34. Meena RS, Singh A, Urhekar S, et al. Artificial Intelligence-Based Deep Learning Model for the Performance Enhancement of Photovoltaic Panels in Solar Energy Systems. International Journal of Photoenergy. 2022, 2022: 1-8. doi: 10.1155/2022/3437364
35. Mateo Romero HF, González Rebollo MÁ, Cardeñoso-Payo V, et al. Applications of Artificial Intelligence to Photovoltaic Systems: A Review. Applied Sciences. 2022, 12(19): 10056. doi: 10.3390/app121910056

Energy Storage and Conversion 2024, 2(1), 491.
https://doi.org/10.59400/esc.v2i1.491

Review

Battery and/or supercapacitor?—On the merger of two electrochemical storage system families

Yuping Wu[1], Rudolf Holze[1,2,3,4,*]

[1] Confucius Energy Storage Lab, School of Energy and Environment, Southeast University, Nanjing 210096, China
[2] Chemnitz University of Technology, 09107 Chemnitz, Germany
[3] Institute of Chemistry, Saint Petersburg State University, Petersburg 199034, Russia
[4] School of Energy and Environment, Southeast University, Nanjing 210096, China
*** Corresponding author:** Rudolf Holze, rudolf.holze@chemie.tu-chemnitz.de

CITATION

Wu Y, Holze R. Battery and/or supercapacitor?—On the merger of two electrochemical storage system families. Energy Storage and Conversion. 2024; 2(1): 491. https://doi.org/10.59400/esc.v2i1.491

ARTICLE INFO

Received: 15 January 2024
Accepted: 17 February 2024
Available online: 8 March 2024

COPYRIGHT

Copyright © 2024 by author(s). *Energy Storage and Conversion* is published by Academic Publishing Pte. Ltd. This work is licensed under the Creative Commons Attribution (CC BY) license. https://creativecommons.org/licenses/by/4.0/

Abstract: Similarities and analogies between materials, structures, operating and construction principles of secondary batteries and supercapacitors and their electrodes are presented, named, and reviewed in context. On the material level, several materials used both in batteries and supercapacitors are addressed, and implications from observations made in one application for the other are highlighted. On the electrode level, a continuous change of architectural details is observed when going from an electrode with high charge storage capability to an electrode supporting high currents is detected; again, this overlap provides instructive ideas for both fields. On the cell level, combinations of electrodes from both fields yielding hybrid devices are an obvious outcome again, with implications for both fields. Ideas and suggestions for further research and development based on a deeper exchange between both families are developed.

Keywords: battery electrodes; supercapacitor electrodes; capacitive behavior; pseudocapacitive behavior; electrochemical energy storage; electrochemical energy conversion

1. Introduction

Electrical energy can be stored by various means and procedures [1]. A fundamental difference between the various principles and systems of electrical energy storage (EES) is related to the question of whether storage proceeds directly without any conversion process or whether such a mechanical, physical, or chemical conversion process of, e.g., electrical energy into chemical energy is required. The essentials are schematically depicted in **Figure 1**.

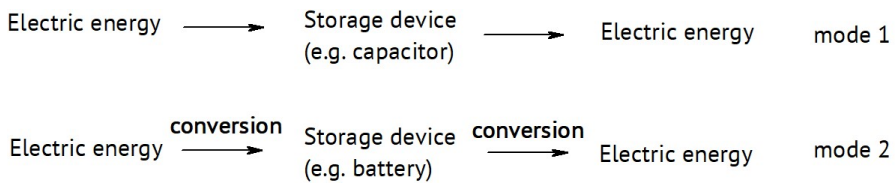

Figure 1. Basic modes of EES.

A typical, prominent, and highly successful example of the first mode is the capacitor; an equally popular and successful example of the second mode is the rechargeable battery. Discoveries of fundamental principles like static electricity for the former device as well as inventions like the lead-acid battery for the latter one are items in the history of science and technology frequently retold in textbooks and

reviews [1,2]. The very different origins of these two principles kept both technologies apart from each other, with only minor exceptions of overlaps or interactions like the electrochemical treatment of aluminum foils for electrolytic capacitors. Although the latter device has even more connections to electrochemistry than a plain surface treatment, such capacitors have never been considered electrochemical energy storage devices for a simple reason: Storage in capacitors without any conversion reaction is based simply on the separation of electric charges on two metal plates (electrodes), whereas storage in a battery is based on a faradaic (redox) reaction with associated more or less extended chemical transformations of the electrode materials (for a scheme and an example, see **Figure 2**).

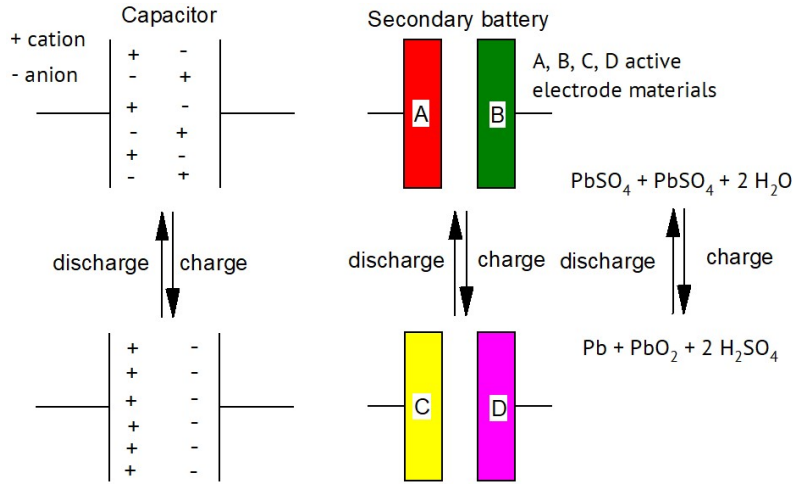

Figure 2. Schematic principles of operation of a capacitor and a secondary battery (with a typical example).

The electrochemical double layer (EDL) established at the interface between an electronic conductor (e.g., a metal electrode) and an ionically conducting phase (an electrolyte solution) is not a recent observation but has been studied, modeled, and measured for decades [3]. Finally, the reports and patents by Becker [4] and Rightmire [5] have moved this omnipresent capacitive property of an electrochemical phase boundary into the view of electrical engineers. This development resulted in the now very popular supercapacitor[1] of the electrochemical double layer capacitor-type (EDLC) [6]. Although the storage principle is again the separation of electric charges, like with the conventional capacitor, the participation of ions in the electrolyte solutions balancing the electric charges in the electrode (the electronically or the hole-conducting conducting phase) has made supercapacitors a highly attractive research topic for electrochemists, although no faradaic or redox reactions proceed at the electrode during storage and release of electrical energy.

Supercapacitors have been established as means of EES in a vast range of sizes, from tiny ones in environmental and medical applications across numerous mobile applications, e.g., telecommunication, to large ones in electric vehicles and supply systems in mass transit. Introductory overviews are available [7–13], in numerous monographs, presumably all aspects, from basic functional principles on to materials and applications, are treated [14–22]. A review of self-discharge as a major drawback of EDLC devices is available [23]. The essential role of secondary batteries is stressed

almost everywhere in the introduction of every publication on topics related to them; their still-growing importance in mobility and in the use of renewable energies is well-established [1,2,24].

Because the storage capability of an EDLC is fundamentally limited by the size of the interfacial area (between the electronically conducting phase, the electrode, and the ionically conducting phase [25]), the amount of charge possibly stored in such a device is limited, and accordingly, the energy, too.

The observation that some surface-confined redox reactions on electrode surfaces show a current response to a changing electrode potential very similar to that of a capacitor (they behave almost like the electrochemical double layer) [26] has stimulated still-booming research into redox-active materials for supercapacitor electrodes. Some of these materials are also encountered in primary and secondary batteries; the design principles as well as electrode chemistries of some battery and supercapacitor electrodes are very similar or just the same. This fact has initiated a discussion about the possibly ongoing merger of secondary batteries and supercapacitors. Or, in other words, secondary batteries and supercapacitors are basically based on the same principles, differing only in details. The overlap and/or merger may proceed if this observation is correct beyond the author's personal opinion on various levels beyond those already mentioned: Combination of battery electrodes and supercapacitor electrodes in advanced lead acid systems, as suggested by Shukla et al. [27], on the device or cell level, as well as use of electrodes containing both a redox-active electrode material and a capacitive one [1] on the electrode level. These concepts have been sometimes named hybrid ones for both levels [28,29]. On the cell level, the term asymmetric frequently shows up [30]. The term "hybridisation" or "hybrid" appeared in the present context some time ago [31]. Some of the resulting electrodes and full devices mostly discussed in terms of hybridisation may actually be called the results of said merger, but the term has not been applied before. Given the absence of a clear definition of this term, it does not surprise that this report deals mostly with combinations of battery and supercapacitor electrodes (called asymmetric devices elsewhere); for an example, see below. Some further thoughts related to distinguishing between supercapacitors and batteries have been provided elsewhere [32].

Beyond the conceivable merger of two fields and their constituents, some confusion regarding terminology and understanding seems to be looming, too. Generous creation of acronyms adds to this. The temptation to create further terms in a sometimes rather vain attempt to create something quotable has resulted, among others, in positrode and negatrode (apparently instead of positive and negative electrodes, simply) or supercapattery naming a device combining aspects of secondary batteries and supercapacitor behaving more like a supercapacitor (i.e., have somewhat higher power output) and supercabattery (the same, but somewhat higher energy output) [33–35].

Whereas in "electrochemical double layer capacitors" the principle of the electrochemical double layer, in particular its capacitive behavior, is utilized (see **Figure 2**) in supercapacitors of the redox type and their materials discussed in this report, redox processes, in particular those proceeding close to the electrode/electrolyte (solution) interface (so-called superficial, see **Figure 3**), are used

in addition for charge and subsequently energy storage [36,37]. In contrast to battery electrodes, wherein redox transformations proceed all over the volume (at least in the desired ideal case of complete mass utilization), only the topmost layer(s) of the material is used for energy storage in a supercapacitor application. Nevertheless, an increase in storage capability by 2 to 3 orders of magnitude has already been estimated in the first reports suggesting this approach [37]. Typical advantages of the EDLC, in particular the extremely fast charge and energy storage and release because of the purely capacitive processes only limited in terms of current by the internal resistance (electrical series resistance (ESR)) and not impeded by any chemical or electrochemical reaction, are only slightly diminished when utilizing surface-confined processes in redox supercapacitors. As an alternative name, the term Faradaic supercapacitor [6] has been used[2].

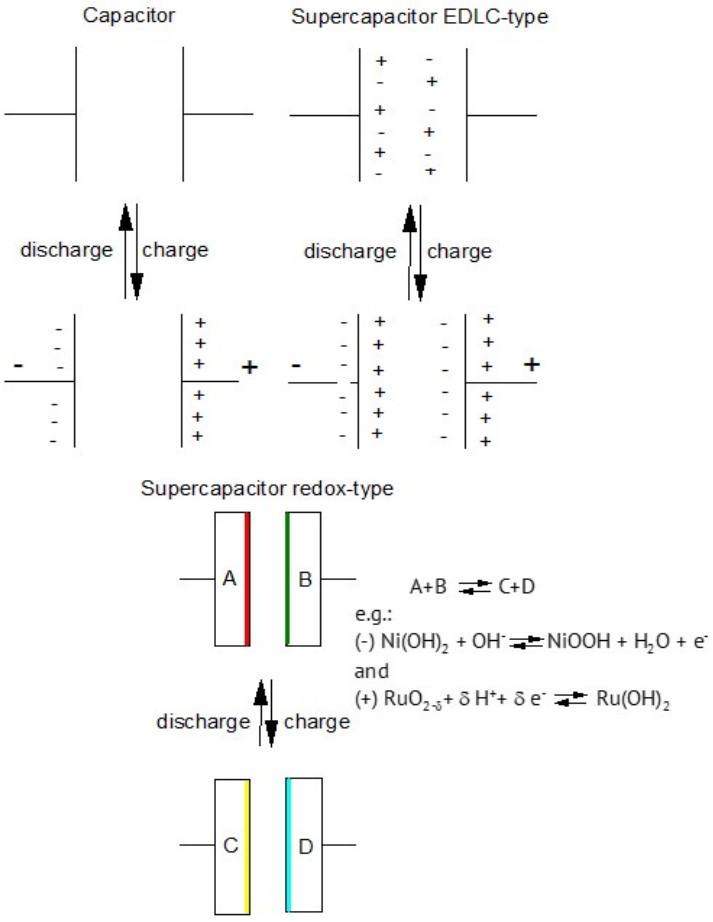

Figure 3. Charge distribution during operation in a conventional capacitor and in EDLC and redox-supercapacitors.

Reports on similarities and connections between the two families of energy storage systems seem to coincide with communications on differences and boundaries. Unfortunately, imprecise use of terminology sometimes ending in simple contradictions within a report has turned out to be more confusing than helpful [38]. A recent update has attempted to provide some clarification [39].

Following, we will inspect approaches, mergers, and overlaps between the two fields on various levels, starting at an atomistic or microscopic one and ending at the

device level. For the sake of clarity in this report, in a roughly simplified way, the term supercapacitor (SC) indicates an EES device providing high current (rate) capability, whereas the term secondary battery names a device with high energy storage capability. Further overlaps between aspects of both systems, like manufacturing processes, were addressed elsewhere [40].

Starting from the implicit hypothesis that redox supercapacitors and secondary batteries are actually only modified versions of the same device, this report aims at highlighting common and separating aspects of both fields, and it shall help in particular to enable "crosspollination" between the fields by suggesting possible transfers of ideas, methods, and concepts from one field into the other.

2. Chemistries, reactions, and processes—merger at the atom and molecule level

Storage of electrical energy can proceed in the simplest case of the electrostatic capacitor by separating charges. The work (energy) spent to achieve this is released again upon discharge when the temporarily separated charges are redistributed again (see **Figure 2**). This applies to the traditional capacitor in all its commercial types; it also applies to the electrochemical double-layer capacitor. The only distinction between both is the fact that in the conventional capacitor, only one charge separation across the device proceeds, whereas in the EDLC, charge separation proceeds at both electrodes (see **Figure 3**).

In a battery, energy is stored by using electric energy to drive a chemical transformation. The obtained materials are "richer in energy" (the absolute value of the Gibbs energy or free reaction enthalpy is larger) than the starting materials. As an example, the charging reaction at the negative electrode of a lead-acid battery shall be considered:

$$PbSO_4 + 2\ e^- + 2\ H^+ \rightarrow Pb + H_2SO_4 \quad (1)$$

Upon discharge the process is reversed:

$$Pb + H_2SO_4 \rightarrow PbSO_4 + 2\ e^- + 2\ H^+ \quad (2)$$

As an alternative the following reaction is conceivable

$$Pb + H_2SO_4 \rightarrow PbSO_4 + H_2 \quad (3)$$

Assigning an energy or enthalpy to both reactions (Equations (1) and (2)) is thermodynamically correct. The Gibbs energy (free reaction enthalpy) of the first process can be calculated, yielding $\Delta G_R = 68.7\ kJ \cdot Mol^{-1}$ for the charging reaction. For the discharge reaction, $\Delta G_R = -68.7\ kJ \cdot Mol^{-1}$ is obtained. In reality, the first process will not occur without applying external force. Equation (3) describes an unwelcome corrosion reaction with the two electrons used to reduce protons, but this is not the purpose of an electrode in a rechargeable battery. Quite obviously, one electrode (half-cell) does not make up a full cell; a second electrode is needed. This very simple consideration makes all considerations and calculations frequently found in scientific reports about the energy assigned to a single electrode and its reaction irrelevant. Nevertheless, the authors feel some certainty based (if they have considered this at all) on the relationship between the free enthalpy and the cell voltage U_0:

$$\Delta G_R = -n \cdot F \cdot U_0 \quad (4)$$

Although sometimes cell voltage U_0 (also called electromotive force emf) and electrode potential E are confused (some authors simply use one symbol for both), this equation certainly does not apply to an electrode. To escape this conundrum, an apparent solution is found by taking two electrode potentials from a charge/discharge experiment or a cyclic voltammogram (CV), calculating the electrode potential difference, and assuming this to be a cell voltage. But again, one electrode does not make up a cell. For lists of electrode potentials calculated from free enthalpies, it is always assumed that the second half-cell is the standard hydrogen electrode (for example, in the study by Wu and Holze [1], listings with references are available in the study by Holze [41]). At this point, it appears to be reasonable and highly recommended to assign only charge storage capabilities to a single electrode (material), possibly combined with the electrode potential, wherein this happens but no energy.

Chemistries and fundamental operating principles of both families met when first reports about the capacitive-like current response in CVs of some metal electrodes appeared and the specific current response towards a changing electrode potential was observed in CVs [37,42–45]. As an example to illustrate the phenomenon and concept (although without practical application value), CVs of a polycrystalline platinum sheet electrode in contact with an aqueous electrolyte solution of 0.05 M H_2SO_4 recorded at different scan rates are shown in **Figure 4**.

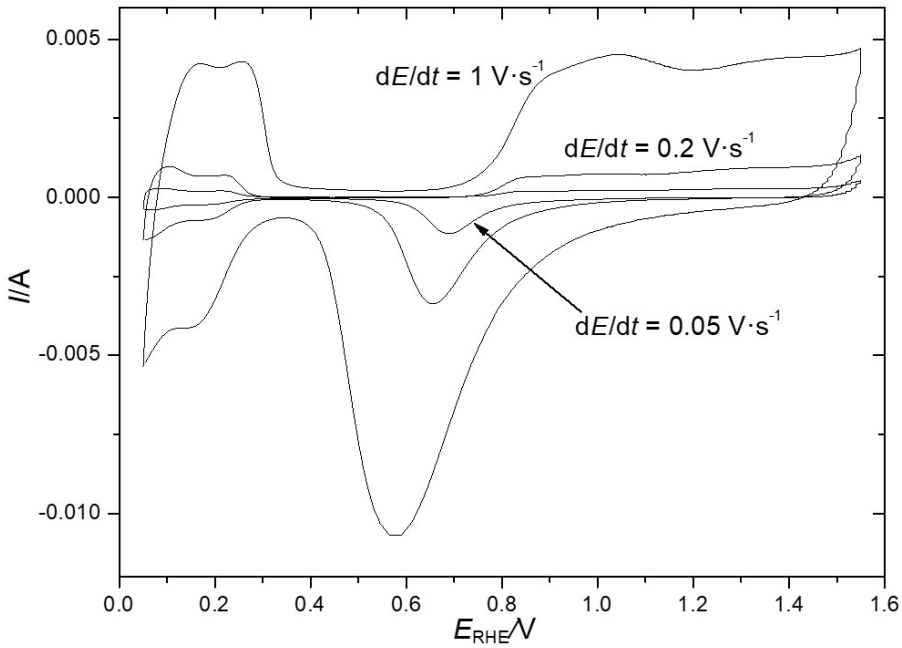

Figure 4. Selected CVs of a polycrystalline platinum electrode in contact with an aqueous electrolyte solution of 0.05 M H_2SO_4, nitrogen purged, scan rates as indicated.

Evaluation of the current response in the double layer region where no Faradaic process is observed (i.e., $0.4 < E_{RHE} < 0.6$ V) and of the current in the electrode potential region where formation of a hydroxide/oxide coverage proceeds (i.e., $0.9 < E_{RHE} < 1.5$ V) yields the following **Figure 5**.

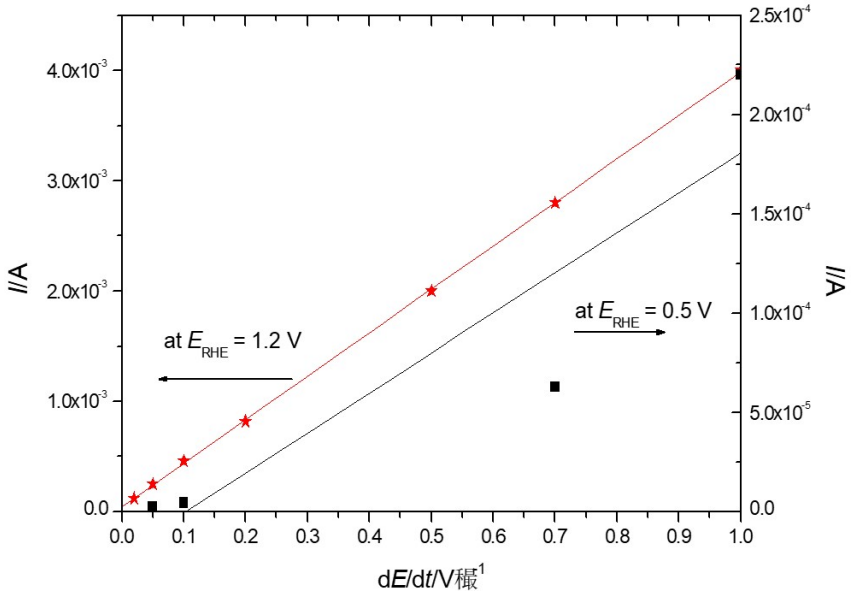

Figure 5. Current response vs. scan rate of a polycrystalline platinum electrode in contact with an aqueous electrolyte solution of 0.05 M H_2SO_4, at different electrode potentials.

Data at both electrode potentials is taken from the same cycle. Values recorded at E_{RHE} = 0.5 V are imprecise in this approach; much more precise data found in a narrow range of electrode potentials with potential scans limited to the double layer region only have been reported before [7,12,46].

From the slope of both lines (dI/dv), a differential capacitance C_{diff} can be obtained. In the case of values noted at E_{RHE} = 0.5 V, this will indeed be the double layer capacitance C_{DL}, which in turn can be used as a measure of the electrochemically active surface area (EASA) [46,47]. The currents found at E_{RHE} = 1.2 V are bigger by more than an order of magnitude and cannot be explained this way. They are due to the formation of hydroxide/oxide coverage, although the current response looks like that of a capacitor. The term *pseudocapacitive* presumably coined by Gileadi and Conway [42], simply and generally describes a response of the electrode like that of a capacitor, as shown in the preceding figures, as already suggested by the term (Greek: ψεύδειν (Pseudes): pretending, fake; in the present content, the meaning is as used in biology and botany for designing a species with the name pseudo*xxx* because it looks like *xxx* is obviously intended). The relationship between scan rate and current response can be stated as

$$I = C_{diff} \cdot dE/dt \quad (5)$$

or using $v = dE/dt$

$$I = C_{diff}\, v \quad (6)$$

This can be taken quite obviously as a specific case of a general power law relationship

$$I = a \cdot v^b \quad (7)$$

with $b = 1$ being typical of a capacitive process and behavior. In the case of the current response in the double layer region with b = 1 and $a = C_{diff}$, at E_{RHE} = 1.2 V, the response is due to a redox process, whereas the response is still behaving like a capacitive one, thus the suggested designation. At this point, it can be concluded that

the term *pseudocapacitive* is purely descriptive (and certainly makes sense only as an adjective). The extensive discussion published in numerous reports on extended terminologies of pseudocapacitance (s) appears to be rather unproductive because it only creates further terminology but fails to provide an understanding of the reasons for the current response with some materials and processes, but not all redox processes at electrodes. Attempts to get an understanding of the causes have been discussed before [26]. Meaning as well as proper application of the term "pseudocapacitive" have been subjects of heated debates [26,38,48–51]. A previous use of the term "pseudocapacity" by Grahame [52] means redox processes at the mercury electrode/aqueous electrolyte solution interface with reduction and subsequent oxidation of cadmium/cadmium ions; thus, this meaning handles solution species differently from the suggestion by Gileadi and Conway involving redox reactions of surface-attached species.

Various processes may constitute the Faradaic reaction causing this response beyond this example:

A simple redox process involving species on the electrode surface involving the electrode material itself:

$$Pt + H_2O \rightarrow PtOH + H^+ + e^- \quad (8)$$

Or a redox process of an electrochemically active coating [26].

$$RuO_{2-\delta}(OH)_\delta \rightleftarrows RuO_2 + \delta\, e^- + \delta\, H^+ \text{with } 0 \leq \delta \leq 2 \quad (9)$$

Or a redox reaction of an electrode material:

$$MnO_2 + H_2O + e^- \varnothing MnOOH + OH^- \quad (10)$$

In all cases, material and system, i.e., electrode, properties discussed elsewhere are responsible for the capacity-like (*pseudocapacitive*) current response and the absence of current peaks frequently observed in CVs obtained with redox active materials, as discussed in detail before [26]; for further considerations, see, e.g., Chen [55]. The last example (Equation (10)) already shows an overlap with battery electrode materials: Manganese dioxide is a frequently encountered material in many, mostly primary, systems [56,57]. Some materials like $RuO_2 \cdot 0.5H_2O$ show this pseudocapacitive behavior always, i.e., independent of particular preparation, morphology, particle size, etc.; they have been called intrinsically pseudocapacitive [58], whereas materials showing this property only after some "engineering" (e.g., nanostructuring, composite formation) have been called extrinsically pseudocapacitive.

All examples share common features also encountered in battery electrode chemistries and processes:

The participating species must be insoluble in the electrolyte solution.

The processes should be fast, in the frequently assumed meaning of reversible electrode kinetics as being fast.

The involved species should be readily available; even better, they should be abundant.

Preferably, they should be cheap, non-toxic, and environmentally compatible.

These general requests are already pointing into the next section, where they will be extended and specified, but some details more related to processes require attention here: Following the first patent [59], the use of redox-active, soluble species added to

the electrolyte solution was recommended in particular for supercapacitors of the EDLC-type, apparently in contradiction to request 1. As pointed out before, this setup is basically a redox flow battery without the flow [60], and without a separating membrane or an equivalent device, keeping the electrolyte solutions operating at the positive and negative electrodes from mixing may be very remarkable [23]. With a membrane instead of the highly porous separator, the internal resistance will grow, making such a device rather unattractive, at least for high-power applications. In terms of operating principle, it brings the redox flow battery and thus the idea of a battery with soluble electrode materials (e.g., the lead acid battery with soluble active materials [1,61]) into the picture. Thus, this concept is one more example of the ongoing merger. The initial concerns regarding fast self-discharge, in particular of an undivided device, can be put into perspective when considering the application: A supercapacitor used only for very short-term energy storage may not have its practical value significantly diminished by self-discharge.

Beyond the two principles of (1) charge separation in a capacitor of whatever kind and (2) a redox reaction, hardly any other process appears to be suitable to be involved in charge and thus energy storage. Nevertheless, new terms like "intercalation pseudocapacitance" were created (for an example, see the report by Lou et al. [62]). Whether they really help is doubtful and should not be discussed here; their inventors seem to overlook that "pseudocapacitive" simply describes a particular current response to a changing potential or voltage without asking for specifics of the underlying electrochemical and possibly associated further chemical processes. Because intercalation is indeed a term encountered when examining battery electrode materials, the common options of processes associated with an electrochemical charge transfer in battery electrodes should be inspected:

- Intercalation;
- Alloying;
- Conversion.

Intercalation (the term insertion is sometimes also used with intercalation, mostly applied to layered materials) itself is not an electrochemical process but a chemical reaction. Coupled with the ingress or egress of ions like, e.g., Li^+ in the negative (graphite) and positive (metal oxide) electrodes of a lithium ion battery, it is a frequently encountered material storage option currently operating in many electrodes of lithium ion batteries and capacitors. Because structural changes in the host material are mostly small, the process may be fast and thus compatible with the fast electrode reaction required for a supercapacitor. Among the many processes and associated materials (in particular metal oxides) suggested for supercapacitor electrodes, verified examples of intercalation were not reported. Actually, the electrode reactions are not even known exactly in most cases [63]. Graphite electrodes used for hosting lithium ions as employed in lithium-ion batteries are used as negative electrodes in lithium-ion capacitors; because they show no pseudocapacitive behavior, they are not considered here.

Alloying is a storage option for, e.g., silicon or tin electrodes in lithium-ion batteries. Because of the extensive structural changes, this storage process appears to be hardly suitable for supercapacitors. The reported current responses in CVs certainly do not suggest pseudocapacitive behavior.

Conversion processes as encountered with, e.g., the lead electrode in a lead-acid battery show high material utilization, and the processes inspected above for supercapacitor electrodes can be taken as typical examples despite the fact that the proceeding reactions will cause major structural changes when happening in the bulk of the electrode material. Such changes in a film of hydrous $Ru(OH)_2$ or a thin coating of electrodeposited MnO_2 are obviously no significant problem given the reported stability of related supercapacitor electrode materials.

There is a family of batteries commonly called dual-ion batteries[3] with some subspecies [64–70] wherein the redox transformation associated with charge storage as well as other conceivable modes of charge storage are not as obvious as indicated in Equations (1) and (2). In its most basic form, it is an ion intercalation/deintercalation battery with the cations M^+ and anions A^- of the electrolyte (MA) going in and out of the respective host materials (e.g., graphite).

(+) $G + x\ A^- \varnothing G(xA) + x\ e^-$ with G = graphite or another intercalation material (11)

(−) $G + xM^+ + x\ e^- \varnothing G(xM)$ with G = graphite or another intercalation material (12)

Instead of intercalation/deintercalation adsorption/desorption with the associated advantage of a high rate is conceivable [70], but a possible pseudocapacitive behavior moving such cells into the focus of this report has not been noticed.

The merger of battery and supercapacitor chemistries has been reviewed elsewhere [28].

3. Materials

Processes and operating principles outlined in the preceding section need materials enabling them; in addition, these actual materials are subject to further consideration. Electrode materials for both battery and supercapacitor electrodes (in the latter case of the redox-type) should meet certain well-established requirements, some of them more related to processes and chemistries than were already addressed in the preceding section:

For practical applications, various properties of the active masses are relevant and desirable:

- Cheap and abundant raw materials;
- Environmental compatibility;
- Fast and chemically as well as electrochemically reversible electrode kinetics;
- Mechanically stable structural integrity during charge/discharge;
- Chemically as well as electrochemically stable under all operating conditions (temperature, current);
- Sufficient electronic conductivity
- Morphology: providing a large interfacial area with electrolyte solution;
- Optimized porosity enables fast ion movement;
- Compatible with electrolyte solutions and other electrode and cell components.

3.1. Chalcogenides

This “wish list” has been common in battery research for decades; it applies as well to redox supercapacitors. Currently, predominantly compounds from the metal chalcogenide class of materials with a single metal (e.g., MnO_2), two or even three

metals (binary chalcogenides, like $Me1_xMe2_yO_z$ and related oxides like $MeMe1_xMe2_yO_z$ with Me1 and Me2 most frequently being transition metals, e.g., $CoFe_2O_4$) are encountered. With materials containing more than one kind of metal, the question of the proceeding redox reactions might be asked. Given the vast number of possible combinations of two or even three different metals, many possible redox processes, their relative likelihood, their reversibility, and their contribution to overall charge storage cannot be discussed here; this will be reported elsewhere [63]. As an example, $NiCo_2O_4$ studied by Wang et al. [71] shall be considered. The authors proposed the following redox reaction:

$$NiCo_2O_4 + OH^- + H_2O \rightleftarrows NiOOH + 2\ CoOOH + 2\ e^- \quad (13)$$

which hardly can be correct; a simple calculation shows that only one electron is released. It appears also rather unlikely that nickel cobaltite with a specific crystal structure disintegrates into two metaloxy hydroxide compounds and reassembles into the cobaltite again on the way back. In the synthesis of the material, high-temperature calcination is required for this to occur. As a follow-up reaction, Equation (14) was proposed.

$$CoOOH + OH^- \rightleftarrows CoO_2 + H_2O + e^- \quad (14)$$

No reason was provided why the reaction in Equation (15) should not proceed.

$$NiOOH + OH^- \rightleftarrows NiO_2 + H_2O + e^- \quad (15)$$

Taking this reaction into account, four electrons may be transferred when all metal ions change from their initial state of oxidation into their highest conceivable state of oxidation. It is rather astonishing to notice that there is no report addressing this question in detail, preferably using *in situ* methods sensitive to the state of oxidation. Even *ex situ* studies with, e.g., XPS possibly providing evidence of the state of oxidation of the participating metal ions at various electrode potentials where the materials were emersed from the electrolyte solution are not available.

The use of redox-active materials for charge storage instead of activated carbon or other carbonaceous materials for double-layer storage to increase storage capability comes at a price: Decreased current capability and lower stability of the materials. The former is mostly due to lower electronic conductivity and thus increased internal ohmic resistance of the material, as well as the limited rate of the redox reaction. This aspect depends on the actual material; the actual effect can be ameliorated to some degree by, e.g., nanostructuring. The reduced stability is mostly due to volume changes of the active material because redox reactions are frequently associated with further chemical and structural changes (see above, Equation (1), etc., and the report by Dubal et al. [72]). Again, suitable structuring of the active material and/or combination with auxiliary materials may help both battery and supercapacitor electrodes. A particularly popular combination includes a redox active material and some form of carbon prepared as a composite with, e.g., MnO_2 deposited on a carbon support of suitable porosity (for an overview, see Borenstein et al. [73]). Such a combination, going beyond the conventional mixing or blending of powders of active mass with, e.g., acetylene black, may even be called a hybrid. Although it appears that the term "hybrid" enjoys a rather widespread and poorly defined usage, it seems safe to state that such deposition of a chalcogenide on a mesoporous carbon support may result in

a product with properties and performance going beyond a simple addition. Whether it is justified to discuss such interactions presumably causing these effects in terms of interfacial conjugation [55] seems to be another question.

3.2. Intrinsically conducting polymers

A second class of materials considered both for use in battery and supercapacitor electrodes encloses intrinsically conducting polymers (ICPs) [74–78]. Starting with the suggestion of the charge storage possibilities of ICPs possibly useful in electrodes for secondary batteries (which unfortunately was not crowned with a commercial success until today), these materials have also been suggested as electrode materials for supercapacitors [78]. Chances and challenges regarding the properties and performance of the materials are the same in both applications, and ways to establish the desired long-term stability during multiple charge and discharge processes are even more mandatory in the case of supercapacitor applications. Accordingly, in the latter case, the architecture of the ICP and suitable morphology, possibly improved by combination with a matching second component, deserve increased attention. Suggestions that ICPs will fill the gap between batteries and supercapacitors may be a bit too optimistic [78].

A class of materials attracting growing attention for both battery and supercapacitor electrodes are organic materials beyond ICPs. The recent surge in interest is presumably related to the general interest in materials with practically unlimited resources (which is a growing concern with many current battery materials), to the possibility of rather simple handling of used/worn out materials not requiring the specific procedures required for handling heavy metal-containing batteries and devices, to the simple redox reactions not encumbered by intercalation or other possibly slow reaction steps, and to mostly smaller energy usage in preparing these materials under environmentally acceptable conditions (for a broader overview with regard to metal-ion batteries see the overview by Lu et al. [79], for some rather general considerations on organic materials in batteries see the report by Huang et al. [80]). Changes in material properties can be afforded in most cases using the tools of well-established organic synthesis [81]. Finally, these materials may provide a bridge to the use of renewable materials like lignin [82] or other materials derived from natural resources [88–90]. Lastly, these materials may enable or at least simplify the construction of flexible and even stretchable battery and supercapacitor devices.

3.3. Composites and further combinations

As already discussed above, for the case of combinations of chalcogenides and carbon materials, combinations of ICPs and some carbon-based components were examined. Several reviews are available [91–96]. Although not always addressed specifically, there are several roles for both the ICP and the carbon component. The ICP will predominantly act as the charge storage material. As a polymer, it might also act as a binder, caring for both cohesion between the ICP in its particular shape and the carbon in the electrode mass and adhesion of the composite or hybrid to the current collector. The carbon provides a mechanical support in case the ICP has been deposited on it; it provides mechanical integrity when the ICP shows shape change

because of, e.g., swelling and shrinking; and it guarantees sufficient electronic conductivity even when the ICP is in its poorly conducting neutral state.

Finally, combinations of metal chalcogenides and ICPs have attracted attention as active masses, mostly for supercapacitors; a review has been provided by Fu et al. [97].

Supercapacitors as well as battery electrodes frequently contain auxiliary materials. In addition to the current collector almost always also acting as a mechanical support (metal foils, carbon, or graphite paper), a binder and a conductive additive (acetylene black or other carbonaceous materials) are present. In both applications, materials are needed: without a binder, coherence between the particles of the active mass as well as their adherence to the current collector would be insufficient for keeping the electrode in shape and stable during cycling. Without added conducting material, the internal ohmic resistance (sometimes confused with the charge transfer resistance R_{ct} or assumed to be almost equivalent to it) of the active mass would be too high to support the high current operation requested both for supercapacitor and high-power battery electrodes. To get rid of the latter additive, mixed metal chalcogenides with higher intrinsic electronic conductivity are attractive when compared with, e.g., the wide bandgap semiconductor forms of MnO_2. In many reported studies, this potential advantage is hardly explored; instead, the almost standard additions of acetylene black, mostly around 10 %wt. indicate that no optimization was tried.

To get rid of the conventionally electrochemically dead binder, electrode preparation procedures wherein the active mass is directly deposited on the current collector (e.g., deposition of metal oxides and hydroxides by chemical or electrochemical procedures from the respective ionic solutions on metal foils, as suggested by the Lokhande group [98]) may provide an option at least for low loadings of active mass. These were identified as being particularly favorable for high mass utilization [99]. Electrochemically active binders based on ICPs have been suggested by Kondratiev and Holze [100]. A review by Holze and Kondratiev is available [77]. Another option is a polystyrene-based binder with redox-active modifications [101]. The possibility of using an ICP both as a redox-active storage material and as a binder when combined with a metal chalcogenide has hardly been explored so far because, in the majority of reported studies (a review by Fu et al. can be found [97]), the ICP has been polymerized chemically in the presence of the finely dispersed chalcogenide, yielding a powder material. To transfer this material into an electrode, a binder is needed. A procedure wherein electropolymerization in the presence of chalcogenide is performed appears to be feasible; it was examined before with promising results for nanocomposites in corrosion protection coatings [102].

4. Electrodes and their architectures

Based on the current response to a changing electrode potential in a CV experiment (or the electrode potential change during a galvanostatic charge/discharge (GCD) experiment), two types of electrodes can be straightforwardly distinguished:

Battery-type electrode (also called redox electrode or Nernstian electrode [103]): The CV shows visible current (Faradaic) peaks associated with the redox transformations of the active material; the GCD curve shows steps or plateaus.

Because electrodes with very few notable exceptions (lithium metal electrodes) are highly porous with an associated large surface area and interfacial capacitance, they will always have significant capacitive currents added to the Faradaic current, yielding CVs that look different from the textbook example of a CV obtained with a compact and smooth metal sheet in an electrolyte solution with a dissolved redox system.

Capacitive electrode[4]: The CV is flat; the GCD curve shows a triangular shape. Only ion accumulation and dispersion (possibly including ad-/desorption) proceed during charging and discharging (see **Figure 2**). Whether adsorptive interaction between the electrode surface and ions close to it happens or not may be of academic interest. Details of partial charge transfer and electrosorption valency are discussed [104]. A flat CV and a triangular GCD curve may also be obtained with an electrode showing pseudocapacitive behavior (see **Figure 4**). But the currents are larger by orders of magnitude than those found with comparable (in terms of EASA and dimension) simply capacitive electrodes; the larger currents cannot be due only to ion accumulation and dispersion but are due to mostly superficial redox processes that lack the peak in a CV (and the plateau in the GCD) for reasons related to materials and species properties discussed elsewhere [26]. Basically, again, a combination of Faradaic and non-Faradaic processes, like in # 1, happens, but this time the current vs. potential relationship is utterly different from the Nernstian case. This electrode may also be called a pseudocapacitive electrode.

Sometimes current responses, more specifically the shape of the recorded curves and diagrams, appearing to be somewhere between types 1 and 2, have been generously called capacitive or pseudocapacitive; this only causes confusion and does not help in understanding the underlying phenomena. Details of such curves have been amply displayed and extensively deplored elsewhere [105] without providing a deeper understanding of the underlying phenomena. Because of the great interest in having electrodes with both high charge storage and current-generating capability as outlined above and to understand relationships between structure, morphology, architecture, and performance, there have been frequent attempts to separate the Faradaic and the capacitive (i.e., non-Faradaic) responses (fractions of current flowing in response to the changing electrode potential) of an electrode in a CV, following a line of reasoning briefly reviewed elsewhere [3]. For further examples, see [106,107].

In a particularly popular and frequently encountered attempt, consideration starts at the power law relationship presented above Equation (7).

As stated, with $b = 1$, the current behaves capacitive-like. In a CV, further dependencies of current on scan rate can be observed. A case of particular interest is with $b = ½$. This is observed for the peak current in a cyclic voltammogram, both in cases where charge transfer and diffusion are limiting [108]. Assuming that the current response of an electrode can only be due to capacitive and faradaic contributions, it has been assumed

$$I = a \cdot v + c \cdot v^{1/2} \quad (16)$$

Such formally additive behavior was indicated first by Liu et al. [109] in a study of Mo_xN-electrodes. In a further stretch, it was assumed that this must be valid at all electrode potentials (although Equation (16) (the Randles-Ševčik equation simplified for the present discussion) was explicitly derived only for the peak current in a CV!). Rearrangement yields

$$I/v^{1/2} = a \cdot v^{1/2} + c \quad (17)$$

Plotting $I/v^{1/2}$ vs. $v^{1/2}$ yields slope a and intercept c. Liu et al. very logically concluded that the observed current must be subject to mixed control, i.e., caused by double layer charging as the capacitive process and some Faradaic reactions not further specified. Subsequently, this statement has developed an astonishing life of its own. It has been argued, presumably starting with a report by Lindström et al. [110], wherein the exponent in the power law equation (16) was observed to deviate from both 1 and ½ considerably while being close to unity in an electrode potential region where hardly any Faradaic reaction could be expected. This region of electrode potential (an example can be seen above in **Figure 4**) was called, for good reason, for decades a double layer region. Subsequent authors (a brief overview has been provided by Ge et al. [3]) have assumed instead that there can be only 1 and ½, with a and c being the adjustable parameters describing the Faradaic and the capacitive or pseudocapacitive parts of the current response. Evaluation of recorded CV data frequently resulted in displays of CVs showing major parts of the current (and charge) as being due to pseudocapacitive processes (some authors even simplified matters further, calling it the capacitive part). If this rather artificial separation makes any sense at all, it should suggest the conclusion that certain materials show higher fractions of the current response without being subject to diffusion limitation. For a material intended for a supercapacitor or a high-power battery, this is certainly a good outcome, but the same would have been obtained without all this rather diffuse reasoning by simply inspecting rate capability plots (capacitance vs. current density) showing a more constant capacitance or storage capability with a growing current density for a more suitable and structurally optimized material. Anyway, the above reasoning has been identified as lacking a scientific foundation [111].

The starting point of this reasoning hints at a development that again resembles a merger in the meaning of this report: to combine properties typical of a battery electrode and of a supercapacitor electrode.

The desire to obtain said separation for a single material, hopefully having significant amounts of both properties, whether it is of scientific and/or technological interest and relevance, appears to be a completely separate question that did not stop there. Various methods to obtain such separation have been compared; an example has been described by Forghani and Donne [112]. Three methods were compared (actually two, because two of the three methods are based on the same CV data, taking the I vs. v relationship (see above) and the integrated charge from a CV as separate methods) and resulted in the conclusion that the third method, named step potential electrochemical spectroscopy (SPECS) [113], presents the “most rigorous approach”. Given the fact that the current response after every electrode potential step was fitted using five adjustable parameters, this might not be too surprising. Somewhat surprisingly, electrochemical impedance measurements were not taken into consideration. This method, widely accessible with common instrumentation, also provides access to the interfacial (double layer) capacitance and the “capacitance” assigned to the redox process (the pseudocapacitance) [3,106,107].

Electrodes for both battery and supercapacitor applications are constructed with respect to performance (charge storage and current generation capability) and mass utilization [98]. Quite obviously, with a supercapacitor electrode, mostly the surface

and perhaps a few topmost layers are utilized in the electrode process, whereas in a battery electrode, in the ideal case, the whole volume up to the current collector is utilized in this reaction. Consequently, for the former application, a thin electrode will be preferred (because the bulk volume underneath the top layer will hardly be used, in particular in high-current applications), whereas for a battery electrode, a thicker volume with a smaller fraction of auxiliary material like a current collector is preferred. The transition from the former electrode (which has been called high power) to the latter (which has been called imprecisely high energy) is a continuous one, as depicted in the following **Figure 6**.

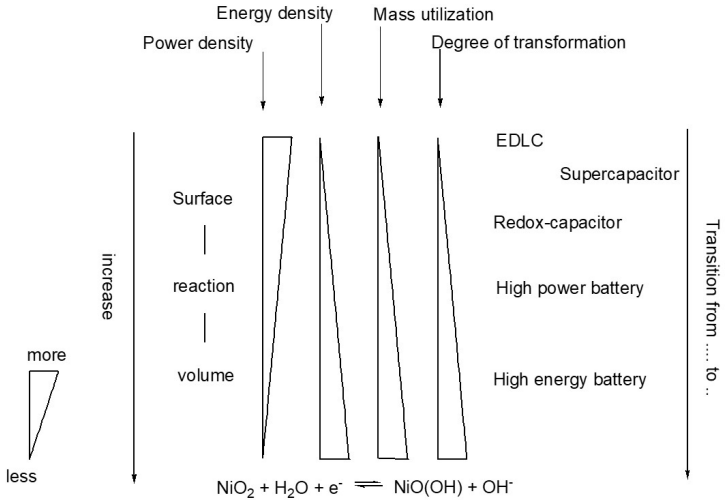

Figure 6. Transition from battery to supercapacitor electrode on the material and electrode design level.

Taking just this illustration, a supercapacitor electrode can be described as an extreme version of a high-power battery electrode. This "transition" was already addressed by Conway [43]. In **Figure 6**, the mode of energy storage, either by charge separation or by redox reaction, is missing because there is no conceivable continuum from charge separation to a redox reaction as proposed elsewhere [114]. Certainly, partial charge transfer can be misunderstood as a hint towards such a continuum, but close examination easily reveals that adsorption (most likely chemisorption) may include sharing charge between substrate and adsorbate, but in battery electrodes, no partial charge transfer happens.

Some further aspects and criteria can be added. A typical commercial example is Li-$SOCl_2$ primary batteries offered with a spirally wound electrode arrangement as a high-power battery and with a solid porous carbon core as the positive electrode and a comparably thicker lithium foil around it as the negative electrode in the high-energy version. Quite obviously, a cell and implicitly the employed electrodes meet both expectations: High energy and power are inherently impossible. Although scientifically not sound, studies of the relative fractions of capacitive and Faradaic currents addressed above have possibly contributed to the growing attention paid to optimized electrode structures and to material combinations enabling at least a closer approach to that elusive goal. An electrode material approaching this goal should have a large EASA, and this must be easily accessible for electrolyte solutions and electrolyte ions. To support high current, the material itself must provide high

electronic conductance, and the pores must not be too narrow to keep ionic conductance at a sufficiently high level. At this surface and very near it, a sufficient amount of battery-electrode material must be located to provide charge storage capability, finally resulting in the energy density of the complete cell. This description looks like a rather abstract wish list, but there is a simple test for the obtained achievement: Rate capability. A material successfully designed along the indicated lines of reasoning should provide excellent rate capability, even at high currents, and of course, only for short periods of time, the electrode potential for both electrodes should change hardly. The fundamental feasibility of this approach is illustrated by the lead acid battery and its remarkable power capability under discharge conditions (a researcher following the misleading line of reasoning briefly discussed above would assign a huge fraction of capacitive current to a lead acid battery during discharge). Unfortunately, during charging, this behavior was not found.

An approach working both during charge and discharge and reducing, in addition, the inventory of expensive electrode materials is the combination of RuO_2 nanoparticles and carbon materials with the metal oxide anchored on a foam of graphene and carbon nanotubes (CNTs) [115]. The obtained composite is stable, and the production is rather simple. The observed high energy density is based both on the sufficiently large surface area and the redox storage provided by the metal oxide. High rate capability is supported by the highly electron-conducting scaffold of the graphene foam with the attached CNTs. Unfortunately, no comparison with the state-of-the-art energy density of secondary batteries was provided, enabling a direct appreciation of the success of this approach.

The previous considerations can be assembled in a schematic approach (**Figure 7**) to an optimized electrode architecture valid both for battery and supercapacitor electrodes.

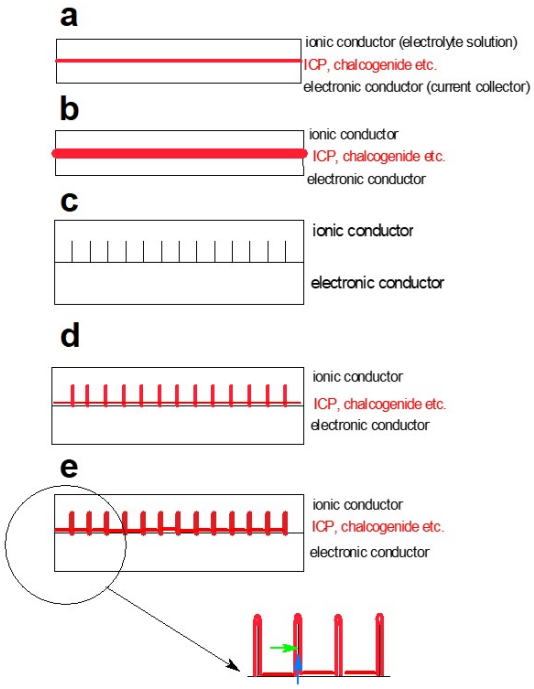

Figure 7. Sketches of electrode architectures.

Black: electronically conducting support; red: Active mass with ion (→) and electron (→) pathway.

A thin electrode (**Figure 7a**) may not provide enough active mass; a thicker, non-porous electrode (**Figure 7b**) has longer electronic pathways when the electrode reaction still takes place at the ICP/solution interface. An electronically conducting 3D support (**Figure 7c**) provides a larger interfacial area to be covered subsequently with active mass (**Figure 7d),** but the actual coating must finely balance electronic and ionic conduction pathways and their respective lengths and contributions to ohmic resistance (**Figure 7e** and insert). 3D-supports (instead of smooth metal foils) can be metal grids, foams or meshes, carbon or graphite paper, or carbon structures prepared by the pyrolysis of natural materials from biological sources. Further structuring on an even finer level can be afforded by controlled and directed ICP deposition. These considerations also apply to materials and electrodes for supercapacitors, and this has been highlighted before by Fu et al. [97].

5. Devices and cells

On the device or cell level, the merger proceeds in various ways. Electrodes containing both components acting via Faradaic reaction, like a conventional battery electrode, and acting via, e.g., a suitably large EASA [46], like a supercapacitor electrode, have already been discussed in the previous section. In addition, combinations of electrodes from both families will be the focus of this section. As already addressed above, the terminology appears to be confusing. A suggested distinction and proposed interpretation of the meaning of the terms “asymmetric” and “hybrid” have been reported [48]: An asymmetric device contains two electrodes of different materials but with the same storage mechanism, like a supercapacitor with different carbon electrodes, whereas a hybrid device contains electrodes with different modes of storage, like a negative activated carbon electrode (capacitive) and a metal chalcogenide positive electrode showing pseudocapacitive or battery electrode behavior. This distinction has been reaffirmed with numerous examples more recently [116].

The well-established limitations and flaws of the negative (lead) electrode in the lead-acid battery [117] have encouraged the search for alternative negative electrodes. Carbon-based materials were suggested, and the device also containing a conventional positive PbO_2-electrode has been called a hybrid ultracapacitor [27]. The device just outlined can be called a capacitor (the rather confusing terminology of commercial devices[1] will not be followed here) or, provided its capacitance is large enough, a supercapacitor because the negative carbon electrode shows behavior typical of an EDLC-supercapacitor material. But if the intercalation of electrolyte ions proceeds, this may not be true anymore. The positive lead dioxide electrode behaves even less like a supercapacitor electrode; it shows battery electrode behavior [118]. Calling the device a battery because of this misses possibly a central property of the negative electrode. Attaching the term hybrid might help, but terms like pseudocapacitor (which even lacks basic logic) do not.

Starting at the same imperfection of the negative lead electrode, a device that might systematically be called a double hybrid—the authors prefer the term ultra-battery—with a positive PbO_2-electrode and a negative one combining a lead and a carbon-based electrode into one has been proposed [119]. Simply connecting the

materials mechanically will not be enough. The electrode potential is now fixed (pinned) by the Pb(0)/Pb(II)-redox couple. As noticed, current vs. electrode potential relationships for the carbon electrode suggest a situation wherein during discharge, most of the current will initially be contributed by the lead electrode, with the carbon electrode contributing only towards the end [119]. During charging, things are slightly more as desired; initially, most of the current goes into the carbon electrode, but now, towards the end of charging, the negative carbon electrode will generate excessive hydrogen gas. Both situations are undesirable, but various modifications to electrode design and cell inventory nevertheless resulted in cell performance much better than that of state-of-the-art lead-acid batteries [119].

In an attempt to bring some order into the terminological confusion, Akinwolemiwa et al. tried to establish an extended terminology, including terms like negatrode and supercapattery of the second kind, etc. [35,13,103,120–123].

Instead of creating further terms and possibly adding confusion, some established terms and possible combinations are shown in **Figure 8**:

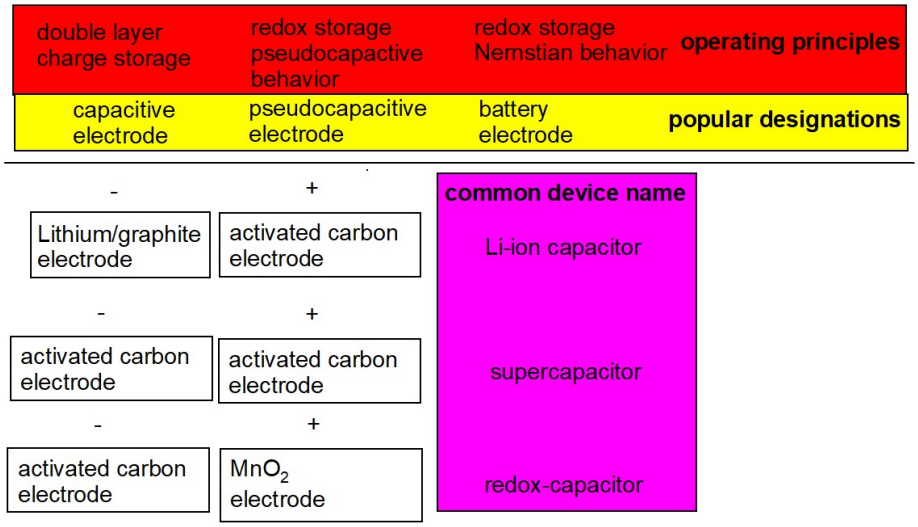

Figure 8. Possible combinations of electrodes and operating principles.

The term “Faradaic” is used to characterize a process involving charge transfer (different from non-Faradaic, i.e., capacitive processes); the term “Nernstian” is applied to a Faradaic process, showing the typical peaks observed in cyclic voltammograms. In this terminology, electrode processes showing a pseudocapacitive current response to a changing electrode potential may be called Faradaic and non-Nernstian, but as already suggested above and elsewhere [26], the creation of further names and terms as well as attempts to use terminology that is unnecessarily complicated appear to be of limited value only. For practical applications, it is of considerably higher interest to know how the charge/discharge behavior of a cell in terms of cell voltage vs. state of charge depends on the particular electrode combination. In the case of a capacitive electrode, there is no electrode reaction controlling the electrode potential; instead, the electrode potential linearly depends on the state of charge. In the case of a pseudocapacitive material, the situation is very similar, but the window of observed electrode potentials is controlled by the actual electrode reaction [26]. With a battery electrode, the actual electrode potential is

controlled by the activities of the participating reactants; basically, the potential will stay rather constant during the charge/discharge as long as a specific reaction proceeds. Only when the reaction switches to another one may the electrode potential show a noticeable step-like change (like in the case of the MnO_2-electrode in an alkaline battery, wherein the transformation of MnO_2 proceeds in two different reactions associated with significantly different electrode potentials and correspondingly different cell voltages). Accordingly, the various combinations sketched in **Figure 8** will show different charge/discharge curves, basically somewhere between the capacitor- and the battery-type. These two boundary cases are illustrated in **Figure 9**.

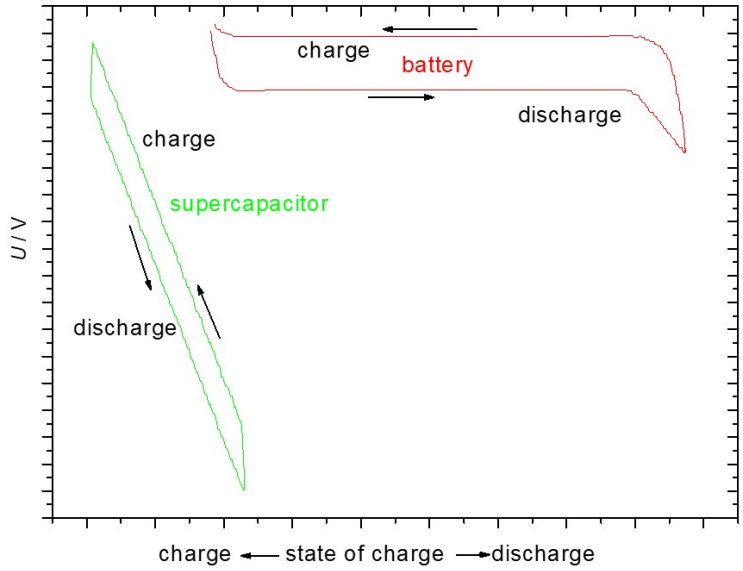

Figure 9. Simplified charge/discharge curves of a battery and a capacitor.

The actual shape of the curves will also depend on the matching of the storage capabilities of both electrodes.

Determination of performance data achieved for such devices and reporting with still missing or poorly defined standards enabling comparisons between more or less different systems was addressed frequently [3,15,116,124] with only limited success. Because the high cycling stability of supercapacitors, in particular the EDLC-type, is always stressed as a major advantage and a basic requisite for practical application devices placed between the traditional fields, whether hybrid or asymmetric, they should be examined with realistic parameters. Even when accepting the generally lower cycle numbers expected from batteries, a few hundred cycles observed with an electrode or even a complete system in this “in between” field is hardly useful.

Combinations of electrodes providing fast charge/discharge with limited storage capability with those showing larger storage capability but slower charge/discharge may look like a poor compromise because the power capability of the device will be limited by the electrode showing a smaller current capability, whereas energy storage is limited by the electrode having a lower charge storage capability. In large-scale and long-term energy storage (where most electrochemical energy conversion and storage systems are at a price disadvantage anyway), these concerns may be valid. But in applications where only short-term storage is required combined with, e.g., long-term stability, like in a power supply for an elevator where a supercapacitor may reduce the

peak power demand from 33 kW to 2.5 kW [125], this is no bad compromise anymore. Even the initial example of the carbon-lead dioxide system enjoys this benefit of high stability and fast charging because of the "fast" negative supercapacitor electrode and the "fast" positive electrode, which enable fast charging even during short periods of bright sunshine.

6. Conclusions

A growing number of electrode materials and architectures are encountered both in secondary batteries and redox supercapacitors. The operating principles, i.e., redox reactions, of such batteries and supercapacitors are basically the same; the major difference is the preferred location of electrode processes at the electrochemical interface in the latter and all over the electrode volume in the former. Consequently, scientists active in research and development in both fields should always look at the other side for inspiration and solutions. This applies in particular to the development of supercapacitor components aiming at higher energy densities, possibly to a lesser extent to high-power batteries. Obviously, progress achieved here can possibly be translated into improvements in batteries, possibly even for those who seem to be "adult" in terms of engineering.

Funding: Preparation of this communication has been supported in various ways by National Key R & D Program of China (2021YFB2400400), it includes results obtained within research projects at St. Petersburg State University supported by grant № 26455158 and grant № 70037840. Preparation of this communication has been supported in various ways by the Alexander von Humboldt-Foundation, Deutscher Akademischer Austauschdienst, Fonds der Chemischen Industrie, Deutsche Forschungsgemeinschaft, National Basic Research Program of China, and Natural Science Foundation of China (Grant # 51425301).

Conflict of interest: The authors declare no conflict of interest.

Notes

1. For supercapacitors no unified and universally accepted nomenclature has been established as of the time of writing. The terms supercap or supercapacitor™ (as well as ultracap/ultracapacitor) appear to lack a proper and generally ac¬cepted definition. At first glance it appears sufficient to assume, that capacitors based on the capacitive prop¬erties of the electrochemical double layer instead of a dielectric material like Al2O3 or Ta2O5 showing huge capacities are correctly called superca¬pacitors. Temporarily the latter term was trademarked (from August 1978 on) to NEC Corpo¬ration, currently this protection has apparently expired. The acronym SC seems to be too short to enable immediate identification. Acronyms like ES for electrochemical supercapacitor or FS for Faradaic supercapacitor do nothing beyond enlarging the confusion. Recently the device wherein purely electrostatic charge storage in the double layer is operative has been frequently called EDLC (electrochemical double layer capacitor). Thus it appears to be reasonable to call devices with high volumetric capacitance (in F), wherein charge storage is based both on electrostatic charge separation (like in an EDLC) and on Faradaic redox processes (including pseudocapacitive and redox storage) supercapacitors. Because of the combination of these fundamentally different charge stor¬age mechanisms these devices are also sometimes called hybrids – adding further to the confusion. In the present report supercapacitors are such hybrid devices, the term ultracapacitor is not used at all. Its use to designate only those devices employing pseudocapacitances seems to be a loosing proposition [A. Burke, J. Power

Sources 91, 37 (2000).]. The statement, that B. Conway coined the term supercapacitor in 1991 is apparently erroneous. The rich collection of terms – some of them presumably protected by trademarks – does not help really: APowerCap, Best¬Cap, BoostCap, CAP-XX, DLCAP, EneCapTen, EVerCAP, DynaCap, Faradcap, GreenCap, Goldcap, HY-CAP, Kapton capacitor, Super capacitor, SuperCap, PAS Capacitor, PowerStor, PseudoCap etc. Adding to this collection by defining the obvious like electrochemical supercapacitor with ES (all known supercapacitors are electrochemical devices, no others are known) or to interpret the well-known acronym EDLC by calling it an electrostatic super¬capa-citor as done by Wang et al.[6] does not help, either.

2. Recently the term pseudocapacitor has been used with growing frequency. As discussed before in detail this term is as wrong as the term pseudocapacitive for designating a material which does not behave pseudocapacitive at all [26, 48]. In short: From a linguistic and systematic point of view a pseudocapacitor must be a device behaving like a capacitor without being a capacitor. When accepting the certainly correct statement that a material like RuO2 may show a capacitive-like response in a CV without being a purely double layer capacitor electrode material the term pseudocapacitor may be perhaps applied to a very narrow class of supercapacitors employing only such materials. But presumably misuse of the term would result in the same chaos currently observed with the term pseudocapacitive. Provisionally in this report the term redox-capacitor is used.
3. The term dual-ion battery DIB stresses the fact, that two (both in case of a binary electrolyte) ions of the electrolyte participate in charge storage different from the rocking-chair principle of e.g. the lithium ion battery wherein only one ion participates. The acronyms DGB and DCB refer instead to the electrode material (G graphite, C carbon) missing the dual ion feature. DIC as dual ion cell is slightly more general.
4. This as an extremely abbreviated notation. Of course the electrode itself is not capacitive, it is the electrode's behavior. This sounds like linguistic and possibly irrelevant hairsplitting, but the sometimes highly emotional, almost offensive discussion of this terminology suggests otherwise.

References

1. Wu Y, Holze R. Electrochemical Energy Conversion and Storage. VCH-WILEY; 2022.
2. Kurzweil P, Dietlmeier OK. Elektrochemische Speicher. Springer Vieweg; 2015.
3. Ge Y, Xie X, Roscher J, et al. How to measure and report the capacity of electrochemical double layers, supercapacitors, and their electrode materials. Journal of Solid State Electrochemistry. 2020; 24(11-12): 3215-3230. doi: 10.1007/s10008-020-04804-x
4. Becker HI. U.S. Patent US2800616, 23 July 1957.
5. Rightmire RA. U.S. Patent US3288641, 29 November 1966.
6. Wang G, Zhang L, Zhang J. A review of electrode materials for electrochemical supercapacitors. Chem Soc Rev. 2012; 41(2): 797-828. doi: 10.1039/c1cs15060j
7. Dubal DP, Wu Y, Holze R. Supercapacitors as fast storage systems for electric energy. Bunsen-Magazin. 2015; 17: 216-227.
8. Vangari M, Pryor T, Jiang L. Supercapacitors: Review of Materials and Fabrication Methods. Journal of Energy Engineering. 2013; 139: 72-92.
9. Vol'fkovich YM, Serdyuk TM. Electrochemical capacitors. Russian Journal of Electrochemistry. 2002; 38: 935-958.
10. Burke A. Ultracapacitors: Why, how, and where is the technology. Journal of Power Sources. 2000; 91: 37-50.
11. Shukla AK, Sampath S, Vijayamohanan K. Electrochemical supercapacitors: Energy storage beyond batteries. Current Science. 2000; 79: 1656-1661.
12. Guan L, Yu L, Chen GZ. Capacitive and non-capacitive faradaic charge storage. Electrochimica Acta. 2016; 206: 464-478. doi: 10.1016/j.electacta.2016.01.213
13. Dubal DP, Wu YP, Holze R. Supercapacitors: from the Leyden jar to electric busses. ChemTexts. 2016; 2(3). doi: 10.1007/s40828-016-0032-6
14. Conway BE. Electrochemical Supercapacitors: Scientific Fundamentals and Technological Applications. Springer; 1999.
15. Faggioli E, Rena P, Danel V, et al. Supercapacitors for the energy management of electric vehicles. Journal of Power Sources. 1999; 84: 261-269.

16. Nguyen T, Montemor MF. Redox active materials for metal compound based hybrid electrochemical energy storage: a perspective view. Applied Surface Science. 2017; 422: 492-497. doi: 10.1016/j.apsusc.2017.06.008
17. Baptista JM, Sagu JS, KG UW, et al. State-of-the-art materials for high power and high energy supercapacitors: Performance metrics and obstacles for the transition from lab to industrial scale – A critical approach. Chemical Engineering Journal. 2019; 374: 1153-1179. doi: 10.1016/j.cej.2019.05.207
18. Electrochemical Supercapacitors for Energy Storage and Delivery—Fundamentals and Applications. CRC Press; 2013.
19. Electrochemical Capacitors. In: Materials Research Foundations. Materials Research Forum LLC; 2018.
20. Stevic Z. Supercapacitor Design and Applications. ExLi4EvA; 2016.
21. Beguin F, Frackowiak E. Supercapacitors. Wiley-VCH; 2013.
22. Miller JM. Ultracapacitor Applications. The Institution of Engineering and Technology; 2011.
23. Wu Y, Holze R. Self-discharge in supercapacitors: Causes, effects and therapies: An overview. Electrochem Energy Technol. 2021; 7: 1-37.
24. Gür TM. Review of electrical energy storage technologies, materials and systems: challenges and prospects for large-scale grid storage. Energy & Environmental Science. 2018; 11: 2696-2767.
25. Frequently the term electrolyte meaning in most cases electrolyte solution is used. In: Solid electrolytes and ionic liquids are further options.
26. Holze R. From current peaks to waves and capacitive currents—on the origins of capacitor-like electrode behavior. Journal of Solid State Electrochemistry. 2016; 21(9): 2601-2607. doi: 10.1007/s10008-016-3483-1
27. Banerjee A, Ramasesha SK, Shukla AK. A photovoltaic stand-alone lighting system with polymeric-silica-gel-electrolyte-based substrate-integrated lead-carbon hybrid ultracapacitors. Electrochemical Energy Technology. 2015; 1(1). doi: 10.1515/eetech-2015-0001
28. Dubal DP, Ayyad O, Ruiz V, et al. Hybrid energy storage: the merging of battery and supercapacitor chemistries. Chemical Society Reviews. 2015; 44(7): 1777-1790. doi: 10.1039/c4cs00266k
29. Zuo W, Li R, Zhou C, et al. Battery-Supercapacitor Hybrid Devices: Recent Progress and Future Prospects. Advanced Science. 2017; 4(7). doi: 10.1002/advs.201600539
30. Krishnan SG, Harilal M, Pal B, et al. Improving the symmetry of asymmetric supercapacitors using battery-type positive electrodes and activated carbon negative electrodes by mass and charge balance. Journal of Electroanalytical Chemistry. 2017; 805: 126-132. doi: 10.1016/j.jelechem.2017.10.029
31. Cericola D, Kötz R. Hybridization of rechargeable batteries and electrochemical capacitors: Principles and limits. Electrochimica Acta. 2012; 72: 1-17. doi: 10.1016/j.electacta.2012.03.151
32. Xie J, Yang P, Wang Y, et al. Puzzles and confusions in supercapacitor and battery: Theory and solutions. Journal of Power Sources. 2018; 401: 213-223. doi: 10.1016/j.jpowsour.2018.08.090
33. Yu L, Chen GZ. Redox electrode materials for supercapatteries. Journal of Power Sources. 2016; 326: 604-612. doi: 10.1016/j.jpowsour.2016.04.095
34. Akinwolemiwa B, Peng C, Chen GZ. Redox Electrolytes in Supercapacitors. Journal of The Electrochemical Society. 2015; 162(5): A5054-A5059. doi: 10.1149/2.0111505jes
35. Chen GZ. Supercapacitor and supercapattery as emerging electrochemical energy stores. International Materials Reviews. 2016; 62(4): 173-202. doi: 10.1080/09506608.2016.1240914
36. Conway BE. Electrochemical Capacitors. The Electrochemical Society Inc; 1996.
37. Conway BE, Birss V, Wojtowicz J. The role and utilization of pseudocapacitance for energy storage by supercapacitors. Journal of Power Sources. 1997; 66: 1-14.
38. Simon P, Gogotsi Y, Dunn B. Where Do Batteries End and Supercapacitors Begin? Science. 2014; 343(6176): 1210-1211. doi: 10.1126/science.1249625
39. Gogotsi Y, Penner RM. Energy Storage in Nanomaterials – Capacitive, Pseudocapacitive, or Battery-like? ACS Nano. 2018; 12(3): 2081-2083. doi: 10.1021/acsnano.8b01914
40. Kim ND, Buchholz DB, Casillas G, et al. Hierarchical Design for Fabricating Cost-Effective High Performance Supercapacitors. Advanced Functional Materials. 2014; 24(26): 4186-4194. doi: 10.1002/adfm.201304130
41. Holze R. Landolt-Börnstein, Numerical Data and Functional Relationships in Science and Technology, New Series, Group IV: Physical Chemistry. Springer-Verlag; 2007.

42. Conway BE, Gileadi E. Kinetic theory of pseudo-capacitance and electrode reactions at appreciable surface coverage. Transactions of the Faraday Society. 1962; 58: 2493. doi: 10.1039/tf9625802493
43. Conway BE. Transition from "Supercapacitor" to "Battery" Behavior in Electrochemical Energy Storage. Journal of The Electrochemical Society. 1991; 138(6): 1539-1548. doi: 10.1149/1.2085829
44. Dubal DP, Holze R. Synthesis, properties, and performance of nanostructured metal oxides for supercapacitors. Pure and Applied Chemistry. 2014; 86(5): 611-632. doi: 10.1515/pac-2013-1021
45. Dubal DP, Chodankar NR, Gomez-Romero P, et al. Fundamentals of Binary Metal Oxide–Based Supercapacitors. In: Dubal DP, Gomez-Romero P (editors). Metal Oxides in Supercapacitors. Elsevier; 2017. pp. 79-98. doi: 10.1016/b978-0-12-810464-4.00004-8
46. Xie X, Holze R. Electrode Kinetic Data: Geometric vs. Real Surface Area. Batteries. 2022; 8(10): 146. doi: 10.3390/batteries8100146
47. Xie X, Holze R. Meaning and Determination of Electrode Surface Area. Available online: https://encyclopedia.pub/entry/41569 (accessed on 20 November 2023).
48. Brousse T, Bélanger D, Long JW. To Be or Not To Be Pseudocapacitive? Journal of The Electrochemical Society. 2015; 162(5): A5185-A5189. doi: 10.1149/2.0201505jes
49. Jiang Y, Liu J. Definitions of Pseudocapacitive Materials: A Brief Review. Energy & Environmental Materials. 2019; 2(1): 30-37. doi: 10.1002/eem2.12028
50. Sarangapani S, Tilak BV, Chen CP. Materials for Electrochemical Capacitors: Theoretical and Experimental Constraints. Journal of the Electrochemical Society. 1996; 143(11). doi: 10.1149/1.1837291
51. Sarangapani S, Tilak BV, Chen C -P. Materials for Electrochemical Capacitors: Theoretical and Experimental Constraints. Journal of The Electrochemical Society. 1996; 143(11): 3791-3799. doi: 10.1149/1.1837291
52. Grahame DC. Properties of the Electrical Double Layer at a Mercury Surface. I. Methods of Measurement and Interpretation of Results. Journal of the American Chemical Society. 1941; 63(5): 1207-1215. doi: 10.1021/ja01850a014
53. Burke LD, Murphy OJ. Cyclic voltammetry as a technique for determining the surface area of RuO2 electrodes. Journal of Electroanalytical Chemistry. 1979; 96: 19-27.
54. Ardizzone S, Fregonara G, Trasatti S. "Inner" and "outer" active surface of RuO_2 electrodes. Electrochimica Acta. 1990; 35: 263-269.
55. Chen GZ. Understanding supercapacitors based on nano-hybrid materials with interfacial conjugation. Progress in Natural Science: Materials International. 2013; 23(3): 245-255. doi: 10.1016/j.pnsc.2013.04.001
56. Reddy TB. Linden's Handbook of Batteries. MacGraw-Hill; 2011.
57. Daniel C, Besenhard JO. Handbook of Battery Materials. WILEY-VCH; 2011.
58. Augustyn V, Simon P, Dunn B. Pseudocapacitive oxide materials for high-rate electrochemical energy storage. Energy & Environmental Science. 2014; 7(5): 1597. doi: 10.1039/c3ee44164d
59. Tian ZW, Dong QF, Zheng MS, Lin ZG. U.S. Patent US20090190286, 30 July 2009.
60. Holze R. Supercapacitors as energy storage (German). Nachr Chem. 2017; 65: 333-338.
61. Beck F, Euler KJ. Electrochemical energy storage (German). VDE-Verlag GmbH; 1984.
62. Lou S, Cheng X, Gao J, et al. Pseudocapacitive Li^+ intercalation in porous $Ti_2Nb_{10}O_{29}$ nanospheres enables ultra-fast lithium storage. Energy Storage Materials. 2018; 11: 57-66. doi: 10.1016/j.ensm.2017.09.012
63. Volkov AI, Dubal DP, Holze R, Wu Y. Mixed metal chalcogenides as active masses for supercapacitor electrodes – A review. Advanced Energy Materials.
64. Placke T, Heckmann A, Schmuch R, et al. Perspective on Performance, Cost, and Technical Challenges for Practical Dual-Ion Batteries. Joule. 2018; 2(12): 2528-2550. doi: 10.1016/j.joule.2018.09.003
65. Placke T, Fromm O, Lux SF, et al. Reversible Intercalation of Bis(trifluoromethanesulfonyl)imide Anions from an Ionic Liquid Electrolyte into Graphite for High Performance Dual-Ion Cells. Journal of The Electrochemical Society. 2012; 159(11): A1755-A1765. doi: 10.1149/2.011211jes
66. Heidrich B, Heckmann A, Beltrop K, et al. Unravelling charge/discharge and capacity fading mechanisms in dual-graphite battery cells using an electron inventory model. Energy Storage Materials. 2019; 21: 414-426. doi: 10.1016/j.ensm.2019.05.031
67. Heckmann A, Thienenkamp J, Beltrop K, et al. Towards high-performance dual-graphite batteries using highly concentrated organic electrolytes. Electrochimica Acta. 2018; 260: 514-525. doi: 10.1016/j.electacta.2017.12.099

68. Kravchyk KV, Kovalenko MV. Rechargeable Dual-Ion Batteries with Graphite as a Cathode: Key Challenges and Opportunities. Advanced Energy Materials. 2019; 9(35). doi: 10.1002/aenm.201901749
69. Walter M, Kovalenko MV, Kravchyk KV. Challenges and benefits of post-lithium-ion batteries. New Journal of Chemistry. 2020; 44(5): 1677-1683. doi: 10.1039/c9nj05682c
70. Sui Y, Liu C, Masse RC, et al. Dual-ion batteries: The emerging alternative rechargeable batteries. Energy Storage Materials. 2020; 25: 1-32. doi: 10.1016/j.ensm.2019.11.003
71. Wang X, Han X, Lim M, et al. Nickel Cobalt Oxide-Single Wall Carbon Nanotube Composite Material for Superior Cycling Stability and High-Performance Supercapacitor Application. The Journal of Physical Chemistry C. 2012; 116(23): 12448-12454. doi: 10.1021/jp3028353
72. Dubal DP, Chen X, Wu Y, Holze R. Conducting Polymers for Supercapacitors. In: Gupta RK (editor). Conducting Polymers for Advanced Energy Applications. CRC Press; 2021.
73. Borenstein A, Hanna O, Attias R, et al. Carbon-based composite materials for supercapacitor electrodes: a review. Journal of Materials Chemistry A. 2017; 5(25): 12653-12672. doi: 10.1039/c7ta00863e
74. Holze R. Composites and Copolymers Containing Redox-Active Molecules and Intrinsically Conducting Polymers as Active Masses for Supercapacitor Electrodes—An Introduction. Polymers. 2020; 12(8): 1835. doi: 10.3390/polym12081835
75. Holze R. Conjugated Molecules and Polymers in Secondary Batteries: A Perspective. Molecules. 2022; 27(2): 546. doi: 10.3390/molecules27020546
76. Kondratiev VV, Holze R. Intrinsically conducting polymers and their combinations with redox-active molecules for rechargeable battery electrodes: An update. Chemical Papers. 2021; 75(10): 4981-5007. doi: 10.1007/s11696-021-01529-7
77. Holze R, Wu YP. Intrinsically conducting polymers in electrochemical energy technology: Trends and progress. Electrochimica Acta. 2014; 122: 93-107. doi: 10.1016/j.electacta.2013.08.100
78. Fong KD, Wang T, Smoukov SK. Multidimensional performance optimization of conducting polymer-based supercapacitor electrodes. Sustainable Energy & Fuels. 2017; 1(9): 1857-1874. doi: 10.1039/c7se00339k
79. Lu Y, Zhang Q, Li L, et al. Design Strategies toward Enhancing the Performance of Organic Electrode Materials in Metal-Ion Batteries. Chem. 2018; 4(12): 2786-2813. doi: 10.1016/j.chempr.2018.09.005
80. Huang T, Long M, Xiao J, et al. Recent research on emerging organic electrode materials for energy storage. Energy Materials. 2022; 1(1): 100009. doi: 10.20517/energymater.2021.09
81. Jia X, Ge Y, Shao L, et al. Tunable Conducting Polymers: Toward Sustainable and Versatile Batteries. ACS Sustainable Chemistry & Engineering. 2019; 7(17): 14321-14340. doi: 10.1021/acssuschemeng.9b02315
82. Espinoza-Acosta JL, Torres-Chávez PI, Olmedo-Martínez JL, et al. Lignin in storage and renewable energy applications: A review. Journal of Energy Chemistry. 2018; 27(5): 1422-1438. doi: 10.1016/j.jechem.2018.02.015
83. Chaleawlert-umpon S, Berthold T, Wang X, et al. Kraft Lignin as Electrode Material for Sustainable Electrochemical Energy Storage. Advanced Materials Interfaces. 2017; 4(23). doi: 10.1002/admi.201700698
84. Lahiri A, Yang L, Höfft O, et al. Biodegradable Zn-ion battery with a lignin composite electrode and bio-ionic liquid based electrolyte: possible in situ energy generation by lignin electrocatalysis. Materials Advances. 2021; 2(8): 2676-2683. doi: 10.1039/d0ma00954g
85. Zhu J, Yan C, Zhang X, et al. A sustainable platform of lignin: From bioresources to materials and their applications in rechargeable batteries and supercapacitors. Progress in Energy and Combustion Science. 2020; 76: 100788. doi: 10.1016/j.pecs.2019.100788
86. Gnedenkov SV, Opra DP, Sinebryukhov SL, et al. Hydrolysis lignin-based organic electrode material for primary lithium batteries. Journal of Solid State Electrochemistry. 2013; 17(10): 2611-2621. doi: 10.1007/s10008-013-2136-x
87. Gnedenkov SV, Opra DP, Sinebryukhov SL, et al. Hydrolysis lignin: Electrochemical properties of the organic cathode material for primary lithium battery. Journal of Industrial and Engineering Chemistry. 2014; 20(3): 903-910. doi: 10.1016/j.jiec.2013.06.021
88. Gnedenkova SV, Opra DP, Zemnukhova LA, et al. Electrochemical performance of Klason lignin as a low-cost cathode-active material for primary lithium battery. Journal of Energy Chemistry. 2015; 24: 346-352.
89. Larcher D, Tarascon JM. Towards greener and more sustainable batteries for electrical energy storage. Nature Chemistry. 2014; 7(1): 19-29. doi: 10.1038/nchem.2085
90. Liu L, Solin N, Inganäs O. Bio Based Batteries. Advanced Energy Materials. 2021; 11(43). doi: 10.1002/aenm.202003713

91. Wang M, Xu YX. Design and construction of three-dimensional graphene/conducting polymer for supercapacitors. Chinese Chemical Letters. 2016; 27(8): 1437-1444. doi: 10.1016/j.cclet.2016.06.048
92. Wang J, Li X, Du X, et al. Polypyrrole composites with carbon materials for supercapacitors. Chemical Papers. 2016; 71(2): 293-316. doi: 10.1007/s11696-016-0048-9
93. Sebastian J, Samuel JM. Recent advances in the applications of substituted polyanilines and their blends and composites. Polymer Bulletin. 2019; 77(12): 6641-6669. doi: 10.1007/s00289-019-03081-7
94. Eftekhari A, Li L, Yang Y. Polyaniline supercapacitors. Journal of Power Sources. 2017; 347: 86-107. doi: 10.1016/j.jpowsour.2017.02.054
95. Huang Z, Li L, Wang Y, et al. Polyaniline/graphene nanocomposites towards high-performance supercapacitors: A review. Composites Communications. 2018; 8: 83-91. doi: 10.1016/j.coco.2017.11.005
96. Chauhan NPS, Mozafari M, Chundawat NS, et al. High-performance supercapacitors based on polyaniline–graphene nanocomposites: Some approaches, challenges and opportunities. Journal of Industrial and Engineering Chemistry. 2016; 36: 13-29. doi: 10.1016/j.jiec.2016.03.003
97. Fu L, Qu Q, Holze R, et al. Composites of metal oxides and intrinsically conducting polymers as supercapacitor electrode materials: the best of both worlds? Journal of Materials Chemistry A. 2019; 7(25): 14937-14970. doi: 10.1039/c8ta10587a
98. Dubal DP, Kim JG, Kim Y, et al. Supercapacitors Based on Flexible Substrates: An Overview. Energy Technology. 2014; 2(4): 325-341. doi: 10.1002/ente.201300144
99. Ge Y, Liu Z, Wu Y, et al. On the utilization of supercapacitor electrode materials. Electrochimica Acta. 2021; 366: 137390. doi: 10.1016/j.electacta.2020.137390
100. Kondratiev V, Holze R. Intrinsically Conducting Polymer Binders for Battery Electrodes. Encyclopedia. 2022; 2(4): 1753-1762. doi: 10.3390/encyclopedia2040120
101. Benoit C, Demeter D, Bélanger D, et al. A Redox-Active Binder for Electrochemical Capacitor Electrodes. Angewandte Chemie International Edition. 2016; 55(17): 5318-5321. doi: 10.1002/anie.201601395
102. Van Hoang H, Holze R. Electrochemical Synthesis of Polyaniline/Montmorillonite Nanocomposites and Their Characterization. Chemistry of Materials. 2006; 18(7): 1976-1980. doi: 10.1021/cm052707w
103. Akinwolemiwa B, Wei C, Chen GZ. Mechanisms and Designs of Asymmetrical Electrochemical Capacitors. Electrochimica Acta. 2017; 247: 344-357. doi: 10.1016/j.electacta.2017.06.088
104. Guidelli R, Schmickler W. Electrosorption Valency and Partial Charge Transfer. In: Conway BE, Vayenas CG, White RE, Gamboa-Adelco ME (editors). Modern Aspects of Electrochemistry. Springer; 2005. doi: 10.1007/0-387-25838-8_3
105. Ragoisha GA, Aniskevich YM. False capacitance of supercapacitors. Available online: https://arxiv.org/abs/1604.08154 (accessed on 12 January 2024).
106. Bandeira MCE, Holze R. Impedance measurements at thin polyaniline films – the influence of film morphology. Microchimica Acta. 2006; 156(1-2): 125-131. doi: 10.1007/s00604-006-0586-x
107. Ko JS, Lai CH, Long JW, et al. Differentiating Double-Layer, Psuedocapacitance, and Battery-like Mechanisms by Analyzing Impedance Measurements in Three Dimensions. ACS Applied Materials & Interfaces. 2020; 12(12): 14071-14078. doi: 10.1021/acsami.0c02020
108. Gosser Jr. DK. Cyclic Voltammetry. VCH; 1993.
109. Liu T -C., Pell WG, Conway BE, Roberson SL. Behavior of Molybdenum Nitrides as Materials for Electrochemical Capacitors: Comparison with Ruthenium Oxide. Journal of The Electrochemical Society. 1998; 145(6): 1882-1888. doi: 10.1149/1.1838571
110. Lindström H, Södergren S, Solbrand A, et al. Li^+ Ion Insertion in TiO_2 (Anatase). 2. Voltammetry on Nanoporous Films. The Journal of Physical Chemistry B. 1997; 101(39): 7717-7722. doi: 10.1021/jp970490q
111. Opitz M, Yue J, Wallauer J, et al. Mechanisms of Charge Storage in Nanoparticulate TiO_2 and $Li_4Ti_5O_{12}$ Anodes: New Insights from Scan rate-dependent Cyclic Voltammetry. Electrochimica Acta. 2015; 168: 125-132. doi: 10.1016/j.electacta.2015.03.186
112. Forghani M, Donne SW. Method Comparison for Deconvoluting Capacitive and Pseudo-Capacitive Contributions to Electrochemical Capacitor Electrode Behavior. Journal of The Electrochemical Society. 2018; 165(3): A664-A673. doi: 10.1149/2.0931803jes

113. Dupont MF, Donne SW. Faradaic and Non-Faradaic Contributions to the Power and Energy Characteristics of Electrolytic Manganese Dioxide for Electrochemical Capacitors. Journal of The Electrochemical Society. 2016; 163(6): A888-A897. doi: 10.1149/2.0401606jes
114. Hall PJ, Mirzaeian M, Fletcher SI, et al. Energy storage in electrochemical capacitors: designing functional materials to improve performance. Energy & Environmental Science. 2010; 3(9): 1238. doi: 10.1039/c0ee00004c
115. Wang W, Guo S, Lee I, et al. Hydrous Ruthenium Oxide Nanoparticles Anchored to Graphene and Carbon Nanotube Hybrid Foam for Supercapacitors. Scientific Reports. 2014; 4(1). doi: 10.1038/srep04452
116. Chodankar NR, Pham HD, Nanjundan AK, et al. True Meaning of Pseudocapacitors and Their Performance Metrics: Asymmetric versus Hybrid Supercapacitors. Small. 2020; 16(37). doi: 10.1002/smll.202002806
117. Pavlov D. Essentials of Lead-Acid Batteries. SAEST; 2006.
118. Yu N, Gao L. Electrodeposited PbO2 thin film on Ti electrode for application in hybrid supercapacitor. Electrochemistry Communications. 2009; 11(1): 220-222. doi: 10.1016/j.elecom.2008.11.013
119. Lam LT, Louey R. Development of ultra-battery for hybrid-electric vehicle applications. Journal of Power Sources. 2006; 158(2): 1140-1148. doi: 10.1016/j.jpowsour.2006.03.022
120. Akinwolemiwa B, Chen G. Fundamental Consideration for Electrochemical Engineering of Supercapattery. Journal of the Brazilian Chemical Society. 2018. doi: 10.21577/0103-5053.20180010
121. Yu L, Chen GZ. Supercapatteries as High-Performance Electrochemical Energy Storage Devices. Electrochemical Energy Reviews. 2020; 3(2): 271-285. doi: 10.1007/s41918-020-00063-6
122. Chen GZ. Supercapacitor and supercapattery as emerging electrochemical energy stores. International Materials Reviews. 2016; 62(4): 173-202. doi: 10.1080/09506608.2016.1240914
123. Chen GZ. Supercapattery: Merit merge of capacitive and Nernstian charge storage mechanisms. Current Opinion in Electrochemistry. 2020; 21: 358-367. doi: 10.1016/j.coelec.2020.04.002
124. Laheäär A, Przygocki P, Abbas Q, et al. Appropriate methods for evaluating the efficiency and capacitive behavior of different types of supercapacitors. Electrochemistry Communications. 2015; 60: 21-25. doi: 10.1016/j.elecom.2015.07.022
125. Rufer A, Barrade P. A supercapacitor-based energy-storage system for elevators with soft commutated interface. IEEE Transactions on Industry Applications. 2002; 38(5): 1151-1159. doi: 10.1109/tia.2002.803021

Energy Storage and Conversion 2024, 2(1), 436.
https://doi.org/10.59400/esc.v2i1.436

Review

Towards sustainable solar energy solutions: Harnessing supercapacitors in PV systems

Kerim Karabacak

Dept. of Electronics and Automation, Kutahya Technical Sciences Vocational School, Kutahya Dumlupinar University, Kutahya 43100, Turkey; kerim.karabacak@dpu.edu.tr

CITATION

Karabacak K. Towards sustainable solar energy solutions: Harnessing supercapacitors in PV systems. Energy Storage and Conversion. 2024; 2(1): 436. https://doi.org/10.59400/esc.v2i1.436

ARTICLE INFO

Received: 27 December 2023
Accepted: 26 February 2024
Available online: 12 March 2024

COPYRIGHT

Copyright © 2024 by author(s). *Energy Storage and Conversion* is published by Academic Publishing Pte. Ltd. This work is licensed under the Creative Commons Attribution (CC BY) license. https://creativecommons.org/licenses/by/4.0/

Abstract: The integration of supercapacitors in photovoltaic (PV) energy systems holds immense potential for enhancing energy storage, reliability, and efficiency. This article provides a comprehensive overview of recent advancements, challenges, and opportunities in the utilization of supercapacitors within PV systems. Fundamental principles of supercapacitor operation, including charge storage mechanisms and electrode materials, are discussed, highlighting their unique advantages such as high power density and rapid charge/discharge capabilities. Various integration strategies, including parallel and series configurations, as well as system-level control algorithms, are examined to optimize energy management and performance. Case studies and real-world examples demonstrate the effectiveness of integrated PV and supercapacitor systems across different applications and scales. According to the results of the research, 235 publications have been made on the subject in the last fifteen years, and the number of publications has doubled in the last five years. Additionally, future research directions focus on improving energy density, efficiency, and cost-effectiveness, as well as addressing challenges related to temperature sensitivity and system scalability. Overall, the integration of supercapacitors in PV systems offers promising solutions for advancing sustainable energy solutions and accelerating the transition towards a cleaner, greener future.

Keywords: energy storage; PV power; supercapacitors

1. Introduction

The global demand for sustainable energy solutions continues to escalate in response to environmental concerns and the imperative to mitigate climate change. Among renewable energy sources, solar power stands out as one of the most promising avenues for meeting this demand due to its abundant availability and minimal environmental impact. Photovoltaic (PV) systems, which convert sunlight directly into electricity, have witnessed significant advancements in efficiency and cost-effectiveness over the years, driving their widespread adoption in both residential and commercial settings. However, despite the remarkable progress made in PV technology, one of the persistent challenges facing solar energy systems is the intermittent nature of sunlight. Fluctuations in solar irradiance throughout the day and variations in weather conditions can lead to inconsistent energy output, limiting the reliability and stability of PV installations. As a result, effective energy storage solutions are indispensable for ensuring the continuous availability of solar power, especially during periods of low sunlight or high demand.

Supercapacitors, also known as electrochemical capacitors or ultracapacitors, have emerged as promising candidates for addressing the energy storage requirements of PV systems. Unlike conventional batteries, which store energy through chemical reactions, supercapacitors store electrical energy through the physical separation of

charges at the interface between electrodes and electrolytes. This mechanism allows supercapacitors to deliver rapid charge and discharge cycles, high power density, and a long cycle life, making them well-suited for applications requiring frequent and rapid energy exchanges.

The main contributions of this study are:

1) The article consolidates existing knowledge on the integration of supercapacitors in photovoltaic (PV) systems, providing readers with a comprehensive overview of the topic. By synthesizing information from a variety of sources, the article serves as a valuable resource for researchers, engineers, policymakers, and other stakeholders interested in sustainable energy solutions.
2) The article identifies and discusses the advantages and challenges associated with integrating supercapacitors in PV systems. By highlighting the benefits of this approach, such as improved energy management, reliability, and efficiency, as well as addressing potential obstacles such as cost and energy density limitations, the article provides readers with a balanced understanding of the topic.
3) The article explores recent advancements in supercapacitor technology and presents case studies of integrated PV and supercapacitor systems. By showcasing real-world examples and highlighting innovative solutions, the article offers insights into the practical implementation and performance of integrated systems across different applications and scales.
4) The article identifies future research directions and opportunities for further innovation in the fields of integrated PV and supercapacitor systems. By discussing emerging technologies, research priorities, and areas for collaboration, the article guides readers towards promising avenues for advancing the state-of-the-art and driving the adoption of sustainable energy solutions.
5) The article informs decision-making and policy development by providing evidence-based insights into the potential benefits and challenges of integrating supercapacitors in PV systems. Policymakers and industry stakeholders can use this information to formulate strategies, allocate resources, and support initiatives aimed at promoting the adoption of renewable energy technologies and enhancing energy sustainability.

In this context, the reminder of this paper is as follows: in the first section, the importance of the supercapacitors is highlighted, and the main contributions of the study are expressed. In the second section, information is given about the working principle and types of supercapacitors. Then, the integration of supercapacitors into PV energy systems is examined, and various studies on the subject are presented. Then, the advantages and challenges of the supercapacitors are investigated. After that, recent developments and key studies about the usage of supercapacitors in PV energy systems are presented. Then, it is attempted to shed light on the future direction of studies on supercapacitors. In the conclusion section, the studies carried out over the years are given, and the subject is summarized. The overview of the study is given in **Figure 1**.

Figure 1. The overview of the study.

By harnessing the complementary strengths of supercapacitors and photovoltaics, it is aimed to pave the way towards more resilient, efficient, and environmentally sustainable solar energy systems. Through this exploration, a future is envisioned where renewable energy sources like solar power, supported by advanced energy storage technologies such as supercapacitors, are seen to play a central role in the global transition towards a cleaner and more sustainable energy landscape.

2. Fundamentals of supercapacitors

Supercapacitors, also known as ultracapacitors or electrochemical capacitors, represent a class of energy storage devices that bridge the gap between traditional capacitors and batteries. Unlike batteries, which store energy through chemical reactions, supercapacitors store electrical energy through the physical separation of charges at the interface between electrodes and an electrolyte. This mechanism allows supercapacitors to achieve exceptionally high power density and rapid charge/discharge capabilities, making them ideal for applications requiring quick bursts of energy.

At the heart of a supercapacitor lies its unique electrode structure, typically composed of porous materials with a high surface area. Common electrode materials include activated carbon, carbon nanotubes, and graphene, which provide ample surface area for charge accumulation and facilitate efficient charge transfer. The electrolyte, often an aqueous or organic solution containing ions, serves as the medium for ion transport between the electrodes, enabling the storage and release of electrical energy. Özada et al. [1] defined the working principles and characteristics of supercapacitors in energy storage systems.

Supercapacitors can be broadly classified into two main types based on their electrode materials and electrolyte composition: electrochemical double-layer capacitors (EDLCs) and pseudocapacitors. EDLCs store energy primarily through the physical adsorption of ions at the electrode/electrolyte interface, relying on the formation of an electric double layer. Pseudocapacitors, on the other hand, exhibit additional electrochemical redox reactions at the electrode surface, leading to enhanced energy storage capacities compared to EDLCs.

An EDLC has two non-reactive porous electrodes immersed in an electrolyte, with a separator between the electrodes that permits the movement of the ions through it. The energy is stored by charge separation in an electrochemical double layer, formed at the electrode/electrolyte interface [2]. The internal structure of an EDLC is given in **Figure 2**. Energy storage occurs through the process of charge separation within an electrochemical double layer, which materializes at the interface between

the electrode and the electrolyte. The thickness of this double layer is intricately influenced by factors such as the electrolyte concentration and the dimensions of the ions involved, typically ranging between 0.5 and 1 nanometer in the case of concentrated electrolytes. The ions necessary for charging the electrochemical double-layer capacitor are transported between the porous electrodes via diffusion through the electrolyte.

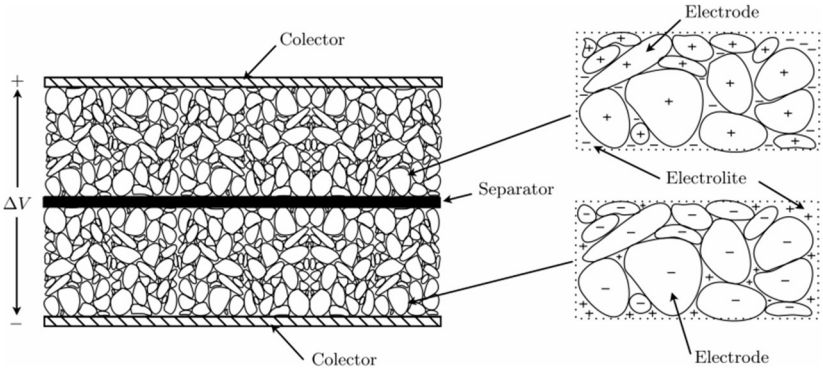

Figure 2. Internal structure of EDLC [2].

The use of activated carbon electrodes and the limitations on voltage and accessible surface area are discussed in another study [3]. **Figure 3** represents the schematic of an activated carbon-based EDLC and the electron micrograph of an activated carbon electrode. The combination of a minute charge separation within the double layer and the extensive surface area of the electrode leads to a specific capacitance typically ranging from 40 to 60 farads per cubic centimeter (F/cm^3). Moreover, the breakdown field strength of the EDLC, expressed in volts per centimeter (V/cm), is notably elevated compared to conventional capacitors. These three factors—namely, the large surface area, minimal charge separation, and heightened field strength—contribute to the remarkable energy density achievable with the EDLC.

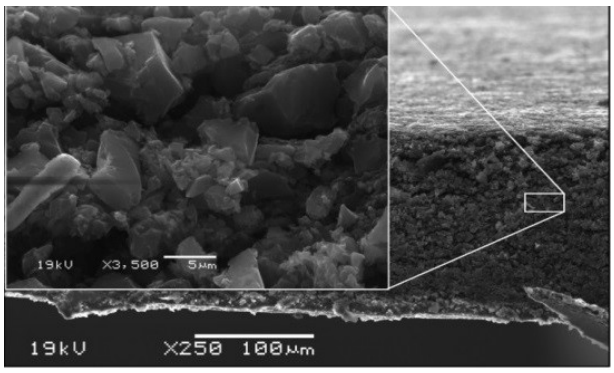

Figure 3. Electron micrograph view of activated carbon electrode [3].

One of the defining characteristics of supercapacitors is their remarkable cycle life, which far exceeds that of conventional batteries. Unlike batteries, which degrade over time due to chemical reactions and electrode wear, supercapacitors undergo minimal degradation even after hundreds of thousands or millions of charge/discharge cycles. This longevity, combined with their rapid response times and high efficiency,

makes supercapacitors well-suited for applications requiring frequent and prolonged operation, such as renewable energy systems and electric vehicles.

Kamali et al. [4] evaluated the environmental impact of two supercapacitor designs in a prospective life cycle assessment conducted at a later stage. Jiang et al. [5] utilized a life cycle assessment method to examine the environmental performance of a nitrogen-doped biochar aerogel-based electrode (BA-electrode) derived from Entermorpha prolifera. Torregrossa and Paolone [6] introduced a novel experimental approach to investigate the aging mechanisms affecting supercapacitors. Their study outlines a carefully designed procedure aimed at assessing the aging process through combined life endurance and power cycling tests. Specifically, their study evaluates the impact of temperature (referred to as life endurance) on supercapacitors subjected to a predetermined power cycle. Additionally, their investigation delves into the effects of temperature during the recovery phase. Cossutta et al. [7] conducted a comprehensive assessment, covering the entire lifecycle of graphene applications. Specifically, it focuses on a case study involving the manufacturing of supercapacitors utilizing graphene and activated carbon as active materials. Tankari et al. [8] used the Rainflow Cycles Counting Method to estimate the supercapacitors lifetime.

Li et al. [9] prepared a redox-active organic molecular electrode for supercapacitors. In their study, the researchers investigated the adsorption of Benzo[1,2-b:4,5-b'] dithiophene-4,8-dione (BDTD), a planar molecule with a fused heteroaromatic structure, onto conductive reduced graphene oxide (rGO) through pi-pi interactions. This process resulted in the formation of a three-dimensional interconnected and functionalized xerogel, referred to as BDTD-rGO. Consequently, the optimized BDTD-rGO electrodes demonstrated a specific capacitance of 360 Fg^{-1} at 1 Ag^{-1}, coupled with an exceptionally long cycle life, retaining 96.4% of their capacitance after 10,000 cycles and still maintaining 80% after 50,000 cycles at 5 Ag^{-1} in 1 M H_2SO_4.

Glogic et al. [10] used coconut shells to produce high-performance activated carbon electrodes for energy storage supercapacitors. Their analysis was carried out using the life cycle assessment approach to investigate the production of activated carbon material and resulting electrodes for a broad range of environmental impact categories and energy use.

Murray and Hayes [11] presented the results of a study on supercapacitor lifetime. Cycle testing was carried out on individual supercapacitors at room temperature and at rated temperature, utilizing a thermal chamber and equipment programmed through GPIB and MATLAB. The results of their study demonstrate cycle lifetimes significantly in excess of manufacturer specifications and potential for deployment in robust long-life applications. **Figure 4** represents the capacitance versus cycle number of a supercapacitor during application testing at 25 ℃. The application study anticipates approximately one million cycles for a full-scale energy storage system comprising supercapacitor modules. Assuming the same cycle lifetime degradation observed in the tested single supercapacitor (excluding other aging factors), it is projected that the system could operate at sea for an estimated duration of 34 years.

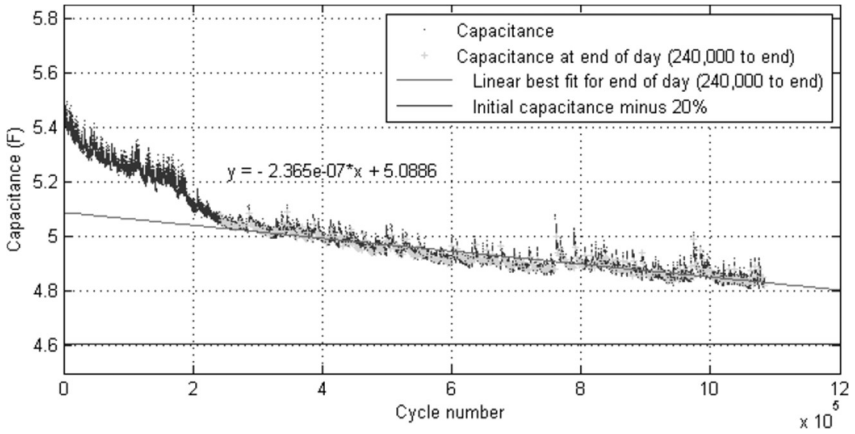

Figure 4. Capacitance versus cycle number of a supercapacitor during application testing at 25 ℃ [11].

In summary, supercapacitors offer a unique set of advantages, including high power density, rapid charge/discharge capabilities, long cycle life, and robust performance under diverse operating conditions. Understanding the fundamental principles underlying supercapacitor operation is essential for harnessing their full potential in various energy storage applications, including their integration into photovoltaic systems for enhanced performance and reliability.

3. Integration of supercapacitors in PV systems

The integration of supercapacitors with photovoltaic (PV) systems offers a promising avenue for overcoming the intermittent nature of solar energy and improving overall system performance. By storing excess energy generated during periods of high sunlight and delivering it during periods of low irradiance or high demand, supercapacitors enable PV systems to achieve greater energy autonomy and reliability. The integration of supercapacitors can be realized through various configurations, including parallel or series connections with PV modules, as well as system-level integration with power electronics and control systems.

In a parallel configuration, supercapacitors are connected in parallel with PV modules, allowing them to capture surplus energy generated by the solar panels and store it for later use. This approach enhances the overall energy management of the system, reducing dependence on the grid and maximizing self-consumption of solar energy. Additionally, supercapacitors can serve as buffer devices to smooth out fluctuations in PV output caused by factors such as shading, clouds, or variations in solar irradiance, thereby improving system stability and efficiency.

Zhang et al. [12] connected an appropriate supercapacitor in parallel with the PV system in order to further mitigate the fluctuations in the PV system. The simulation results demonstrated that the designed supercapacitor structure has better performance than conventional structures.

Keshavarzi and Ali [13] introduced an integrated and cost-effective photovoltaic-supercapacitor (PVSC) system, merging the energy storage capability of the supercapacitor (SC) directly into the PV array. This integration facilitates bidirectional power flow, ensuring system stability during grid disturbances occurring throughout the day, night, and under cloudy conditions. The efficacy of this system was assessed

through simulation analysis and compared against that of a basic PV system and a conventional SC system, where the full energy storage is parallel-connected with the PV. The results indicate that the proposed PVSC system enhances the dynamic performance of the grid system it is connected to. **Figure 5** shows a parallel supercapacitor structure.

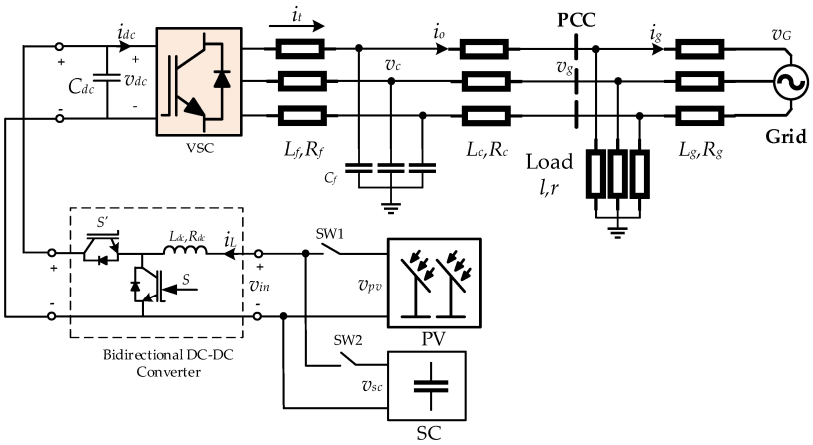

Figure 5. Power stage of a PV-supercapacitor energy storage system [13].

In a series configuration, supercapacitors are connected in series with the PV modules, typically through a DC-DC converter or charge controller. This setup enables the supercapacitors to store energy at a higher voltage level, enhancing their energy storage capacity and efficiency. By storing energy at a higher voltage, supercapacitors can minimize energy losses during charging and discharging cycles, leading to improved overall system performance and energy yield. Series-connected supercapacitors can also provide voltage support and regulation, ensuring optimal operation of the PV system under varying load conditions.

System-level integration of supercapacitors with PV systems involves the incorporation of advanced power electronics and control algorithms to optimize energy management and performance. This may include the use of maximum power point tracking (MPPT) algorithms to maximize energy harvest from the PV array, as well as intelligent energy management systems to dynamically allocate energy between the PV modules and supercapacitors based on real-time demand and operating conditions. Such integration schemes enable PV systems to operate more efficiently and autonomously, reducing reliance on external energy sources and enhancing overall system resilience.

Han et al. [14] conducted research on a sizeable dispatchable grid-connected photovoltaic (PV) system designed to feed power directly into the grid for centralized dispatch rather than supplying electricity solely to a local load. To optimize the utilization of solar energy, the system incorporates a hybrid electricity storage solution comprising both batteries and supercapacitors alongside the PV array.

Sahin and Blaabjerg [15] investigated and analyzed the advantages of incorporating supercapacitors in a hybrid energy storage system. Their study proposes a hybrid system that harnesses photovoltaic energy and stores it using both batteries and supercapacitors, aiming to address key challenges on both fronts. Using MATLAB/Simulink, they designed models for the supercapacitor, photovoltaic

system, and the proposed hybrid setup rated at 6 kW. **Figure 6** illustrates a MATLAB/Simulink model of a supercapacitor. Additionally, they introduced a novel topology aimed at enhancing energy storage capacity with supercapacitors in a passive storage setup. This topology focuses on temporarily storing instantaneous peak currents in supercapacitors, leading to voltage stabilization on both ends and reducing the load on batteries. Consequently, this approach extends battery lifespan and reduces overall system costs.

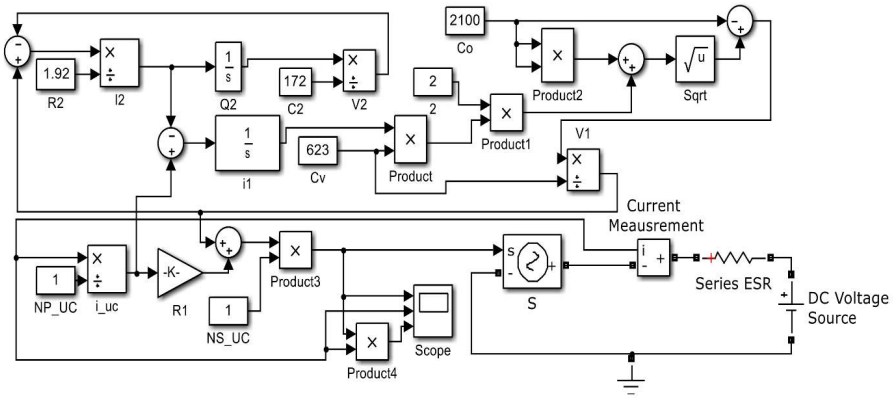

Figure 6. MATLAB/Simulink model of a supercapacitor [15].

Yang and Hu [16] introduced an innovative dynamic inertia control strategy for supercapacitors in multi-area autonomous microgrid (MG) clusters, utilizing a fuzzy-based approach. Javadpoor and Nazarpour [17] explored a hybrid photovoltaic (PV)-hydrogen/fuel cell (FC) system comprising fundamental components such as a PV array, a fuel cell, alkaline water electrolysis, and a hydrogen storage tank. Zhao et al. [18] introduced a multiobjective optimization approach for electric vehicle-supercapacitor hybrid energy storage systems aimed at aligning with the output of photovoltaic projects. Sabhahit et al. [19] outline control strategies tailored for a hybrid power system integrating photovoltaics, fuel cells, and a supercapacitor bank, designed for use in isolated load scenarios. Tummuru et al. [20] have introduced rapid-response DC-link voltage-dependent energy management strategies designed for a hybrid energy storage system powered by solar photovoltaic (PV) energy.

Hossain et al. [21] outlined a comprehensive approach involving the design and execution of a universal ramp-rate-based compensation technique. This strategy is aimed at stabilizing solar power output and swiftly meeting sudden load demands within grid-connected microgrids. It leverages a hybrid multilevel storage system incorporated into the DC link of the power converter. This system includes high-capacity buffer storage like battery systems and hydrogen storage, comprising a proton exchange membrane electrolyzer and a fuel cell. Additionally, short-term cache storage, such as supercapacitors, is employed to enhance system efficiency.

Xiong and Nour [22] acknowledged the importance of energy storage by conducting simulations of a comprehensive PV-battery-supercapacitor model using MATLAB/Simulink. This simulation aimed to generate a flat load profile, enhancing predictability from a network management perspective. Regowski et al. [23] provided findings from measurements and parameter comparisons of an energy storage system comprising supercapacitor batteries and a conventional lead-acid solution. This system

was specifically tailored for use in photovoltaic micro-installations. Given the lack of dependable and cost-effective PV module characterization systems, the development and analysis of a smart, digital, and portable test setup is of considerable importance. Pal et al. [24] have addressed this need by devising and evaluating such a model in their study. In their setup, supercapacitors serve as the load for the photovoltaic module being tested.

Abbassi et al. [25] have introduced a novel approach for optimally determining the size of a hybrid energy storage system (HESS) using a statistical method. This method is designed to leverage the capacity distribution of a hybrid supercapacitor-battery system within an autonomous photovoltaic (PV)/wind power generation setup.

Palla and Kumar [26] introduced an algorithm designed to coordinate the control of photovoltaic systems and ultracapacitor-based energy storage systems. Their proposed system is shown in **Figure 7**. The aim is to mitigate the impacts of abrupt variations in solar irradiance and address low-voltage occurrences at the point of common coupling. Furthermore, their study presents an enhanced multi-mode operational scheme for controlling ultracapacitor-based energy storage systems. This scheme accounts for various constraints associated with both charging and discharging modes.

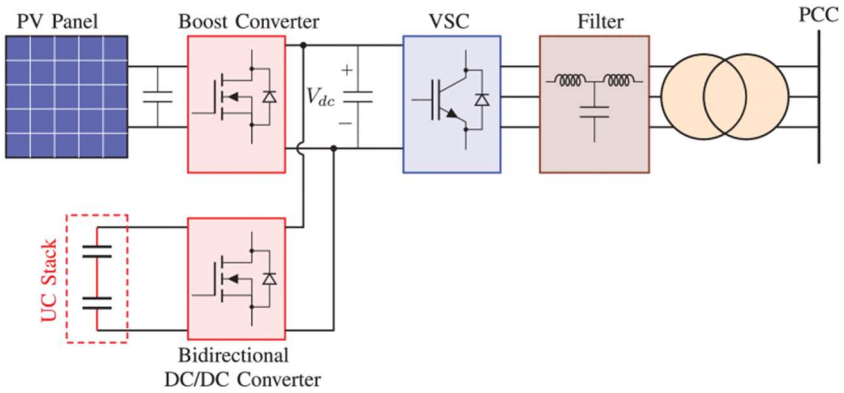

Figure 7. Configuration of a typical PV-Ultracapacitor system.

Benavides et al. [27] have introduced a power smoothing technique employing supercapacitors within a grid-connected photovoltaic system. This method operates through two distinct stages: prediction and correction, aimed at enhancing power stability.

Roy et al. [28] investigated a HESS integrating both a battery and a supercapacitor for managing solar power dispatch in hourly increments over a full day for 1 MW grid-connected PV arrays. The HESS operates autonomously, utilizing the PV array for charging rather than relying on grid power, ensuring immunity to fluctuations in electricity prices. While the battery and supercapacitor are designed to deliver consistent, predetermined power levels, their primary function does not include providing ancillary services for grid operation.

In summary, the integration of supercapacitors in PV systems offers significant benefits in terms of energy storage, management, and system performance. Whether deployed in parallel or series configurations or integrated at the system level with advanced control strategies, supercapacitors enhance the reliability, efficiency, and

sustainability of photovoltaic installations, contributing to the broader transition towards a clean and renewable energy future.

4. Advantages and challenges

The integration of supercapacitors in photovoltaic systems offers a range of advantages that contribute to improved system performance, reliability, and efficiency. One of the key advantages is the rapid charge and discharge capabilities of supercapacitors, which enable them to respond quickly to fluctuations in solar irradiance and load demand. This ability to store and release energy rapidly makes supercapacitors well-suited for applications requiring high-power bursts, such as grid stabilization, frequency regulation, and peak shaving.

Another advantage of supercapacitors is their long cycle life and robust performance under diverse operating conditions. Unlike conventional batteries, which degrade over time due to chemical reactions and electrode wear, supercapacitors undergo minimal degradation even after thousands or millions of charge and discharge cycles. This longevity ensures the reliability and durability of the energy storage system, reducing maintenance requirements and overall lifecycle costs.

Supercapacitors also offer high efficiency and energy density compared to other energy storage technologies, such as batteries. Their high charge/discharge efficiency and low internal resistance result in minimal energy losses during energy conversion processes, maximizing overall system efficiency. Additionally, supercapacitors can achieve high energy densities when combined with advanced electrode materials and electrolytes, further enhancing their energy storage capacity and performance.

Despite these advantages, the integration of supercapacitors in PV systems presents certain challenges and limitations that must be addressed. One of the primary challenges is the relatively low energy density of supercapacitors compared to batteries, which limits their ability to store large amounts of energy over extended periods. This constraint may necessitate the use of hybrid energy storage systems combining supercapacitors with batteries or other storage technologies to achieve the desired energy storage capacity while maintaining high power density and efficiency.

Cost is another factor to consider when integrating supercapacitors into PV systems. While supercapacitors offer long-term cost savings due to their extended lifecycle and minimal maintenance requirements, their initial capital costs can be higher than those of traditional battery systems. However, ongoing advancements in supercapacitor technology, along with economies of scale in manufacturing, are expected to drive down costs and improve cost-effectiveness over time.

Temperature sensitivity is another challenge associated with supercapacitors, as their performance and lifespan can be affected by temperature variations. Extreme temperatures can degrade electrode materials, reduce electrolyte conductivity, and compromise overall system efficiency and reliability. Therefore, proper thermal management strategies must be implemented to mitigate temperature-related effects and ensure optimal performance of the integrated PV and supercapacitor systems.

In summary, while the integration of supercapacitors in PV systems offers numerous advantages in terms of performance, reliability, and efficiency, it also presents certain challenges and considerations that must be addressed. By overcoming

these challenges through ongoing research, innovation, and technological advancements, supercapacitors have the potential to play a significant role in enhancing the sustainability and viability of solar energy systems.

5. Recent developments and case studies

In recent years, there have been significant advancements in the development and integration of supercapacitors in photovoltaic systems, driven by a growing demand for reliable and efficient renewable energy solutions. These advancements encompass a wide range of areas, including materials science, device engineering, system design, and control algorithms, aimed at improving the performance, durability, and cost-effectiveness of integrated PV and supercapacitor systems.

One area of innovation in supercapacitor technology is the development of advanced electrode materials with enhanced energy storage capacities and improved electrochemical properties. Researchers have explored novel carbon-based materials, such as carbon nanotubes, graphene, and activated carbon composites, as well as transition metal oxides and conducting polymers, to increase the energy density and power density of supercapacitors. These materials offer higher specific surface areas, greater charge storage capacities, and faster charge/discharge rates, enabling the development of supercapacitors with superior performance characteristics for PV energy storage applications.

Zhang et al. [29] primarily discuss recent progress and obstacles in flexible supercapacitors, with a focus on the synthesis and performance of flexible substrates. Ji et al. [30] emphasized the principle of designing electrode materials, which involves comprehending the connections between the structural design, properties, and components of electrode materials and how these factors influence their electrochemical performance. Jiang et al. [31] have provided a recent review of carbon-based nanostructured electrode materials, encompassing structures ranging from zero-dimensional to three-dimensional. Their analysis delves into the impact of nanostructuring on supercapacitor properties, such as specific capacitance, rate capability, and cycle stability. The insights gained from this exploration may serve as valuable guidance for the design of electrodes in the development of the next generation of EDLCs. Grace and Ramachandran [32] discussed advancements in the development of nanostructured materials for supercapacitor electrodes. Baig et al. [33] outlined the operational principles and obstacles associated with various advanced materials utilized in supercapacitor electrodes, along with proposed strategies for addressing these challenges.

In addition to material advancements, there have been notable developments in the design and fabrication of supercapacitor devices tailored for integration with PV systems. These include the development of flexible and lightweight supercapacitors compatible with flexible PV modules and building-integrated photovoltaics (BIPV) applications. Such devices offer enhanced mechanical flexibility, conformability, and durability, enabling seamless integration into various architectural and structural elements while maintaining high energy storage performance.

Maddala et al. [34] showcased the remarkable photovoltaic power conversion efficiency (PCE) of 11.12% achieved through single-wall carbon nanohorn-assisted

carbon counter electrodes in dye-sensitized solar cells (DSSCs). This efficiency surpassed that of platinum (9.41%), motivating the fabrication of a dye-sensitized solar module (DSSM) comprising six series-connected DSSCs arranged in a bifacial configuration for building-integrated photovoltaic applications. The DSSM achieved an impressive champion PCE of 19.71%. To further enhance this efficiency, an integrated device, termed a photocapacitor, was developed, combining the DSSM with a supercapacitor.

Several case studies and real-world implementations highlight the effectiveness and benefits of integrating supercapacitors into PV systems across different scales and applications. For example, in off-grid and remote areas where access to reliable electricity is limited, standalone PV systems with integrated supercapacitors provide a cost-effective and sustainable energy solution. These systems can store excess solar energy during the day and deliver it during periods of high demand or low sunlight, ensuring continuous power supply for lighting, communication, and other essential services. In grid-connected PV installations, supercapacitors serve as valuable assets for enhancing grid stability, power quality, and energy management. By providing fast response times and high-power support, supercapacitors can mitigate voltage fluctuations, frequency variations, and transient disturbances caused by intermittent renewable energy sources such as solar power. Furthermore, supercapacitors enable grid operators to implement demand response strategies, peak shaving, and energy arbitrage schemes, optimizing the use of renewable energy resources and reducing reliance on fossil fuels.

Hamdan et al. [35] discussed methods to enhance the stability of grid-connected photovoltaic systems by incorporating supercapacitors. **Figure 8** shows their supercapacitor model. Their approach focuses on applying this technique to photovoltaic systems, utilizing the perturbation and observation (P&O) algorithm for maximum power point tracking. The P&O algorithm serves to optimize power extraction from the photovoltaic system under study.

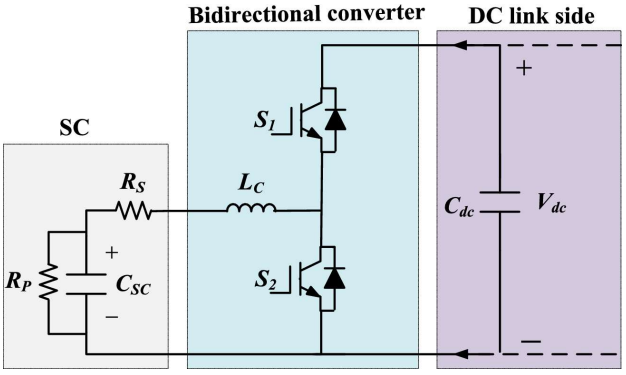

Figure 8. Schematic diagram of the SC model [35].

Vargas et al. [36] introduced a model designed for harmonic transient simulation of a standalone photovoltaic system, incorporating a hybrid energy storage system comprised of batteries and supercapacitors. This model utilizes a newly introduced technique for harmonic domain modeling.

Ramineni et al. [37] have devised and applied an energy management (EM) model to a foundational electric vehicle (EV) model powered by solar energy.

Predicting the driver cycle of the EV poses a significant challenge in any EM model. The core structure incorporates solar panels, supercapacitors, batteries, DC-DC converters, and appropriate control models.

Alam et al. [38] introduced a control strategy for supercapacitors within a microgrid composed of multiple clusters integrating various renewable energy sources and generators, including wind power, solar photovoltaics, solar thermal power (STP), fuel cells, aqua electrolyzers, and diesel generators. Initially, they developed a small-signal model to aid in control design. This model was then combined with a fractional-order supercapacitor controller to stabilize the microgrid frequency. Additionally, optimization of controller parameters was conducted to ensure robust performance.

Arkhangelski et al. [39] investigated a Hybrid Renewable Energy System (HRES) as a dependable power supply source when connected to the grid. Grid connection imposes limitations on the power output and harmonic content of the HRES, necessitating the use of multiple control systems and subsystems such as measurement normalization, current control, active harmonic compensation, and synchronization, as detailed in their study. Special emphasis was placed on interactions within the storage system of the HRES. Combining supercapacitors and batteries was identified as a method to enhance the durability of the HRES.

Díaz-González et al. [40], the authors introduced a two-level controller designed to oversee a hybrid energy storage solution for integrating photovoltaic plants into distribution grids. This HESS involves linking a lead-acid battery pack with a supercapacitor pack via a modular power electronics cabinet. **Figure 9** shows the active power results of their study. As depicted, the peak power exchanged with the grid is significantly diminished, ensuring that maximum values remain below 6 kW. Additionally, concerning apparent power, the values remain below the maximum threshold set by grid ratings. This power limitation is achieved through the coordinated operation of both the battery and supercapacitor packs.

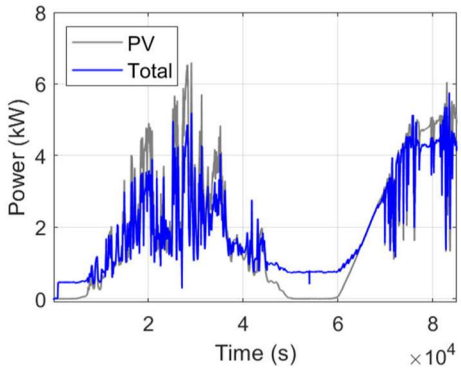

Figure 9. The total active power output of the PV plant with and without the contribution of the hybrid energy storage solution [40].

Mbouteu Megaptche et al. [41], the authors discussed the utilization of a Demand Response-Fuzzy Inference System Controller (DR-FIS) to regulate the operation of loads. This controller was employed for the sizing optimization of systems comprising photovoltaic/wind turbine/battery/supercapacitor and photovoltaic/wind turbine/battery/diesel generator setups, operating autonomously in a health center located in northern Cameroon. The optimization process utilized multi-objective

particle swarm optimization (MOPSO) and multi-objective genetic algorithm (MOGA) methods.

Overall, recent developments in supercapacitor technology and case studies of integrated PV and supercapacitor systems demonstrate the potential for these solutions to drive the transition towards a more sustainable and resilient energy future. By leveraging advancements in materials science, device engineering, and system integration, integrated PV and supercapacitor systems offer scalable, reliable, and cost-effective solutions for meeting the growing demand for clean energy worldwide.

6. Future directions and opportunities

As the demand for renewable energy continues to rise and the need for sustainable energy solutions becomes increasingly urgent, the integration of supercapacitors in photovoltaic systems presents exciting opportunities for further innovation and advancement. Looking ahead, several key areas emerge as focal points for future research, development, and implementation of integrated PV and supercapacitor systems.

One area of focus is the continued advancement of supercapacitor technology to improve energy density, power density, and efficiency. Ongoing research efforts aim to develop new electrode materials, electrolytes, and device architectures capable of enhancing the energy storage capacity and performance of supercapacitors while maintaining their fast charge/discharge capabilities and long cycle life. Advances in nanomaterials, hybrid energy storage systems, and manufacturing processes hold promise for achieving breakthroughs in supercapacitor performance and cost-effectiveness.

Another area of interest is the integration of supercapacitors with emerging PV technologies, such as perovskite solar cells, tandem solar cells, and organic photovoltaics. These next-generation PV technologies offer higher efficiency, lower manufacturing costs, and greater flexibility compared to traditional silicon-based solar cells, opening up new opportunities for integrated PV and supercapacitor systems in a variety of applications. By combining the advantages of advanced PV technologies with the energy storage capabilities of supercapacitors, researchers aim to develop highly efficient, lightweight, and cost-effective solutions for distributed energy generation, grid integration, and electrification initiatives.

In addition to technological advancements, future research efforts will focus on addressing key challenges and barriers to the widespread adoption of integrated PV and supercapacitor systems. These challenges include cost competitiveness, system scalability, standardization, and regulatory frameworks. Collaborative research initiatives involving academia, industry, and government agencies are needed to overcome these challenges and accelerate the deployment of integrated PV and supercapacitor systems on a global scale.

Furthermore, the development of advanced control algorithms and energy management strategies will play a crucial role in optimizing the operation and performance of integrated PV and supercapacitor systems. By leveraging real-time data, predictive analytics, and machine learning techniques, researchers can develop intelligent control systems capable of maximizing energy harvest, optimizing energy

storage, and minimizing grid impact. These advanced control strategies will enable integrated PV and supercapacitor systems to operate autonomously, adaptively, and efficiently under diverse operating conditions and grid environments.

In summary, the integration of supercapacitors in PV systems holds tremendous potential for shaping the future of renewable energy and accelerating the transition towards a sustainable energy landscape. By focusing on technological innovation, research collaboration, and policy support, stakeholders can unlock new opportunities and overcome barriers to the widespread adoption of integrated PV and supercapacitor systems, paving the way for a cleaner, greener, and more resilient energy future.

7. Conclusions

The integration of supercapacitors in photovoltaic (PV) systems represents a promising approach for addressing the energy storage challenges associated with solar energy and advancing the transition towards a sustainable energy future. Through this exploration, it is evident that supercapacitors offer unique advantages such as high power density, rapid charge/discharge capabilities, and long cycle life, making them well-suited for applications requiring efficient and reliable energy storage. The number of academic publications regarding the use of supercapacitors in PV energy systems has increased over the years. **Figure 10** shows the number of academic publications involving the use of supercapacitors in photovoltaic energy systems in the last fifteen years [42]. Studies on the subject have doubled in the last five years.

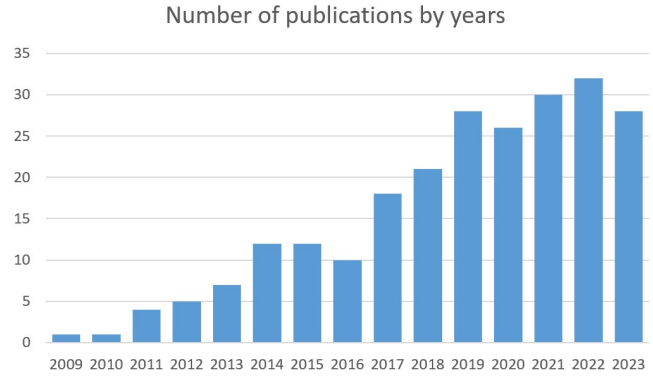

Figure 10. Number of publications by years [42].

By harnessing the complementary strengths of supercapacitors and PV technology, integrated systems can achieve greater energy autonomy, reliability, and efficiency. Supercapacitors enable PV systems to capture surplus energy during periods of high sunlight and deliver it during periods of low irradiance or high demand, thereby enhancing overall system performance and stability. The integration of supercapacitors also facilitates grid integration, demand response, and energy management strategies, enabling PV systems to contribute to grid stability and resilience.

Furthermore, recent developments in supercapacitor technology and case studies of integrated PV and supercapacitor systems demonstrate the feasibility and effectiveness of this approach across a wide range of applications and scales. From off-grid installations in remote areas to grid-connected systems in urban environments,

integrated PV and supercapacitor systems offer scalable, reliable, and cost-effective solutions for meeting the growing demand for clean energy worldwide.

Looking ahead, there are exciting opportunities for further innovation and advancement in the field of integrated PV and supercapacitor systems. Future research efforts will focus on enhancing the energy density, efficiency, and cost-effectiveness of supercapacitors, as well as exploring new materials, device architectures, and system integration strategies. Collaborative research initiatives involving academia, industry, and government agencies will be essential for overcoming key challenges and accelerating the adoption of integrated PV and supercapacitor systems on a global scale.

In conclusion, the integration of supercapacitors in PV systems holds tremendous potential for driving the transition towards a more sustainable, resilient, and efficient energy landscape. By leveraging advancements in technology, research collaboration, and policy support, stakeholders can unlock new opportunities and overcome barriers to the widespread adoption of integrated PV and supercapacitor systems, ultimately contributing to a cleaner, greener, and more sustainable future for generations to come.

Conflict of interest: The author declares no conflict of interest.

References

1. Özada Ç, Ünal M, Yazici M. Supercapacitor: Fundamentals and materials (Turkish). Gazi Üniversitesi Mühendislik Mimarlık Fakültesi Dergisi. 2023; 39(2): 1315-1332. doi: 10.17341/gazimmfd.1141220
2. Martin R, Quintana JJ, Ramos A, et al. Modeling electrochemical double layer capacitor, from classical to fractional impedance. In: Proceedings of the MELECON 2008 - The 14th IEEE Mediterranean Electrotechnical Conference; 5-7 May 2008; Ajaccio, France. pp. 12-16. doi: 10.1109/melcon.2008.4618411
3. Signorelli R, Ku DC, Kassakian JG, et al. Electrochemical Double-Layer Capacitors Using Carbon Nanotube Electrode Structures. Proceedings of the IEEE. 2009; 97(11): 1837-1847. doi: 10.1109/jproc.2009.2030240
4. Kamali AK, Glogic E, Keppetipola NM, et al. Prospective Life Cycle Assessment of Two Supercapacitor Architectures. ACS Sustainable Chemistry & Engineering. 2023; 11(44): 15898-15909. doi: 10.1021/acssuschemeng.3c04007
5. Jiang Z, Zou Y, Li Y, et al. Environmental life cycle assessment of supercapacitor electrode production using algae derived biochar aerogel. Biochar. 2021; 3(4): 701-714. doi: 10.1007/s42773-021-00122-1
6. Torregrossa D, Paolone M. Novel experimental investigation of supercapacitor ageing during combined life-endurance and power-cycling tests. In: Proceedings of the IECON 2013 - 39th Annual Conference of the IEEE Industrial Electronics Society; 10-13 November 2013; Vienna, Austria. pp. 36-41. doi: 10.1109/iecon.2013.6699401
7. Cossutta M, Vretenar V, Centeno TA, et al. A comparative life cycle assessment of graphene and activated carbon in a supercapacitor application. Journal of Cleaner Production. 2020; 242: 118468. doi: 10.1016/j.jclepro.2019.118468
8. Tankari MA, Lefebvre G, Bellache K, et al. Supercapacitor Lifetime Estimation Based on Rainflow Cycle Counting Method. In: Proceedings of the 2015 IEEE Vehicle Power and Propulsion Conference (VPPC). 19-22 October 2015; Montreal, QC, Canada. doi: 10.1109/vppc.2015.7353028
9. Li S, Wang X, Hou L, et al. Graphene hydrogels functionalized non-covalently by fused heteroaromatic molecule for asymmetric supercapacitor with ultra-long cycle life. Electrochimica Acta. 2019; 317: 437-448. doi: 10.1016/j.electacta.2019.06.022
10. Glogic E, Kamali AK, Keppetipola NM, et al. Life Cycle Assessment of Supercapacitor Electrodes Based on Activated Carbon from Coconut Shells. ACS Sustainable Chemistry & Engineering. 2022; 10(46): 15025-15034. doi: 10.1021/acssuschemeng.2c03239
11. Murray DB, Hayes JG. Cycle Testing of Supercapacitors for Long-Life Robust Applications. IEEE Transactions on Power Electronics. 2015; 30(5): 2505-2516. doi: 10.1109/tpel.2014.2373368
12. Zhang L, Yu SS, Herbert HCI, et al. An advanced maximum power point capturing technique with supercapacitor for PV

system. In: Proceedings of the 2018 IEEE Power & Energy Society General Meeting (PESGM); 5-10 August 2018; Portland, OR, USA. pp. 1-5. doi: 10.1109/pesgm.2018.8586640
13. Keshavarzi MD, Ali MH. Dynamic Performance Enhancement of Power Grids by Operating Solar Photovoltaic (PV) System as Supercapacitor Energy Storage. Energies. 2021; 14(14): 4277. doi: 10.3390/en14144277
14. Han X, Ai X, Sun Y. Research on large-scale dispatchable grid-connected PV systems. Journal of Modern Power Systems and Clean Energy. 2014; 2(1): 69-76.
15. Sahin ME, Blaabjerg F. A Hybrid PV-Battery/Supercapacitor System and a Basic Active Power Control Proposal in MATLAB/Simulink. Electronics. 2020; 9(1): 129. doi: 10.3390/electronics9010129
16. Yang L, Hu Z. Implementation of Dynamic Virtual Inertia Control of Supercapacitors for Multi-Area PV-Based Microgrid Clusters. Sustainability. 2020; 12(8): 3299. doi: 10.3390/su12083299
17. Javadpoor S, Nazarpour D. Modeling a PV-FC-Hydrogen Hybrid Power Generation System. Engineering, Technology & Applied Science Research. 2017; 7(2): 1455-1459. doi: 10.48084/etasr.760
18. Zhao S, Zhou L, Zhang Q, et al. Research on electric vehicle-supercapacitor hybrid system participates in the application of tracking PV project output. Energy Science & Engineering. 2021; 10(1): 120-131. doi: 10.1002/ese3.1013
19. Sabhahit JN, Gaonkar DN, Nempu PB. Integrated power flow and voltage regulation of stand-alone PV-fuel cell system with supercapacitors. International Journal of Power and Energy Systems. 2017; 37(1). doi: 10.2316/journal.203.2017.1.203-6251
20. Tummuru NR, Mishra MK, Srinivas S. Dynamic Energy Management of Hybrid Energy Storage System with High-Gain PV Converter. IEEE Transactions on Energy Conversion. 2015; 30(1): 150-160. doi: 10.1109/tec.2014.2357076
21. Hossain MdB, Islam MdR, Muttaqi KM, et al. A Compensation Strategy for Mitigating Intermittencies Within a PV Powered Microgrid Using a Hybrid Multilevel Energy Storage System. IEEE Transactions on Industry Applications. 2023; 59(4): 5074-5086. doi: 10.1109/tia.2023.3262771
22. Xiong L, Nour M. Techno-Economic Analysis of a Residential PV-Storage Model in a Distribution Network. Energies. 2019; 12(16): 3062. doi: 10.3390/en12163062
23. Rogowski S, Sibinski M, Garlikowski K. Applications of supercapacitor systems in photovoltaic installations. Przeglad Elektrotechniczny. 2021; 97(12): 173-178.
24. Pal SB, Das Bhattacharya K, Mukherjee D, et al. A simple and low cost measurement technology for solar PV modules. Sādhanā. 2020; 45(1). doi: 10.1007/s12046-020-01509-9
25. Abbassi A, Dami MA, Jemli M. A statistical approach for hybrid energy storage system sizing based on capacity distributions in an autonomous PV/Wind power generation system. Renewable Energy. 2017; 103: 81-93. doi: 10.1016/j.renene.2016.11.024
26. Palla N, Kumar VSS. Coordinated Control of PV-Ultracapacitor System for Enhanced Operation Under Variable Solar Irradiance and Short-Term Voltage Dips. IEEE Access. 2020; 8: 211809-211819. doi: 10.1109/access.2020.3040058
27. Benavides D, Arévalo P, Aguado JA, et al. Experimental validation of a novel power smoothing method for on-grid photovoltaic systems using supercapacitors. International Journal of Electrical Power & Energy Systems. 2023; 149: 109050. doi: 10.1016/j.ijepes.2023.109050
28. Roy PKS, Karayaka HB, Yan Y, et al. Investigations into best cost battery-supercapacitor hybrid energy storage system for a utility scale PV array. Journal of Energy Storage. 2019; 22: 50-59. doi: 10.1016/j.est.2018.12.024
29. Zhang Y, Mei H, Cao Y, et al. Recent advances and challenges of electrode materials for flexible supercapacitors. Coordination Chemistry Reviews. 2021; 438: 213910. doi: 10.1016/j.ccr.2021.213910
30. Ji C, Mi H, Yang S. Latest advances in supercapacitors: From new electrode materials to novel device designs. Chinese Science Bulletin. 2018; 64(1): 9-34. doi: 10.1360/n972018-00815
31. Jiang J, Zhang Y, Nie P, et al. Progress of Nanostructured Electrode Materials for Supercapacitors. Advanced Sustainable Systems. 2017; 2(1). doi: 10.1002/adsu.201700110
32. Grace AN, Ramachandran R. Advanced Materials for Supercapacitors. In: Kumar SA (editor). Eco-Friendly Nano-Hybrid Materials for Advanced Engineering Applications. Apple Academic Press; 2017. pp. 99-128. doi: 10.1201/9781315366531-6
33. Baig MM, Khan MA, Gul IH, et al. A Review of Advanced Electrode Materials for Supercapacitors: Challenges and Opportunities. Journal of Electronic Materials. 2023; 52(9): 5775-5794. doi: 10.1007/s11664-023-10532-5
34. Maddala G, Ambapuram M, Tankasala V, et al. Optimal Dye Sensitized Solar Cell and Photocapacitor Performance with Efficient Electrocatalytic SWCNH Assisted Carbon Electrode. ACS Applied Energy Materials. 2021; 4(10): 11225-11233. doi: 10.1021/acsaem.1c02087

35. Hamdan I, Maghraby A, Noureldeen O. Stability improvement and control of grid-connected photovoltaic system during faults using supercapacitor. SN Applied Sciences. 2019; 1(12). doi: 10.1007/s42452-019-1743-2
36. Vargas U, Lazaroiu GC, Tironi E, et al. Harmonic modeling and simulation of a stand-alone photovoltaic-battery-supercapacitor hybrid system. International Journal of Electrical Power & Energy Systems. 2019; 105: 70-78. doi: 10.1016/j.ijepes.2018.08.004
37. Ramineni P, Pandian A, Kumar MK, et al. Improved operation of Li-ion battery with supercapacitor realized to solar-electric vehicle. Energy Reports. 2022; 8: 256-264. doi: 10.1016/j.egyr.2022.10.191
38. Alam Md, Almehizia A, Al-Ismail F, et al. Frequency Stabilization of AC Microgrid Clusters: An Efficient Fractional Order Supercapacitor Controller Approach. Energies. 2022; 15(14): 5179. doi: 10.3390/en15145179
39. Arkhangelski J, Roncero-Sánchez P, Abdou-Tankari M, et al. Control and Restrictions of a Hybrid Renewable Energy System Connected to the Grid: A Battery and Supercapacitor Storage Case. Energies. 2019; 12(14): 2776. doi: 10.3390/en12142776
40. Díaz-González F, Chillón-Antón C, Llonch-Masachs M, et al. A hybrid energy storage solution based on supercapacitors and batteries for the grid integration of utility scale photovoltaic plants. Journal of Energy Storage. 2022; 51: 104446. doi: 10.1016/j.est.2022.104446
41. Mbouteu Megaptche CA, Moses Musau P, Virginie Tjahè A, et al. Demand response-fuzzy inference system controller in the multi-objective optimization design of a photovoltaic/wind turbine/battery/supercapacitor and diesel system: Case of healthcare facility. Energy Conversion and Management. 2023; 291: 117245. doi: 10.1016/j.enconman.2023.117245
42. Web of Science. Available online: https://www.webofscience.com/wos/woscc/summary/6a502159-c0f0-4ec7-b967-492789d7eb8f-ce15b443/date-ascending/1 (accessed on 23 February 2024).

Academic Publishing Pte. Ltd.

Add: 73 Upper Paya Lebar Road #07-02B-01 Centro Bianco Singapore 534818

Tel: +65 83184869

E-mail: editorial_office@acad-pub.com

Web: http://ojs.acad-pub.com/